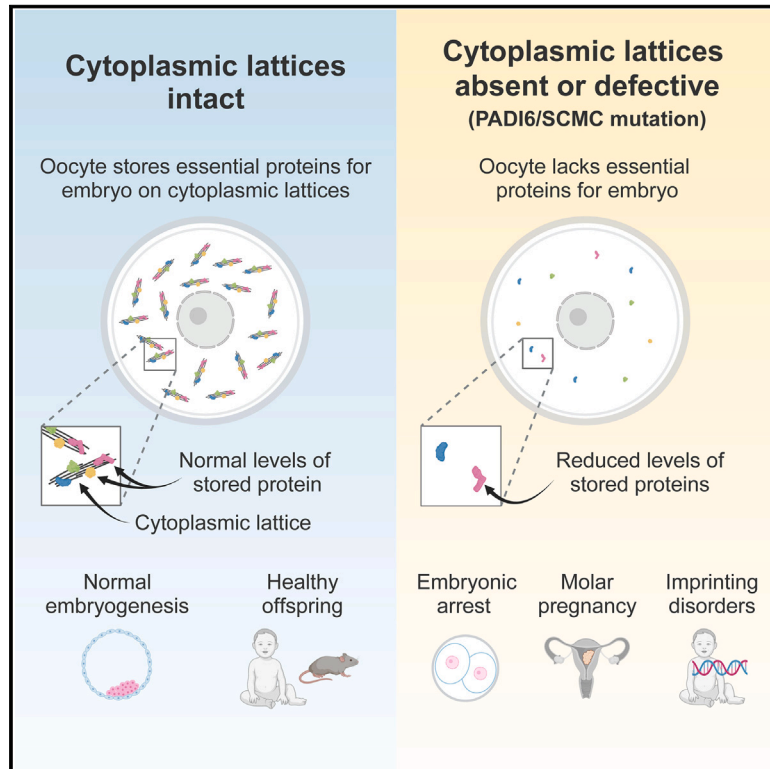# Mammalian oocytes store proteins for the early embryo on cytoplasmic lattices

Graphical abstract

Authors

Ida M.A. Jentoft, Felix J.B. Bäuerlein, Luisa M. Welp, ..., Henning Urlaub, Rubén Fernández-Busnadiego, Melina Schuh

Correspondence

melina.schuh@mpinat.mpg.de

In brief

Mammalian oocytes enrich proteins needed to sustain early embryonic development on cytoplasmic lattices. Loss of cytoplasmic lattices leads to reduced levels of maternally supplied proteins and embryogenesis failure.

Highlights

- Oocytes store essential proteins for early embryogenesis on cytoplasmic lattices

- Cytoplasmic lattices are composed of periodic filaments with high surface area

- Many stored proteins are required for epigenetic reprogramming of the embryo

- Study links infertility phenotypes in women with stored protein function

CellPress

Cell

Article

Mammalian oocytes store proteins for the early embryo on cytoplasmic lattices

Ida M.A. Jentoft,[1] Felix J.B. Bäuerlein,[2,3] Luisa M. Welp,[4,9] Benjamin H. Cooper,[5] Arsen Petrovic,[2,3] Chun So,[1] Sarah Mae Penir,[1] Antonio Z. Politi,[6] Yehor Horokhovskyi,[7] Iina Takala,[7] Heike Eckel,[8] Rüdiger Moltrecht,[8] Peter Lénárt,[6] Tommaso Cavazza,[1,12] Juliane Liepe,[7] Nils Brose,[3,5] Henning Urlaub,[3,4,9,10] Rubén Fernández-Busnadiego,[2,3,11] and Melina Schuh[1,3,13,*]

[1]Department of Meiosis, Max Planck Institute for Multidisciplinary Sciences, 37077 Göttingen, Germany
[2]Institute for Neuropathology, University Medical Center Göttingen, 37077 Göttingen, Germany
[3]Cluster of Excellence "Multiscale Bioimaging: from Molecular Machines to Networks of Excitable Cells" (MBExC), University of Göttingen, 37077 Göttingen, Germany
[4]Bioanalytical Mass Spectrometry Group, Max Planck Institute for Multidisciplinary Sciences, 37077 Göttingen, Germany
[5]Department of Molecular Neurobiology, Max Planck Institute for Multidisciplinary Sciences, 37075 Göttingen, Germany
[6]Facility for Light Microscopy, Max Planck Institute for Multidisciplinary Sciences, 37077 Göttingen, Germany
[7]Quantitative and Systems Biology Group, Max Planck Institute for Multidisciplinary Sciences, 37077 Göttingen, Germany
[8]Kinderwunschzentrum Göttingen, 37081 Göttingen, Germany
[9]Institute of Clinical Chemistry, University Medical Center Göttingen, 37075 Göttingen, Germany
[10]Göttingen Center for Molecular Biosciences, Georg-August University Göttingen, 37077 Göttingen, Germany
[11]Faculty of Physics, Georg-August-Universität Göttingen, 37077 Göttingen, Germany
[12]Present address: Department of Reproductive Endocrinology, University Hospital Zurich, University of Zurich, Schlieren 8952, Switzerland
[13]Lead contact
*Correspondence: melina.schuh@mpinat.mpg.de
https://doi.org/10.1016/j.cell.2023.10.003

SUMMARY

Mammalian oocytes are filled with poorly understood structures called cytoplasmic lattices. First discovered in the 1960s and speculated to correspond to mammalian yolk, ribosomal arrays, or intermediate filaments, their function has remained enigmatic to date. Here, we show that cytoplasmic lattices are sites where oocytes store essential proteins for early embryonic development. Using super-resolution light microscopy and cryoelectron tomography, we show that cytoplasmic lattices are composed of filaments with a high surface area, which contain PADI6 and subcortical maternal complex proteins. The lattices associate with many proteins critical for embryonic development, including proteins that control epigenetic reprogramming of the preimplantation embryo. Loss of cytoplasmic lattices by knocking out PADI6 or the subcortical maternal complex prevents the accumulation of these proteins and results in early embryonic arrest. Our work suggests that cytoplasmic lattices enrich maternally provided proteins to prevent their premature degradation and cellular activity, thereby enabling early mammalian development.

INTRODUCTION

During their growth phase, oocytes accumulate proteins and other compounds to reprogram the zygote and support early embryogenesis.[1–4] The maternally supplied compounds are crucial for embryonic development, yet how mammalian oocytes accumulate and store proteins is not known.

Protein storage in oocytes has been predominantly studied in non-mammalian systems. Oviparous animals accumulate the yolk protein vitellogenin in a membrane-enclosed yolk sac.[5,6] Plant seeds have protein storage vacuoles that accumulate globulins and albumins to support germination.[7–9] Storing proteins within yolk sacs or protein storage vacuoles prevents protein degradation and misfolding and allows the accumulation

of the stored proteins.[5,10] Yeast and some mammalian somatic cells transiently store metabolic enzymes as polymers during times of poor nutrient supply or stress.[11–15] Storage within polymers has been proposed to protect the enzymes against degradation and to ensure that the enzymes are readily available upon stress relief.[16–19] Protein storage can thus be achieved by the separation of proteins from the cytosol into polymers or membrane-enclosed compartments.

The cytoplasm of mammalian oocytes and preimplantation embryos is filled with highly abundant structures called cytoplasmic lattices, which have only been visualized by electron microscopy (EM).[20,21] Cytoplasmic lattices were first discovered in the 1960s[22,23] and have puzzled scientists ever since, as their function and composition remain enigmatic. When cytoplasmic lattices
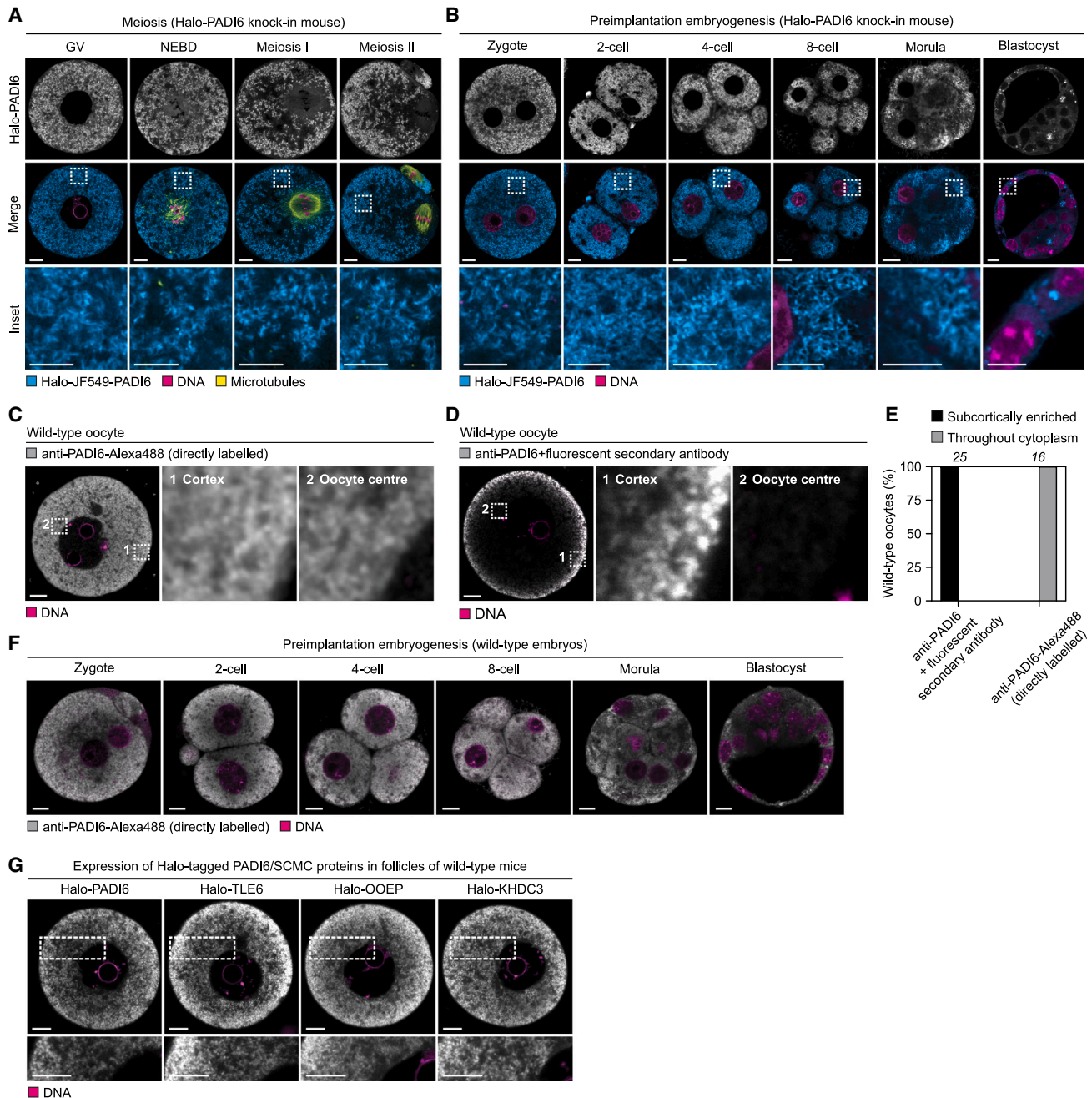
Cell
Article

Figure 1. PADI6 and subcortical maternal complex (SCMC) proteins are distributed throughout the oocyte cytoplasm

(A) Representative micrographs of HaloTag-JF549-PADI6 (cyan) mouse oocytes fixed at GV, nuclear envelope breakdown (NEBD), meiosis I, and meiosis II stages of meiosis. DNA (magenta), microtubules (yellow).

(B) Representative micrographs of HaloTag-JF549-PADI6 (cyan) mouse embryos at different stages of preimplantation embryogenesis. DNA, magenta. Scale bars of insets, 5 μm. Other scale bars, 10 μm.

(C) Representative micrograph of mouse wild-type GV oocytes stained with a directly coupled PADI6-Alexa 488 antibody (gray). DNA (magenta). Scale bar, 10 μm.

(D) Representative micrograph of mouse wild-type GV oocytes stained with an anti-PADI6 antibody followed by a secondary antibody (gray). DNA (magenta). Scale bar, 10 μm.

(E) Quantification of subcellular localization of PADI6 in oocytes stained with either an anti-PADI6 antibody followed by a secondary antibody or a directly coupled PADI6-Alexa 488 antibody. Number of oocytes analyzed indicated in italics.

(F) Representative micrographs of wild-type preimplantation mouse embryos. Embryos were labeled with a directly coupled anti-PADI6-Alexa 488 antibody (gray) and DNA (magenta). Scale bars, 10 μm.

Cell
Article

CellPress
OPEN ACCESS

were first discovered, they were described as "yolk plates" or "cytoplasmic sheets" of unknown composition and function. Later reports suggested that cytoplasmic lattices were composed of ribosomes arranged as beads on a string, potentially serving as a ribosome reservoir for oocytes and embryos.[24–27] In the 1990s, the cytoplasmic lattices were proposed to be oocyte-specific intermediate filament assemblies related to keratin.[28,29] In the early 2000s, several studies identified oocyte-specific proteins that are essential for the formation of cytoplasmic lattices. These proteins were PADI6 (peptidylarginine deiminase 6) and the "subcortical maternal complex" (SCMC), which consists of maternally encoded proteins, including NLRP5 (NACHT, LRR, and PYD domains containing protein 5; MATER), TLE6 (transducin-like enhancer 6), OOEP (oocyte-expressed protein; FLOPED), KHDC3 (KH-domain-containing protein 3; FILIA), NLRP4f (NACHT, LRR, and PYD domains containing protein 4f), and ZBED3 (zinc-finger BED-type containing 3).[30–33] Loss of PADI6 or SCMC proteins prevents cytoplasmic lattice formation and inhibits embryo development.[30–35] PADI6 and SCMC proteins are enriched under the oocyte cortex in immunofluorescence micrographs.[27,30,36] The subcortical enrichment of PADI6 and SCMC proteins differs from the localization of cytoplasmic lattices, which are uniformly distributed throughout the cytoplasm in electron micrographs.[20,37] However, some studies report increased detection of SCMC proteins in the cytoplasm upon oocyte detergent treatment or short antibody incubation,[35,38] and immunogold particles directed against PADI6, NLRP5, and OOEP overlapped with cytoplasmic lattices,[34,35,39] suggesting that at least a fraction of the proteins could be located in the cytoplasm. From the divided current literature, it is unclear whether PADI6 and the SCMC only regulate cytoplasmic lattice assembly from the subcortical region or whether they contribute more directly to cytoplasmic lattice assembly.[3,35,40,41]

Although the function of cytoplasmic lattices remains unclear, there is substantial evidence that cytoplasmic lattices are critical for both mouse and human reproduction. Mouse embryos conceived by mothers with mutations in *Padi6* or SCMC genes lack cytoplasmic lattices and arrest during preimplantation development.[30–35,42] Cytoplasmic lattices have thus been inferred as essential for preimplantation development.

In addition, mutations in the *PADI6* and SCMC genes are well-established genetic causes of human infertility.[3,4] Human embryos conceived by women with *PADI6* or SCMC mutations stop developing shortly after fertilization or develop into a hydatidiform mole, an abnormally developing embryo characterized by severe trophoblast hyperproliferation.[3,43] In rare cases, the embryos develop to term, but these children are diagnosed with multilocus imprinting disorders.[3,44] Both hydatidiform moles and multilocus imprinting disorders are caused by a loss of methylation marks on the embryonic genome.[45,46] However, the origin of hypomethylation in these embryos is unclear.

Despite the importance of the cytoplasmic lattices, PADI6, and SCMC proteins for successful embryonic development, their function and interconnection have remained elusive. In this study, we hence set out to investigate the function and organization of cytoplasmic lattices and their link to PADI6 and SCMC proteins in mammalian oocytes.

RESULTS

PADI6 and SCMC proteins are distributed throughout the oocyte cytoplasm

We first addressed the long-standing question of where PADI6 and SCMC proteins localize in oocytes. To determine the subcellular localization of PADI6 without immunofluorescence staining, we generated a knockin mouse line with a HaloTag sequence inserted into the endogenous locus of the *Padi6* gene (Figure S1A). The Halo-PADI6 fusion protein was expressed at a similar level as unmodified PADI6 in oocytes (Figure S1B). The number of oocytes retrieved from homozygous (p/p) and heterozygous (p/+) knockin females was comparable to that of wild-type animals (Figure S1C). p/+ females had litter sizes comparable to wild-type females, whereas p/p females were subfertile (Figure S1D). We thus used p/+ females to investigate the localization of the reporter protein in oocytes and during embryo preimplantation development. Previous light-microscopy-based studies reported a diffuse enrichment of PADI6 and SCMC proteins under the oocyte cortex.[27,30,47] Whether PADI6 and other SCMC proteins are arranged in distinct structures could not yet be assessed by light microscopy. To overcome this obstacle, we optimized labeling protocols using the knockin Halo-PADI6 line combined with Airyscan super-resolution microscopy. Unexpectedly, we found that Halo-JaneliaFluor549 labeled Halo-PADI6 organized into distinct structures and was distributed not just at the subcortex but also throughout the cytoplasm in oocytes and in preimplantation embryos until embryo compaction, after which the protein signal decreased, reaching the lowest level at the blastocyst stage (Figures 1A and 1B). The decreasing levels of Halo-PADI6 during preimplantation development are consistent with a previous study of PADI6 protein levels using immunoblotting of wild-type embryos.[39]

In contrast, when we detected Halo-PADI6 by immunofluorescence with a primary anti-PADI6 antibody and a fluorescent secondary antibody, we observed strong enrichment in the subcortical region (Figures S1E–S1G). However, a directly labeled anti-PADI6-Alexa 488 primary antibody revealed cytoplasmic PADI6 in wild-type oocytes, similar to the Halo-PADI6 signal (Figures 1C and S1H), indicating that the apparent subcortical enrichment observed by immunofluorescence was due to the secondary antibody (Figures 1D and 1E). Secondary antibodies bind to multiple regions of the primary antibody, thereby creating an "extended coat" around them, which likely limits penetration into the inner region of the oocyte when abundant

(G) Representative micrographs of germinal vesicle stage wild-type mouse oocytes expressing HaloTag-PADI6, -TLE6, -OOEP, and -KHDC3 mRNA constructs injected at the primary follicle stage. HaloTag-JF549 (gray), DNA (magenta). Scale bars, 10 μm.

All insets are magnifications of outlined regions. All images acquired with a laser scanning confocal microscope. Images in (A), (B), and (G) were acquired in Airyscan mode.

See also Figure S1.

proteins such as PADI6 or SCMC components are stained by immunofluorescence (Figure S1I). Direct labeling of primary antibodies is thus a valuable tool to validate the potential enrichment of proteins in subcortical regions in large cells such as oocytes. Importantly, similar to Halo-PADI6, the endogenous, unmodified PADI6 was cytoplasmic throughout embryo development until compaction in wild-type embryos (Figure 1F).

To investigate the subcellular distribution of PADI6 and SCMC proteins further, we microinjected mRNAs encoding Halo-tagged PADI6 and SCMC reporter proteins into oocytes growing within follicles[48] because PADI6 and SCMC proteins as well as cytoplasmic lattices emerge during oocyte growth.[27,30] Halo-PADI6, Halo-TLE6, Halo-OOEP, and Halo-KHDC3 fusion proteins expressed for 9 days during follicle growth showed a similar localization pattern as endogenously expressed Halo-PADI6 in the knockin line, with assembly into distinct structures throughout the cytoplasm (Figure 1G). In contrast, expression of the same fusion proteins for only 3 h in fully grown germinal vesicle (GV)-stage oocytes resulted in a much more diffuse signal with little (PADI6) or no (TLE6, OOEP, and KHDC3) visible incorporation into distinct structures (Figure S1J). This could indicate slow turnover of PADI6 and SCMC proteins on the structures but could also be explained by poorer detectability of the structures upon acute overexpression of the fluorescently tagged proteins in the cytoplasm. Fluorescence recovery after photobleaching experiments after follicle culture revealed low recovery of the mClover3-PADI6 signal over 2 min, with an immobile fraction of 66.0% ±7.6% (Figures S1K and S1L). Longer observations after photobleaching were precluded by the drift of cytoplasmic lattices within the cytoplasm. Taken together, our data show that PADI6 and SCMC proteins assemble into distinct structures that fill the entire cytoplasm in oocytes.

PADI6 and SCMC proteins are essential components of cytoplasmic lattices

Next, we analyzed the three-dimensional (3D) organization of the PADI6 and SCMC structures. To resolve the small structures at higher resolution, we expanded mouse oocytes by adapting existing protein-retention expansion microscopy protocols (pro-ExM).[49–51] The gels were expanded with a factor of 4.4, as calculated by measuring the size of different cellular structures pre and post expansion, including the meiotic spindle and the nucleus (Figure S2A). The expanded oocytes were labeled for PADI6 and the SCMC proteins TLE6, NLRP5, OOEP, and KHDC3 (Figures 2A–2D). Airyscan imaging of the expanded samples revealed that PADI6 and the SCMC proteins were organized into fibers that filled the cytoplasm. The fibers contained both PADI6 and the SCMC proteins, which were densely distributed along the entire length of the fibers (Figures 2A–2D).

To resolve the fiber 3D organization at higher axial resolution, we simultaneously immunostained oocytes for PADI6, NLRP5, and TLE6 to achieve high labeling density and then imaged the expanded oocytes by 3D stimulated emission depletion (STED) nanoscopy (ExSTED)[52] (Figures 2E and 2F). We found that the PADI6/SCMC protein fibers were ~100-nm wide (Figure 2G) and on average ~700-nm long (Figure 2H) after dividing by the expansion factor. These dimensions were similar to two-dimen-

sional (2D) EM data of cytoplasmic lattices in mouse oocytes.[53] To evaluate the expansion homogeneity and validity of the extracted measurements, we quantified the error of length measurements by interrogating the sample deformation after ExM. To this end, we labeled either interphase or spindle microtubules and imaged the oocytes before and after expansion. Subsequently, post-ExM images were registered to the pre-ExM images through similarity or affine registration, followed by non-rigid B-spline registration[54,55] (Figures S2C–S2J; STAR Methods). The calculated expansion factor from the similarity scaling measurements was similar to that of the manual landmark measurements (Figure S2B). Within the range of cytoplasmic lattice fiber length (~700 nm), the error was small (<5%) (Figure S2F).

Given the dimensions of the PADI6/SCMC protein fibers, their uniform cytoplasmic distribution, and the requirement of PADI6 and SCMC proteins for cytoplasmic lattice formation,[34,35,40] we asked whether the PADI6/SCMC protein fibers are the same structures as cytoplasmic lattices. To this end, we combined N-hydroxysuccinimide (NHS) ester labeling from pan-ExM[55] to the pro-ExM protocol in order to visualize PADI6 and SCMC proteins within the ultrastructural context of the ooplasm. We first co-labeled expanded GV mouse oocytes with an anti-PADI6 antibody and a fluorophore-coupled NHS ester (NHS-ATTO488). The NHS ester binds to primary amines on proteins and hence labels protein-dense regions in cells, yielding images that resemble EM micrographs.[55] Strikingly, PADI6 co-localized with cytoplasmic, protein-dense structures that resembled cytoplasmic lattices observed in EM micrographs (Figure 2I). To determine whether the fibrous, protein-dense structures are indeed cytoplasmic lattices, we stained $Padi6^{-/-}$ and $Tle6^{-/-}$ oocytes, which lack cytoplasmic lattices,[32,33] with NHS-ATTO488. The protein-dense, fibrous structures were absent in both mutant cytoplasms but not in the wild-type cytoplasm (Figure 2J), indicating that the structures labeled by the NHS ester are cytoplasmic lattices. Together, these data indicate that cytoplasmic lattices are fibers that are rich in PADI6 and SCMC proteins.

Cytoplasmic lattices are fibers of short, twisted filaments

To investigate the overall 3D organization of cytoplasmic lattices in more detail, we assessed the overall lattice organization by room temperature electron tomography (RT-ET) (Figures 3A–3C). Tomogram segmentation and filament tracing of the lattices in ~500-nm-thick plastic-embedded sections of mouse oocytes revealed ~700-nm-long fibers (Figure 3C), consistent with our 3D ExSTED analysis. The fibers were a prominent structural feature, occupying ~10% of the cytoplasmic volume. The fibers were composed of multiple shorter arched filaments (~200 nm in length) (Figure 3C; Video S1). These filaments were individually stacked and slightly twisted relative to each other, resulting in an overall helical appearance of the fiber (Figure 3B; Video S1). The number of filaments within a fiber cross-section varied from 5 to 40 filaments, with an average of 22 filaments (Figures 3D and S3A).

To gain further insights into the architecture of the cytoplasmic lattices, we imaged vitrified mouse oocytes by cryo-ET. This technique enables the visualization of cellular complexes *in situ*
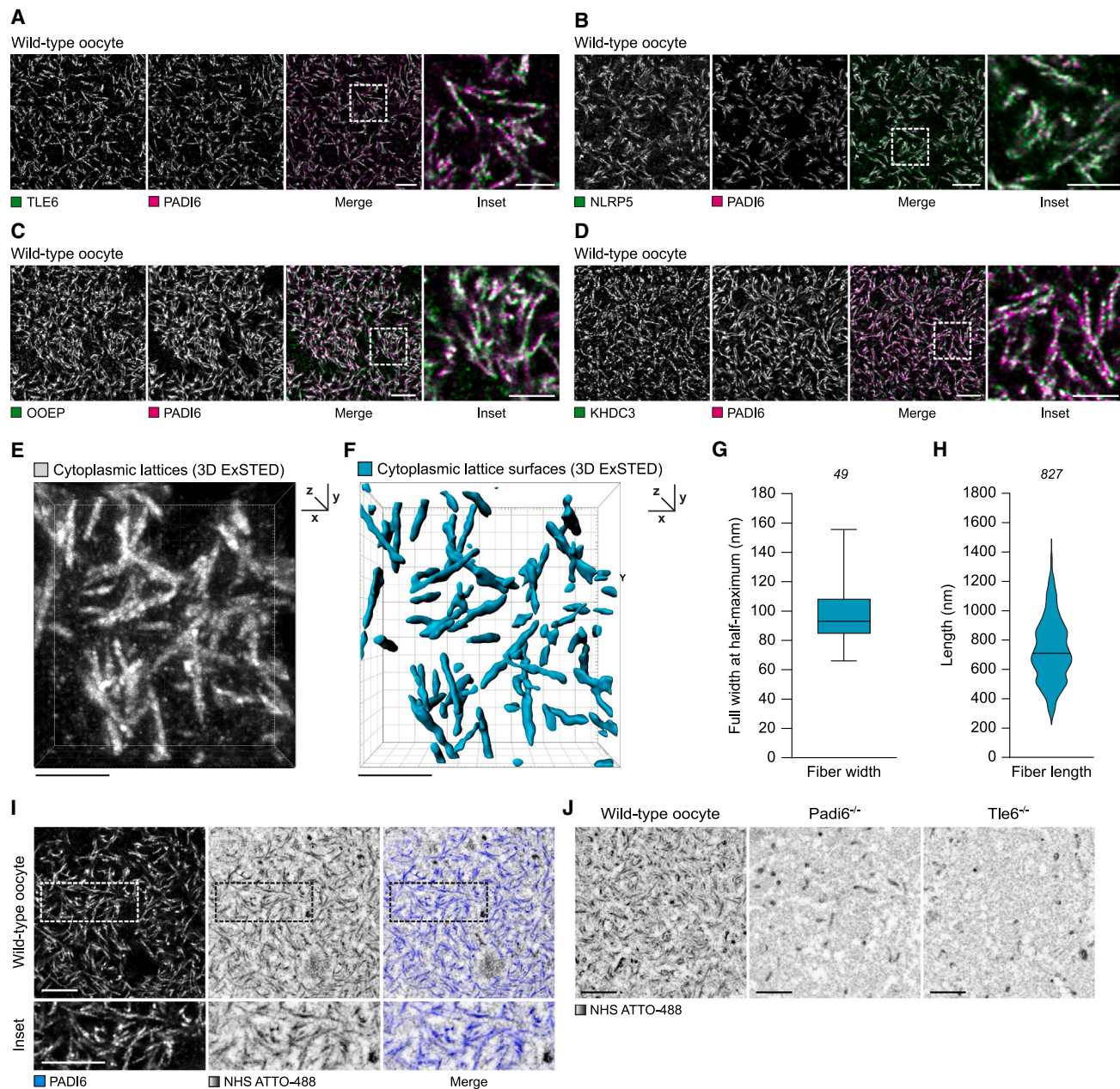
Figure 2. Cytoplasmic lattices are PADI6- and SCMC-protein-rich fibers

(A–D) Representative ExM micrographs of mouse GV oocytes co-labeled with anti-PADI6 (magenta) and anti-TLE6, -NLRP5, -OOEP, or -KHDC3, respectively (green). Scale bars, 2 μm. Scale bars of insets, 1 μm.

(E) Raw 3D ExSTED volume of an expanded mouse oocyte co-stained using rabbit anti-PADI6, -TLE6, and -NLRP5 antibodies, followed by an anti-rabbit STAR 635 secondary antibody. Scale bar, 2 μm.

(F) Isosurface reconstruction of 3D ExSTED cytoplasmic lattice-segmented volumes from (E). 3D volumes were segmented using Ilastik software. Scale bar, 2 μm.

(G) Quantification of cytoplasmic lattice fiber width. Number of individual fibers measured is indicated in italics. Experiment mean is indicated with a vertical line. Whiskers represent minimum and maximum values. Reported fiber width measurements were corrected for the expansion factor.

(H) Quantification of cytoplasmic lattice fiber length. Number of individual filaments measured is indicated in italics. Experiment mean indicated with vertical line. Fiber length measurements were corrected for the expansion factor.

(I) Representative pan-ExM images of mouse GV oocytes. Expanded oocytes were labeled for PADI6 (blue) and an NHS ester coupled to ATTO-488 (gray-inverted look-up table). Scale bars, 2 μm.

(J) Representative pan-ExM images, of wild-type, $Padi6^{-/-}$, and $Tle6^{-/-}$ mouse oocytes labeled with NHS-Atto488 (gray-inverted look-up table). Scale bars, 2 μm.

All scale bars for ExM micrographs, or ExM-derived images, are corrected for the expansion factor.

Images in (A)–(D), (I), and (J) were acquired on a laser scanning confocal microscope.

See also Figure S2.
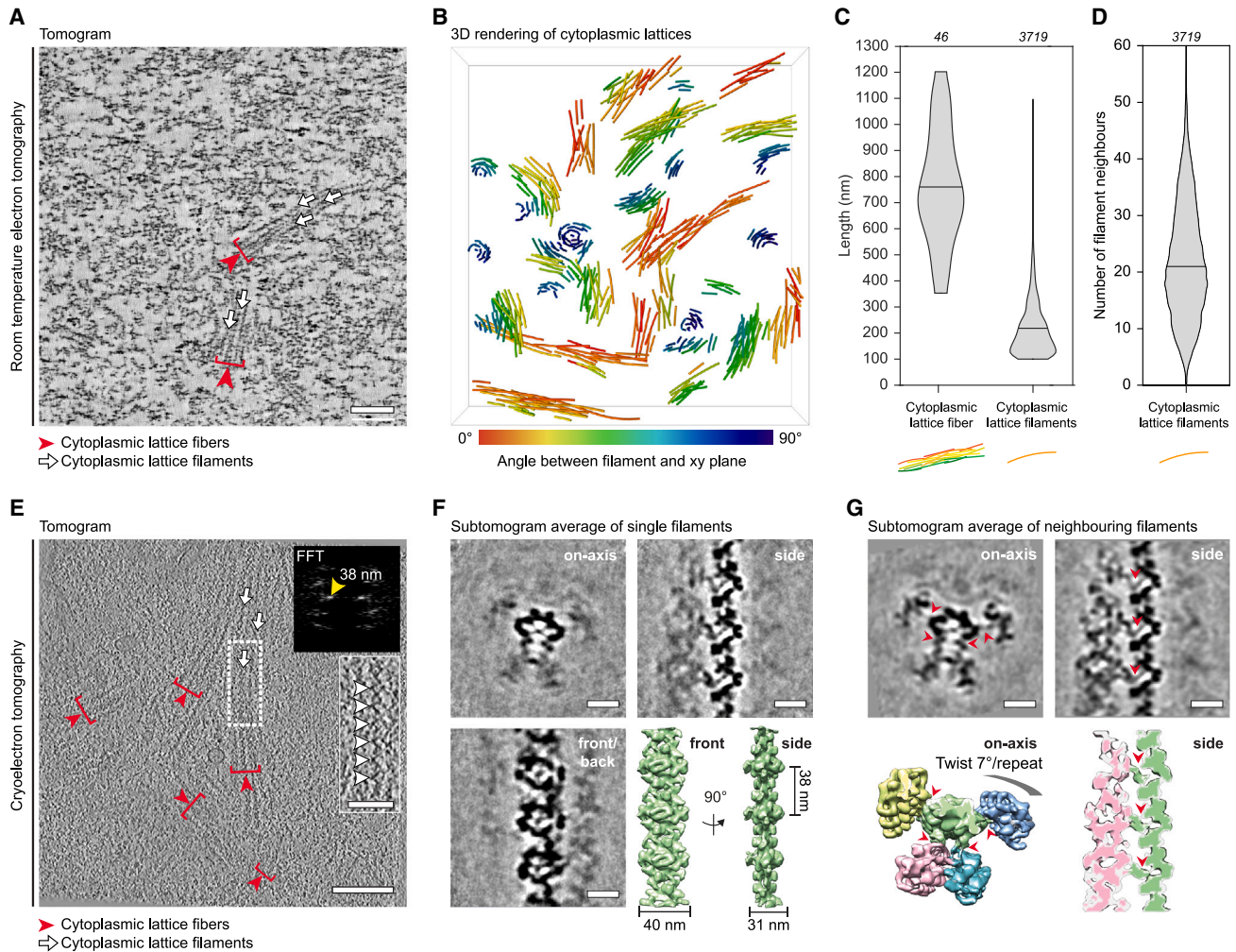
Cell
Article

Figure 3. Electron tomography reveals the organization and structure of cytoplasmic lattices

(A–D) Room temperature electron tomography (RT-ET) of cytoplasmic lattice fibers.

(A) 1.22-nm-thick tomographic slice. Cytoplasmic lattice fibers (red arrowheads) are built by individual filaments (white arrows).

(B) 3D rendering of the filaments shown in the tomogram in (A). The color scale depicts the angle between the xy plane and the filament: 0° (warm colors) represents filaments in the xy plane, 90° (cold colors) represents filaments perpendicular to the image plane.

(C and D) Statistical analysis of cytoplasmic fiber length, filament length, and number of cross-sectional neighbors in a cytoplasmic lattice fiber. Violin plots visualize the distribution, and horizontal lines mark the mean. Number of bundles (not contacting the edge of the tomogram, and in the xy plane) = 46; number of filaments = 3,719. Data extracted from a total of 7 tomograms.
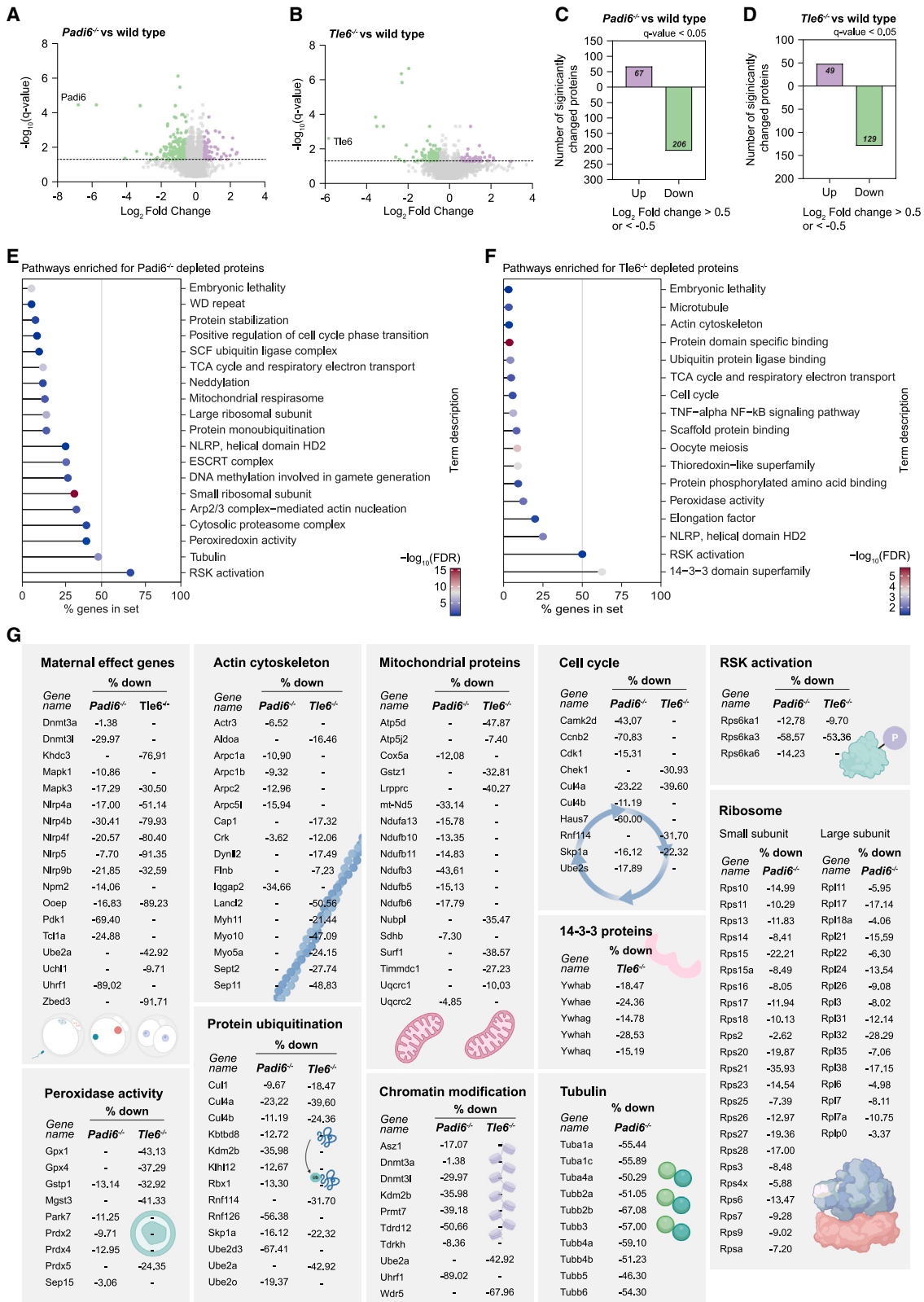
(E–G) Cryoelectron tomography of cytoplasmic lattice fibers.

(E) 1.46-nm-thick tomographic slice. Cytoplasmic lattice fibers (red arrowheads) are built by individual filaments (white arrows). Inset, bottom: high magnification image of a cytoplasmic lattice filament with repetitive elements (white arrowheads). The inset shows the boxed area in a different tomographic slice. Inset, top: corresponding Fourier transform showing a periodicity of 38 nm.

(F) Subtomogram average of cytoplasmic lattice filaments with a mask focusing the alignment on a single filament. Cross-sections of the averaged volume along the filament axis (upper left), from the filament side (upper right) and front (bottom left). Bottom right: isosurface rendering of the filament average in front and side views. The dimensions of the filament cross-sections and repeating units are indicated.

(G) Subtomogram average of cytoplasmic lattice filaments with a mask focusing the alignment on neighboring filaments. Cross-sections of the averaged volume along the filament axis (upper left) and from the filament side (upper right). Arrowheads (red) indicate densities connecting neighboring filaments. Lower left: isosurface rendering of the on-axis view. The neighboring filaments are distinguished by different colors. Bottom right: cross-sectional view through the iso-surface rendering, visualizing the connections between neighboring filaments (red arrowheads). Scale bars, 250 nm in (A) and (E), 100 nm (E, bottom inset), 25 nm in (F) and (G); field of view, 2,350 nm in (B).

See also Figures S3 and S4, Videos S1, S2, S3, and S4, and STAR Methods.

A — $Padi6^{-/-}$ vs wild type (axes: $-\log_{10}$(q-value) vs $\log_2$ Fold Change; labeled point: Padi6)

B — $Tle6^{-/-}$ vs wild type (axes: $-\log_{10}$(q-value) vs $\log_2$ Fold Change; labeled point: Tle6)

C — $Padi6^{-/-}$ vs wild type; q-value < 0.05; Number of significantly changed proteins; Up 67, Down 206; $\log_2$ Fold change > 0.5 or < -0.5

D — $Tle6^{-/-}$ vs wild type; q-value < 0.05; Up 49, Down 129; $\log_2$ Fold change > 0.5 or < -0.5

E — Pathways enriched for Padi6⁻/⁻ depleted proteins (Term description vs % genes in set; color = $-\log_{10}$(FDR))

Terms: Embryonic lethality; WD repeat; Protein stabilization; Positive regulation of cell cycle phase transition; SCF ubiquitin ligase complex; TCA cycle and respiratory electron transport; Neddylation; Mitochondrial respirasome; Large ribosomal subunit; Protein monoubiquitination; NLRP, helical domain HD2; ESCRT complex; DNA methylation involved in gamete generation; Small ribosomal subunit; Arp2/3 complex–mediated actin nucleation; Cytosolic proteasome complex; Peroxiredoxin activity; Tubulin; RSK activation

F — Pathways enriched for Tle6⁻/⁻ depleted proteins (Term description vs % genes in set; color = $-\log_{10}$(FDR))

Terms: Embryonic lethality; Microtubule; Actin cytoskeleton; Protein domain specific binding; Ubiquitin protein ligase binding; TCA cycle and respiratory electron transport; Cell cycle; TNF−alpha NF−kB signaling pathway; Scaffold protein binding; Oocyte meiosis; Thioredoxin−like superfamily; Protein phosphorylated amino acid binding; Peroxidase activity; Elongation factor; NLRP, helical domain HD2; RSK activation; 14−3−3 domain superfamily

G

Maternal effect genes

Gene name	% down $Padi6^{-/-}$	% down $Tle6^{-/-}$
Dnmt3a	-1.38	-
Dnmt3l	-29.97	-
Khdc3	-	-76.91
Mapk1	-10.86	-
Mapk3	-17.29	-30.50
Nlrp4a	-17.00	-51.14
Nlrp4b	-30.41	-79.93
Nlrp4f	-20.57	-80.40
Nlrp5	-7.70	-91.35
Nlrp9b	-21.85	-32.59
Npm2	-14.06	-
Ooep	-16.83	-89.23
Pdk1	-69.40	-
Tcl1a	-24.88	-
Ube2a	-	-42.92
Uchl1	-	-9.71
Uhrf1	-89.02	-
Zbed3	-	-91.71

Actin cytoskeleton

Gene name	% down $Padi6^{-/-}$	% down $Tle6^{-/-}$
Actr3	-6.52	-
Aldoa	-	-16.46
Arpc1a	-10.90	-
Arpc1b	-9.32	-
Arpc2	-12.96	-
Arpc5l	-15.94	-
Cap1	-	-17.32
Crk	-3.62	-12.06
Dynll2	-	-17.49
Flnb	-	-7.23
Iqgap2	-34.66	-
Lancl2	-	-50.56
Myh11	-	-21.44
Myo10	-	-47.09
Myo5a	-	-24.15
Sept2	-	-27.74
Sep11	-	-48.83

Mitochondrial proteins

Gene name	% down $Padi6^{-/-}$	% down $Tle6^{-/-}$
Atp5d	-	-47.87
Atp5j2	-	-7.40
Cox5a	-12.08	-
Gstz1	-	-32.81
Lrpprc	-	-40.27
mt-Nd5	-33.14	-
Ndufa13	-15.78	-
Ndufb10	-13.35	-
Ndufb11	-14.83	-
Ndufb3	-43.61	-
Ndufb5	-15.13	-
Ndufb6	-17.79	-
Nubpl	-	-35.47
Sdhb	-7.30	-
Surf1	-	-38.57
Timmdc1	-	-27.23
Uqcrc1	-	-10.03
Uqcrc2	-4.85	-

Cell cycle

Gene name	% down $Padi6^{-/-}$	% down $Tle6^{-/-}$
Camk2d	-43.07	-
Ccnb2	-70.83	-
Cdk1	-15.31	-
Chek1	-	-30.93
Cul4a	-23.22	-39.60
Cul4b	-11.19	-
Haus7	-60.00	-
Rnf114	-	-31.70
Skp1a	-16.12	-22.32
Ube2s	-17.89	-

RSK activation

Gene name	% down $Padi6^{-/-}$	% down $Tle6^{-/-}$
Rps6ka1	-12.78	-9.70
Rps6ka3	-58.57	-53.36
Rps6ka6	-14.23	-

14-3-3 proteins

Gene name	% down $Tle6^{-/-}$
Ywhab	-18.47
Ywhae	-24.36
Ywhag	-14.78
Ywhah	-28.53
Ywhaq	-15.19

Protein ubiquitination

Gene name	% down $Padi6^{-/-}$	% down $Tle6^{-/-}$
Cul1	-9.67	-18.47
Cul4a	-23.22	-39.60
Cul4b	-11.19	-24.36
Kbtbd8	-12.72	-
Kdm2b	-35.98	-
Klhl12	-12.67	-
Rbx1	-13.30	-
Rnf114	-	-31.70
Rnf126	-56.38	-
Skp1a	-16.12	-22.32
Ube2d3	-67.41	-
Ube2a	-	-42.92
Ube2o	-19.37	-

Chromatin modification

Gene name	% down $Padi6^{-/-}$	% down $Tle6^{-/-}$
Asz1	-17.07	-
Dnmt3a	-1.38	-
Dnmt3l	-29.97	-
Kdm2b	-35.98	-
Prmt7	-39.18	-
Tdrd12	-50.66	-
Tdrkh	-8.36	-
Ube2a	-	-42.92
Uhrf1	-89.02	-
Wdr5	-	-67.96

Tubulin

Gene name	% down $Padi6^{-/-}$
Tuba1a	-55.44
Tuba1c	-55.89
Tuba4a	-50.29
Tubb2a	-51.05
Tubb2b	-67.08
Tubb3	-57.00
Tubb4a	-59.10
Tubb4b	-51.23
Tubb5	-46.30
Tubb6	-54.30

Peroxidase activity

Gene name	% down $Padi6^{-/-}$	% down $Tle6^{-/-}$
Gpx1	-	-43.13
Gpx4	-	-37.29
Gstp1	-13.14	-32.92
Mgst3	-	-41.33
Park7	-11.25	-
Prdx2	-9.71	-
Prdx4	-12.95	-
Prdx5	-	-24.35
Sep15	-3.06	-

Ribosome

Small subunit Gene name	% down $Padi6^{-/-}$	Large subunit Gene name	% down $Padi6^{-/-}$
Rps10	-14.99	Rpl11	-5.95
Rps11	-10.29	Rpl17	-17.14
Rps13	-11.83	Rpl18a	-4.06
Rps14	-8.41	Rpl21	-15.59
Rps15	-22.21	Rpl22	-6.30
Rps15a	-8.49	Rpl24	-13.54
Rps16	-8.05	Rpl26	-9.08
Rps17	-11.94	Rpl3	-8.02
Rps18	-10.13	Rpl31	-12.14
Rps2	-2.62	Rpl32	-28.29
Rps20	-19.87	Rpl35	-7.06
Rps21	-35.93	Rpl38	-17.15
Rps23	-14.54	Rpl6	-4.98
Rps25	-7.39	Rpl7	-8.11
Rps26	-12.97	Rpl7a	-10.75
Rps27	-19.36	Rplp0	-3.37
Rps28	-17.00		
Rps3	-8.48		
Rps4x	-5.88		
Rps6	-13.47		
Rps7	-9.28		
Rps9	-9.02		
Rpsa	-7.20		

(legend on next page)

in unstained, frozen-hydrated conditions. No cryo-ET studies have been performed in oocytes so far, as their size (~75 μm in diameter in mice) prevents standard cryo-ET analysis. However, we recently showed that a brief incubation in a cryo-protective solution enables the vitrification of large biological specimens by plunge freezing.[56] For mouse oocytes, a cryo-protectant mixture of 7.5% dimethyl sulfoxide (DMSO) and 7.5% ethylene glycol (EG), commonly used in cryo-preservation of human oocytes,[57–61] was used for plunge freezing. Subsequently, we performed cryo-focused ion beam (cryo-FIB) milling to obtain lamellae of the oocyte cytoplasm for cryo-ET (Figure S4; see STAR Methods). The size of the oocytes prompted us to develop a "deep-FIBing" approach in which the cells were first milled perpendicular to the EM grid to reveal a clean surface from which lamellae were subsequently prepared (Figure S4A).

The dense array of cytoplasmic lattice filaments was also easily observed under these near-native conditions (Figure 3E; Video S2). Similar to the RT-ET samples, cryo-ET tomogram segmentation showed the overall helical nature of the fibers, composed of multiple stacked filaments (Figure S3B; Video S3). Filaments within the fibers were ~200-nm long (Figure S3C). Persistence length analysis indicated that the stiffness of the filaments was in the range of amyloid fibrils[62,63] and microtubules[64] (Figure S3D).

The filaments showed an apparent periodicity of 38 nm (Figure 3E, inset), prompting us to investigate their organization in more detail by subtomogram averaging. Subvolumes extracted along the filaments were aligned and averaged, yielding a map of approximately 30 Å global resolution (Figures 3F and S3E–S3G). This showed that the filaments adopt an elliptical shape with a 40-nm-long major axis ("front/back") and a 31-nm minor axis ("side") (Figure 3F). The structure rules out the possibility that cytoplasmic lattices are composed of stacked ribosomes (Figure S3H), as was previously proposed.[24,26] Although the presence of the neighboring filaments was apparent in the initial average (Figure 3F, orthoslices), additional rounds of local alignment with a larger mask were needed to identify them clearly (Figures 3G and S3I). This showed a group of five filaments with discernible densities connecting them (Figures 3G and S3I, arrowheads). Interestingly, the interactions between the filaments follow a unique configuration, whereby the back surface of one filament contacts the side of neighboring filaments (Figures 3G and S3I, arrowheads; Video S4). This geometry could form the basis for the assembly of filaments into fibers.

In summary, our data show that cytoplasmic lattices are composed of repetitive arched filaments that interact to form a twisting fiber. The average filament map indicates a consistent and ordered core unit. Our ExM STED analysis indicates that the cytoplasmic lattices contain PADI6 and SCMC proteins, which are among the most abundant proteins in oocytes,[65] consistent with the high abundance of cytoplasmic lattices. Given that PADI6 and SCMC proteins are necessary for cytoplasmic lattice assembly, these proteins might constitute core components of the filaments.

PADI6 and SCMC proteins are required to accumulate hundreds of maternally provided proteins in oocytes

To investigate the functions of PADI6 and SCMC proteins in oocytes, we performed quantitative mass spectrometry (MS) analysis of wild-type oocytes and of oocytes from $Tle6^{-/-}$ and $Padi6^{-/-}$ mouse lines where cytoplasmic lattices do not form (Figures 4A and 4B). We found that 665 out of 3,788 detected proteins in $Padi6^{-/-}$ oocytes and 234 out of 3,508 detected proteins in $Tle6^{-/-}$ oocytes were significantly less abundant compared with their levels in wild type (Figures S5A and S5B). Of these, 206 and 129 proteins were significantly reduced by more than ~30% in $Padi6^{-/-}$ and $Tle6^{-/-}$ oocytes, respectively, when compared with their levels in wild-type oocytes (corresponding to a $\log_2$ fold change < −0.5). In contrast, only 67 ($Padi6^{-/-}$) and 49 ($Tle6^{-/-}$) proteins were increased by more than ~30% (corresponding to a $\log_2$ fold change > 0.5) (Figures 4C and 4D). Although we observed changes in mRNA abundance in $Padi6^{-/-}$ and $Tle6^{-/-}$ oocytes compared with wild type (Figures S5C and S5D), the changes in protein and mRNA abundance were not concordant (Figures S5E and S5F), and the vast majority of depleted or increased proteins did not display a significant change in transcript abundance.

Strikingly, ~30% of the depleted proteins were encoded by transcripts classified as "maternal RNA" in the Database of Transcriptome in the Mouse Early Embryo (DBTMEE) transcript database[66] (Figures S5G and S5H). These maternally provided RNA transcripts have the highest levels in the mature egg and decrease rapidly upon fertilization, without replenishment during the first stages of preimplantation development. Moreover, many of the depleted proteins were highly abundant in wild-type oocytes, and highly abundant proteins were more frequent in the collection of $Padi6^{-/-}$ and $Tle6^{-/-}$ depleted proteins than in the overall oocyte proteome (Figures S5I and S5J). Therefore, many of these proteins had key properties expected for maternally provided, stored proteins.

$Tle6^{-/-}$ oocytes contained near wild-type levels of PADI6, but were depleted of the other SCMC proteins (Figure S5K),

Figure 4. PADI6 and SCMC proteins are required to accumulate essential proteins in the oocyte

(A and B) Volcano plots representing differentially abundant proteins in $Padi6^{-/-}$ (A) or $Tle6^{-/-}$ (B) oocytes compared with wild type. Green dots represent proteins with a $\log_2$ fold change < −0.5 and a q value < 0.05. Purple dots represent proteins with a $\log_2$ fold change > 0.5 and a q value < 0.05. Gray line indicates q value = 0.05. Only proteins with >2 identified unique peptides were considered.

(C) Numeric quantification of colored data points in (A).

(D) Numeric quantification of colored data points in (B).

(E) Enriched terms after STRING analysis of $Padi6^{-/-}$ significantly depleted proteins (q value < 0.05). Dot color indicates the false discovery rate (FDR) given by $-\log_{10}(FDR)$.

(F) Enriched terms after STRING analysis of $Tle6^{-/-}$ significantly depleted proteins (q value < 0.05). Dot color indicates the FDR given by $-\log_{10}(FDR)$.

(G) Schematic representation of pathways enriched among depleted proteins in $Padi6^{-/-}$ and/or $Tle6^{-/-}$ oocytes. Percent decrease in protein level is indicated for each protein. Icons were generated with BioRender.com.

See also Figure S5.

consistent with previous studies showing that the entire SCMC complex is destabilized when one of the SCMC components is missing.[67] Vice versa, *Padi6*^{−/−} oocytes lacked PADI6 but still contained the SCMC proteins at near wild-type levels (Figure S5L). The proteins that were depleted in *Padi6*^{−/−} and *Tle6*^{−/−} oocytes overlapped partially but were largely distinct (Figure S5M). These data indicate that PADI6 and SCMC proteins can accumulate independently of each other in oocytes, together with distinct subsets of additional proteins.

We next used Search Tool for the Retrieval of Interacting Genes/Proteins (STRING) for pathway enrichment analysis[68] and found that the significantly depleted proteins in either *Padi6*^{−/−} or *Tle6*^{−/−} oocytes overlapped functionally (Figures 4E and 4F). Both *Padi6*^{−/−} and *Tle6*^{−/−} oocytes were depleted of known maternal factors important for the developmental progression of the early embryo[4] (Figure 4G). In addition, proteins involved in mitochondrial organization and metabolism, as well as actin- and microtubule-related proteins and peroxidase-activity-related proteins, were depleted in both mutants (Figures 4E and 4G). *Padi6*^{−/−} oocytes were additionally depleted of proteins required for DNA methylation (DNMT3a, DNMT3l, PRMT7), and both mutants showed lower levels of different chromatin-modification-related factors (KDM2B, UBE2D3, UHRF1, WDR5, UBE2A), which are crucial for the epigenetic regulation of early embryo development (Figures 4E and 4G), as well as ribosomal proteins (Figures 4E and 4G). In *Tle6*^{−/−} oocytes, five out of seven known 14-3-3 proteins were significantly reduced (Figures 4F and 4G). 14-3-3 proteins can form cup-like homo- and hetero-dimers and interact with hundreds of different proteins by binding to phosphorylated serine and threonine residues, thereby regulating a wide range of cellular processes.[69,70]

Together, our data establish that PADI6 and SCMC proteins are required to accumulate highly abundant proteins in oocytes, many of which are encoded by maternally supplied mRNAs.

Oocytes store proteins on cytoplasmic lattices

We next sought to investigate how PADI6 and SCMC proteins promote protein accumulation. Previous studies established that proteins need to be stored in a non-soluble state.[16–18] We thus hypothesized that soluble proteins are enriched on PADI6- and SCMC-dependent cytoplasmic lattices in a non-soluble state to allow for their accumulation.

To test this hypothesis, we examined a subset of proteins that were depleted to various extents in *Padi6*^{−/−} and *Tle6*^{−/−} oocytes, including α-tubulins, which were previously reported to associate with PADI6[40] and proteins involved in chromatin modification (UHRF1, KDM2B), chromatin reading (SPIN1), protein ubiquitination (SKP1, UBE2D3), cell signaling (14-3-3/YWAH), pluripotency maintenance (DPPA5), and the NLRP proteins NLRP4 and NLRP14 (Figures 5A, 5D, 5G, 5J, 5M, S6A, S6D, S6G, S6J, and S6M). We analyzed the localization of these proteins relative to our cytoplasmic lattice marker PADI6 in wild-type oocytes by immunofluorescence and ExM (Figures 5B, 5E, 5H, 5K, 5N, S6B, S6E, S6H, S6K, and S6N).

Strikingly, these proteins were enriched on the lattices, validating our hypothesis. To quantify the enrichment of the candidate proteins on the cytoplasmic lattices, we segmented the cytoplasmic lattices using PADI6 as a marker (Figures S6P and S6Q). We next calculated the fold enrichment by measuring the mean fluorescence intensity of the candidate proteins within and outside of the cytoplasmic lattice segmentation mask. We found that our probed candidates were enriched at least 1.5-fold within the cytoplasmic lattice mask (Figures 5C, 5F, 5I, 5L, 5O, S6C, S6F, S6I, S6L, S6O, and S7G). To ensure that the enriched protein signal on the cytoplasmic lattices is not an artifact of the ExM protocol, we also measured enrichment of CDK1 (cyclin-dependent kinase 1), a cytosolic protein unrelated to the lattices, as well as the mitochondrial protein UQCRB (ubiquinol-cytochrome *c* reductase binding protein), and found no enrichment on the lattice structure (Figures S7A–S7D). Similarly, exogenous expression of GFP followed by ExM and enrichment analysis showed no enrichment of the GFP protein on cytoplasmic lattices (Figures S7E and S7F).

As an additional control, we rotated the candidate protein channel by 90° and found that the signal was no longer enriched on the cytoplasmic lattices (Figures S7H–S7Q). Line profiles of individual cytoplasmic lattices revealed that the candidate proteins in the original images (gray line) localized along the lattices at regular intervals, often overlapping with the fluorescence signal of PADI6; this pattern was no longer visible in the rotated images (Figures S7G–S7Q).

Together, our data show that PADI6 and the SCMC are required to accumulate and store essential proteins that localize on cytoplasmic lattices, many of which are essential for preimplantation embryo development.[71–74] The proteins that are depleted in *Padi6*^{−/−} and *Tle6*^{−/−} oocytes have overlapping functions but are largely distinct (Figure 4G). Understanding how PADI6 and SCMC proteins drive the accumulation of distinct subsets of proteins will require extensive additional structural and functional studies. It is, for instance, possible that the lattices are composed of PADI6- and SCMC-dependent subunits that stabilize distinct subsets of maternal proteins and can assemble independently of each other but require each other in order to become arranged into cytoplasmic lattices.

Cytoplasmic lattices are composed of PADI6 and SCMC proteins and store UHRF1 in human oocytes

Next, we investigated whether cytoplasmic lattices are composed of PADI6 and SCMC proteins and also serve as sites for protein storage in human oocytes. To this end, we labeled expanded GV human oocytes with antibodies, as well as with a fluorescently labeled NHS ester, to detect PADI6 and different SCMC components. As expected, the NHS-ester-stained cytoplasmic lattices in human oocytes appeared shorter than those in mouse oocytes (Figure 6A). This is consistent with previous EM data of cytoplasmic lattices in human oocytes, showing that the structures appear like a fibrous mesh rather than easily distinguishable fibers as in rodents.[20] Importantly, PADI6 strongly co-localized with the cytoplasmic lattices in human oocytes (Figure 6A). Further, TLE6, PADI6, and NLRP5 co-localized in human oocytes, indicating that cytoplasmic lattices are composed of PADI6 and SCMC proteins in human oocytes (Figures 6B and 6C).

The embryos of women with mutations in *PADI6* or SCMC genes display phenotypes such as early developmental arrest.[3] In addition, mutations in *PADI6*, *NLRP5*, *OOEP*, and *KHDC3L* are
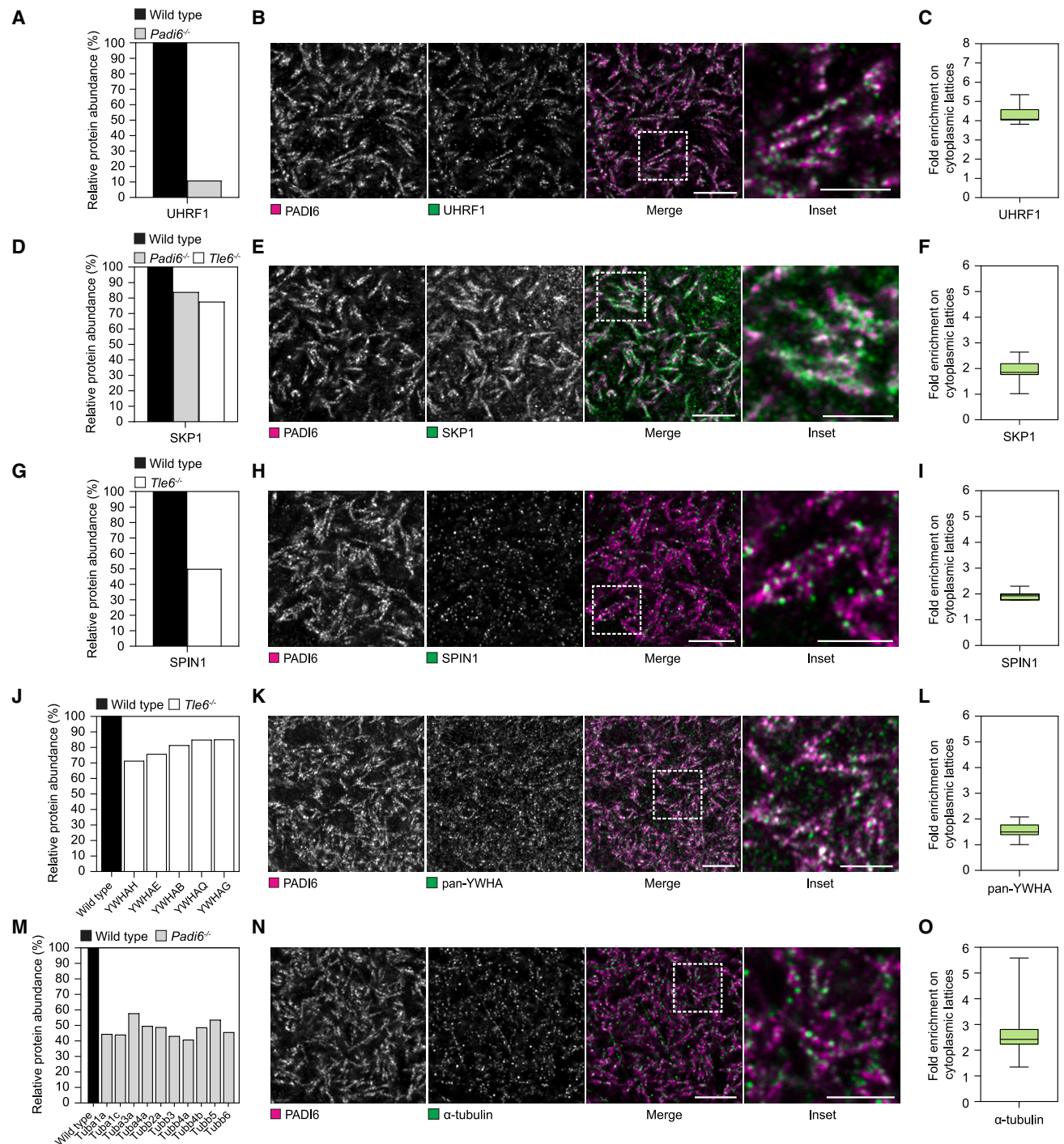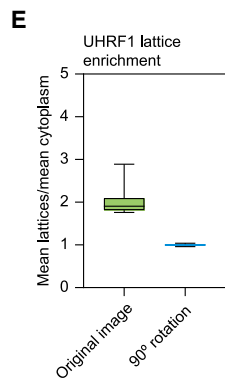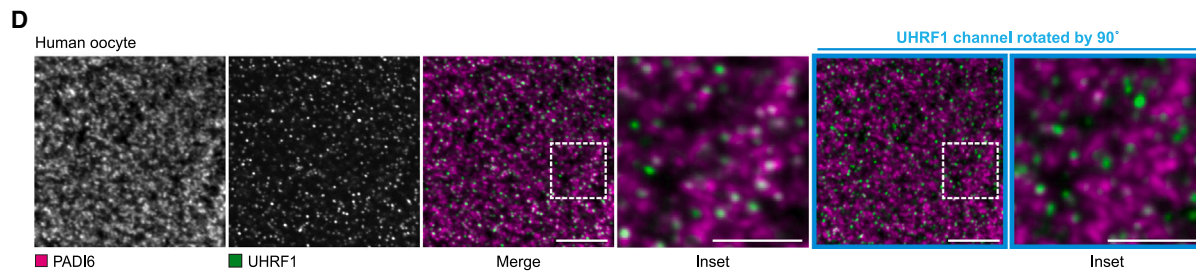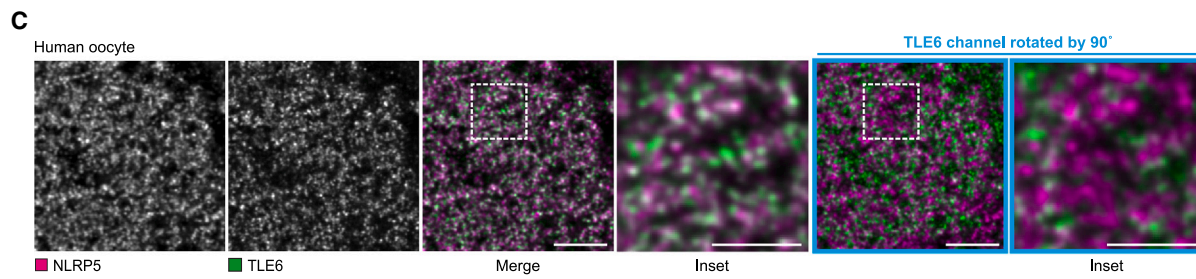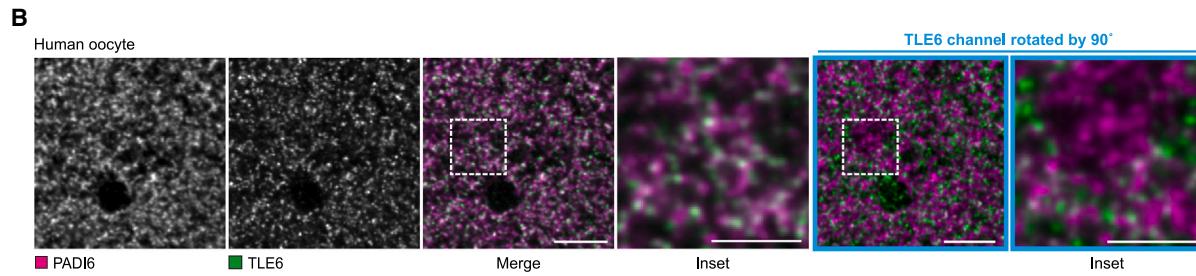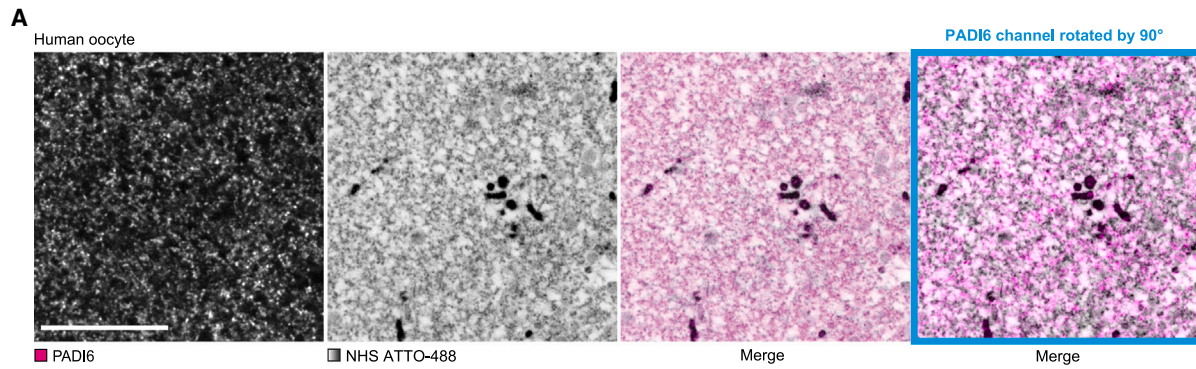
Figure 5. Essential oocyte proteins are stored on cytoplasmic lattices

(A, D, G, J, and M) Quantification of relative protein abundance of proteins shown in (B), (E), (H), (K), and (N), respectively; (J) includes all significantly changed YHWA/14-3-3 proteins, and (M) includes all significantly changed tubulin proteins.

(B, E, H, K, and N) Representative ExM micrographs of wild-type oocytes labeled for PADI6 (magenta) and UHRF1, SKP1, SPIN1, pan-YWHA/14-3-3, or α-tubulin (green), respectively. Insets are magnifications of outlined regions. Scale bars, 2 μm. Scale bars of insets, 1 μm. All scale bares are corrected for the expansion factor. All images were acquired using a laser scanning confocal microscope in Airyscan mode.

(C, F, I, L, and O) Quantification of candidate protein enrichment on cytoplasmic lattices. Fold enrichment was measured by dividing the candidate protein mean fluorescence intensity within a cytoplasmic lattice segmentation mask by the cytoplasmic signal outside. Vertical lines mark the mean. Whiskers represent minimum and maximum values.

See also Figures S6 and S7.

A Human oocyte

PADI6 channel rotated by 90°

PADI6 | NHS ATTO-488 | Merge | Merge

B Human oocyte

TLE6 channel rotated by 90°

PADI6 | TLE6 | Merge | Inset | | Inset

C Human oocyte

TLE6 channel rotated by 90°

NLRP5 | TLE6 | Merge | Inset | | Inset

D Human oocyte

UHRF1 channel rotated by 90°

PADI6 | UHRF1 | Merge | Inset | | Inset

E

UHRF1 lattice enrichment

Mean lattices/mean cytoplasm

Original image | 90° rotation

(legend on next page)

linked to recurrent biparental hydatidiform mole formation as well as births of offspring with multilocus imprinting disorders.[3,4,44] How the mutations result in these phenotypes is unclear. Given that UHRF1 (ubiquitin-like with PHD and RING finger domains 1), which is essential for the maintenance of DNA methylation in the early embryo,[71,75,76] was depleted in $Padi6^{-/-}$ mouse oocytes and was enriched on cytoplasmic lattices in wild-type mouse oocytes (Figures 5B and 5C), we examined whether UHRF1 is also stored on cytoplasmic lattices in human oocytes. To this end, we co-labeled expanded human oocytes to detect UHRF1 and the cytoplasmic lattice marker PADI6. Indeed, UHRF1 was enriched on cytoplasmic lattices in human oocytes (Figure 6D; Video S5). The 90° rotated image control did not show enrichment of UHRF1 on PADI6-positive structures (Figures 6D and 6E). Thus, cytoplasmic lattices of both mouse and human oocytes store UHRF1. We propose that reduced UHRF1 levels and/or altered UHRF1 localization contribute to the imprinting disorders that have been reported for embryos conceived by women with cytoplasmic-lattice-related gene mutations.[4,77,78]

DISCUSSION

This study shows that mammalian oocytes store proteins with essential functions for embryonic development on cytoplasmic lattices (Figure 7). After fertilization, the new embryo immediately requires a large number of proteins to initiate reprogramming and support development. By producing and stockpiling essential proteins during oocyte growth, the egg can meet these immediate needs of the early embryo.

Storing proteins specifically on the lattices results in their compartmentalization, which could serve multiple functions. Sequestering proteins on lattices in the cytoplasm could prevent their access to the nucleus. Indeed, cytoplasmic retention of UHRF1 is essential for the passive demethylation of the maternal genome following fertilization, and premature entry of UHRF1 into the oocyte nucleus causes genome hypermethylation.[75,79] Similarly, storing proteins on the lattices may prevent them from entering mitochondria or assembling into complexes such as ribosomes, which in turn might delay the functional activation of organelles and cellular machineries in the dividing embryo. Notably, the density of free ribosomes during preimplantation embryogenesis remains low during early embryogenesis until the morula stage, concomitant with cytoplasmic lattice disassembly.[80] In support of this, the ribosomal protein RSP6 is associated with a macromolecular complex in wild-type but not

$Padi6^{-/-}$ mouse oocytes.[27] Furthermore, storing proteins on the lattices may protect them from the degradation machinery or inactivate expression feedback loops. For example, the cellular concentration of tubulin is regulated by negative feedback loops in somatic cells.[81–83] Storing tubulin in a non-soluble form on cytoplasmic lattices would circumvent this negative feedback and allow a higher accumulation of tubulin in oocytes compared with somatic cells. Consistent with this notion, mouse oocytes contain ~3 times more α-tubulin than HeLa cells.[84] Our data hence also provide a possible explanation for the plethora of functions that have been suggested for the SCMC.[1,41]

In this study, we performed cryo-ET on oocytes, made possible by our deep-FIBing technique. Currently, the adaptation of cryo-ET technology to complex specimens such as large cells or tissues is an active area of research. Recent approaches have shown the great potential of FIB milling high-pressure frozen specimens.[85–87] In comparison, our deep-FIBing method is simpler, as it does not require high-pressure freezing or lift-out equipment. At the same time, deep-FIBing is limited to specimens that can be vitrified by plunge freezing. Of note, although deep-FIBing relies on the use of cryo-protectants, this is often also the case for vitrification of large specimens by high-pressure freezing. Our cryo-ET data reveal that the lattices have a high surface area, which is achieved by a well-spaced-out, regular distribution of filaments within a fiber. This organization appears to be ideal for storing proteins on individual filaments within a small volume. Our subtomogram-averaging structure likely represents the core of lattices. However, at the current resolution, it was not possible to further explore how lattice components are organized within the core. It is also conceivable that additional components bind the lattice core in a more heterogeneous fashion that cannot be resolved through averaging. Therefore, comprehensive structural and functional studies are needed to elucidate the molecular composition of lattices and how they store many proteins.

Several lattice proteins have the potential to mediate versatile interactions. For example, several of the SCMC proteins belong to the NLRP (nucleotide-binding oligomerization domain, leucine-rich repeat, and pyrin-domain-containing proteins) protein family. Leucine-rich repeats form a large globular protein domain that is present in a wide range of proteins with different cellular functions. The domain serves as a protein recognition motif and facilitates the formation of a large variety of protein-protein interactions.[88] Furthermore, our proteomic analyses identified several proteins, in addition to TLE6, which contain the WD40 domain. Like leucine-rich repeats, WD40 domains serve as protein-protein interaction platforms.[89] Finally, we found that the lattices are

Figure 6. Cytoplasmic lattices are composed of PADI6 and SCMC proteins and store UHRF1 in human oocytes

(A) Representative pan-ExM micrographs of wild-type human oocytes labeled for PADI6 (magenta) and NHS-ATTO488.

(B) Representative ExM micrographs of a GV human oocyte labeled for PADI6 (magenta) and TLE6 (green).

(C) Representative ExM micrographs of a GV human oocyte labeled for NLRP5 (magenta) and TLE6 (green).

(D) Representative ExM micrographs of a GV human oocyte labeled for PADI6 (magenta) and UHRF1 (green).

(E) Quantification of UHRF1 enrichment on human cytoplasmic lattices. Fold enrichment was measured by dividing the UHRF1 mean fluorescence intensity within a cytoplasmic lattice segmentation mask by the cytoplasmic signal outside. Cytoplasmic lattices were segmented in Ilastik. The same analysis was done for the 90°-rotated UHRF1 image. Vertical linkes mark the mean. Whiskers represent minimum and maximum values.

All insets are magnifications of respective outlined regions. In (A), scale bars, 5 μm. In (B)–(D), scale bars, 2 μm. Scale bars of insets, 1 μm. For (A)–(D); blue boxes indicate rotation of the PADI6, TLE6, or UHRF1 channels.

All micrographs were acquired on a laser scanning confocal microscope. All ExM scale bars have been corrected for the expansion factor.

See also Video S5.

CellPress
OPEN ACCESS
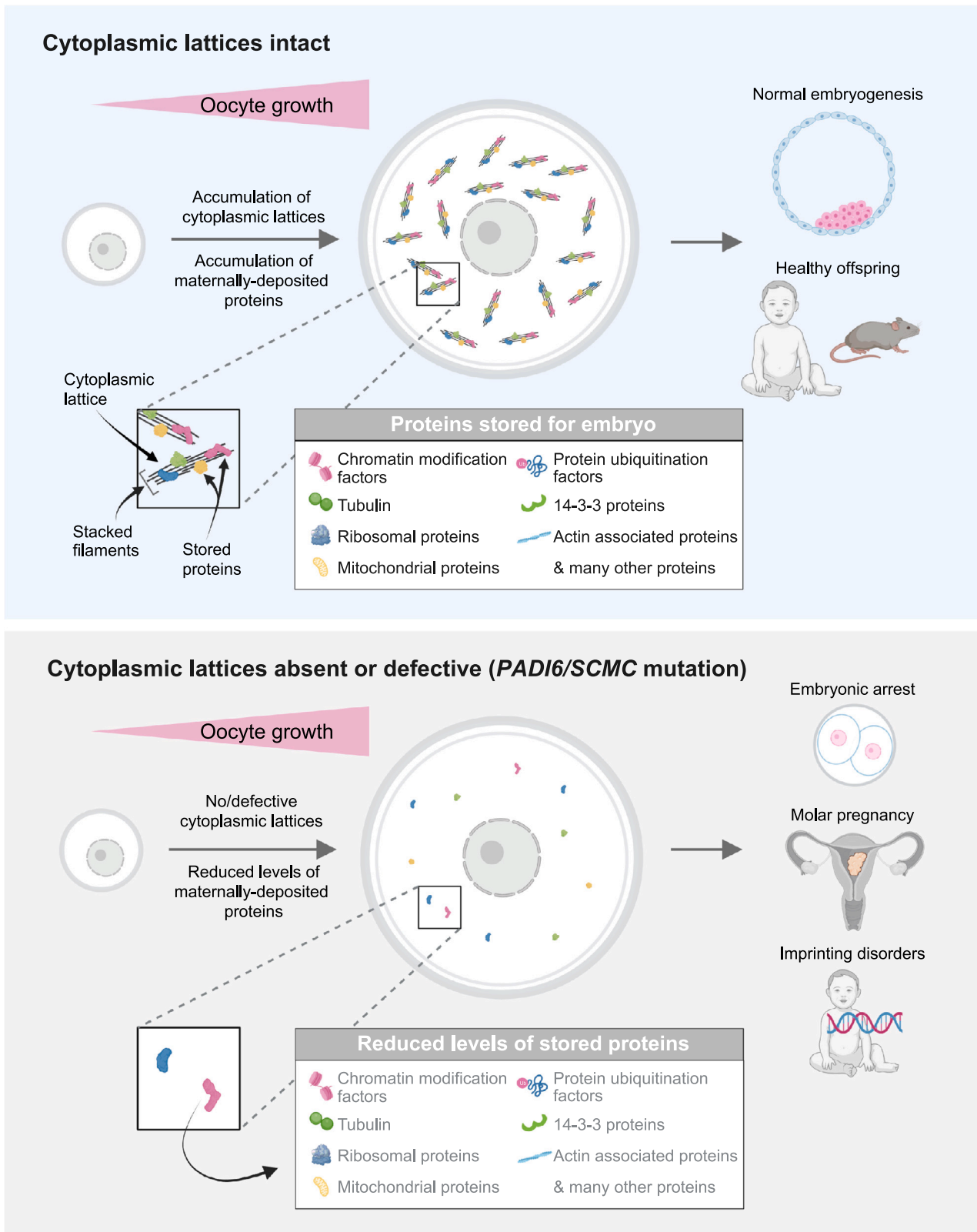
(legend on next page)

enriched in 14-3-3 domain proteins (Figures 4F, 4G, and 5J), which can interact with hundreds of different proteins.

PADI6 belongs to the small family of peptidylarginine deiminases. Peptidylarginine deiminases catalyze citrullination of peptidyl-arginine; however, the PADI6 isozyme is enzymatically inactive.[90,91] Peptidylarginine deiminases can bind to a wide range of substrates, but how they recognize substrates is unclear.[92] PADI6 might bind proteins by similar mechanisms as other peptidylarginine deiminases and thereby promote protein storage. In support of this hypothesis, 13 out of 40 proteins that were identified as substrates of PADI4 in an *in vitro* protein array assay were significantly depleted in the PADI6 mutant oocytes, including RPS2, RPS10, RPS13, RPS14, RPS15A, RPS18, RPL7, RPL18a, and PRMT1.[93]

Protein storage compartments in non-mammalian gametes, such as yolk in oviparous species or protein storage vacuoles in plant seeds, store proteins predominantly for nutrient purposes and later availability of amino acids.[5,8,94] Whether cytoplasmic lattices also serve a similar function in mammals in addition to storage of functional proteins will be another interesting topic for future studies.

Protein storage structures resembling cytoplasmic lattices have not yet been reported outside mammalian oocytes. However, the cytoplasmic-lattice-enriched protein α-tubulin[40] is also stored in oocytes from other species. For instance, early sea urchin embryos are dependent on maternally stockpiled tubulin for the first mitotic divisions following fertilization.[95] Oocytes from zebrafish, *Xenopus laevis*, *Rana pipiens*, *Drosophila*, and sea urchin store the majority of α-tubulin in non-polymerized pools, which have been proposed to be associated with a macromolecular structure of unknown nature.[96–100] In zebrafish, the size of the macromolecular structure and the amount of soluble α-tubulin decrease during early embryo development.[100] It is, however, unlikely that this macromolecular structure is directly related to cytoplasmic lattices, as SCMC proteins are not found in non-mammalian species.

Mutations in cytoplasmic-lattice-related genes are a well-established genetic cause of female infertility,[3] and *Padi6*/SCMC mutant mouse embryos cannot develop to term.[30–33,35,42] In addition, aberrant DNA methylation[101–104] and births of offspring with multilocus imprinting disorders[78,105–108] are seen in women with cytoplasmic-lattice-related gene mutations. The cytoplasmic lattices store proteins that are essential for epigenetic reprogramming, such as UHRF1 and KDM2B. Changes in the abundance and/or localization of these proteins caused by mutation in cytoplasmic-lattice-related genes are likely to contribute to these phenotypes. Individual mutations in *Padi6*/SCMC genes may affect the abundance and localization of the stored proteins as well as the structural integrity of the cytoplasmic lattices differently, which could explain why the severity of phenotypes varies between specific *PADI6* and SCMC mutations in women.

Given the importance of PADI6 and SCMC proteins for maintaining the levels of key maternally supplied proteins, it is not surprising that mutant embryos of both mice and humans fail to develop. Recognizing and identifying mutations in cytoplasmic lattice genes as the underlying cause of recurrent early pregnancy loss is important, as affected women will not benefit from *in vitro* fertilization or intracytoplasmic sperm injection. Thus, unnecessary emotional and financial burdens on infertile couples through unsuccessful cycles can be prevented. Importantly, we show that PADI6 and SCMC proteins are successfully incorporated into cytoplasmic lattices when expressed in mouse follicle culture. This suggests a potential treatment for women with cytoplasmic-lattice-related gene mutations in which follicles could be cultured *in vitro* to restore full protein functionality and proper cytoplasmic lattice assembly, which may allow embryo development to proceed normally.

Limitations of the study

Although our work provides intriguing insights into the organization and function of cytoplasmic lattices in mammalian oocytes, several issues remain to be addressed. We identify a large number of proteins that are depleted in Padi6$^{-/-}$ and Tle6$^{-/-}$ oocytes that lack cytoplasmic lattices, and we show for several of the depleted proteins that they associate with cytoplasmic lattices. However, we do not know whether all of the depleted proteins are stored on the lattices or whether some proteins are depleted by indirect effects. Conversely, it is possible that additional proteins are stored on cytoplasmic lattices that are not depleted in the mutants. Not all proteins may rely on cytoplasmic lattices in order to accumulate in oocytes and might contribute to the reduced developmental potential of the egg through mislocalization or premature activity. Furthermore, at present, we can only speculate how the cytoplasmic lattices associate with a wide range of stored proteins. Further biochemical and structural studies are needed to identify the protein-protein interaction mechanisms that allow for the enrichment of a wide variety of proteins on cytoplasmic lattices. Finally, PADI6 and the SCMC proteins are required for the accumulation of distinct subsets of proteins in oocytes. We speculate that they may be required to assemble distinct subunits of cytoplasmic lattices that are dependent on each other for complete assembly. Further studies are needed to determine whether such subunits exist and how they contribute to cytoplasmic lattice assembly and protein storage.

STAR★METHODS

Detailed methods are provided in the online version of this paper and include the following:

- KEY RESOURCES TABLE

Figure 7. Mammalian oocytes store proteins with essential functions for embryo development on cytoplasmic lattices
Model of cytoplasmic lattice function in mammalian oocytes. In normal oocytes (top), cytoplasmic lattices and maternally deposited proteins accumulate during oocyte growth. Cytoplasmic lattices are twisted fibers composed of individually stacked filaments. Proteins important to sustain embryonic development localize to cytoplasmic lattices, which supports accumulation and storage of these proteins. In oocytes with *PADI6*/SCMC gene mutations (bottom), cytoplasmic lattices do not form and the level of maternally provided proteins is reduced. *PADI6*/SCMC mutations thus impair early development and results in embryonic arrest, molar pregnancies, or offspring with multilocus imprinting disorders. Figure was created with BioRender.com.

Cell
Article

SUPPLEMENTAL INFORMATION

Supplemental information can be found online at https://doi.org/10.1016/j.cell.2023.10.003.

REFERENCES

1. Li, L., Zheng, P., and Dean, J. (2010). Maternal control of early mouse development. Development *137*, 859–870. https://doi.org/10.1242/dev.039487.

2. Zhang, K., and Smith, G.W. (2015). Maternal control of early embryogenesis in mammals. Reprod. Fertil. Dev. *27*, 880–896. https://doi.org/10.1071/RD14441.

3. Bebbere, D., Albertini, D.F., Coticchio, G., Borini, A., and Ledda, S. (2021). The subcortical maternal complex: emerging roles and novel perspectives. Mol. Hum. Reprod. *27*. https://doi.org/10.1093/MOLEHR/GAAB043.

4. Mitchell, L.E. (2022). Maternal effect genes: update and review of evidence for a link with birth defects. HGG Adv. *3*, 100067. https://doi.org/10.1016/j.xhgg.2021.100067.

5. Romano, M., Rosanova, P., Anteo, C., and Limatola, E. (2004). Vertebrate yolk proteins: a review. Mol. Reprod. Dev. *69*, 109–116. https://doi.org/10.1002/MRD.20146.

6. Perez, M.F., and Lehner, B. (2019). Vitellogenins - yolk gene function and regulation in Caenorhabditis elegans. Front. Physiol. *10*, 1067. https://doi.org/10.3389/fphys.2019.01067.

7. Herman, E.M., and Larkins, B.A. (1999). Protein storage bodies and vacuoles. Plant Cell *11*, 601–614. https://doi.org/10.1105/tpc.11.4.601.

8. Tan, X., Li, K., Wang, Z., Zhu, K., Tan, X., and Cao, J. (2019). A review of plant vacuoles: formation, located proteins, and functions. Plants (Basel) 8, 327. https://doi.org/10.3390/PLANTS8090327.

9. Wang, J., Li, Y., Lo, S.W., Hillmer, S., Sun, S.S.M., Robinson, D.G., and Jiang, L. (2007). Protein mobilization in germinating mung bean seeds involves vacuolar sorting receptors and multivesicular bodies. Plant Physiol. 143, 1628–1639. https://doi.org/10.1104/PP.107.096263.

10. Shewry, P.R., and Tosi, P. (2016). Protein synthesis and deposition. In Reference Module in Food Science (Elsevier). https://doi.org/10.1016/B978-0-08-100596-5.00106-2.

11. Prouteau, M., Desfosses, A., Sieben, C., Bourgoint, C., Mozaffari, N.L., Demurtas, D., Mitra, A.K., Guichard, P., Manley, S., and Loewith, R. (2017). TORC1 organized in inhibited domains (TOROIDs) regulate TORC1 activity. Nature 550, 265–269. https://doi.org/10.1038/nature24021.

12. Noree, C., Sato, B.K., Broyer, R.M., and Wilhelm, J.E. (2010). Identification of novel filament-forming proteins in Saccharomyces cerevisiae and Drosophila melanogaster. J. Cell Biol. 190, 541–551. https://doi.org/10.1083/JCB.201003001.

13. Shen, Q.J., Kassim, H., Huang, Y., Li, H., Zhang, J., Li, G., Wang, P.Y., Yan, J., Ye, F., and Liu, J.L. (2016). Filamentation of metabolic enzymes in Saccharomyces cerevisiae. J. Genet. Genomics 43, 393–404. https://doi.org/10.1016/J.JGG.2016.03.008.

14. Lynch, E.M., Hicks, D.R., Shepherd, M., Endrizzi, J.A., Maker, A., Hansen, J.M., Barry, R.M., Gitai, Z., Baldwin, E.P., and Kollman, J.M. (2017). Human CTP synthase filament structure reveals the active enzyme conformation. Nat. Struct. Mol. Biol. 24, 507–514. https://doi.org/10.1038/nsmb.3407.

15. Webb, B.A., Dosey, A.M., Wittmann, T., Kollman, J.M., and Barber, D.L. (2017). The glycolytic enzyme phosphofructokinase-1 assembles into filaments. J. Cell Biol. 216, 2305–2313. https://doi.org/10.1083/JCB.201701084.

16. Narayanaswamy, R., Levy, M., Tsechansky, M., Stovall, G.M., O'Connell, J.D., Mirrielees, J., Ellington, A.D., and Marcotte, E.M. (2009). Widespread reorganization of metabolic enzymes into reversible assemblies upon nutrient starvation. Proc. Natl. Acad. Sci. USA 106, 10147–10152. https://doi.org/10.1073/pnas.0812771106.

17. Suresh, H.G., da Silveira Dos Santos, A.X., Kukulski, W., Tyedmers, J., Riezman, H., Bukau, B., and Mogk, A. (2015). Prolonged starvation drives reversible sequestration of lipid biosynthetic enzymes and organelle reorganization in Saccharomyces cerevisiae. Mol. Biol. Cell 26, 1601–1615. https://doi.org/10.1091/mbc.E14-11-1559.

18. Petrovska, I., Nüske, E., Munder, M.C., Kulasegaran, G., Malinovska, L., Kroschwald, S., Richter, D., Fahmy, K., Gibson, K., Verbavatz, J.M., et al. (2014). Filament formation by metabolic enzymes is a specific adaptation to an advanced state of cellular starvation. eLife 3. https://doi.org/10.7554/eLife.02409.

19. Prouteau, M., and Loewith, R. (2018). Regulation of cellular metabolism through phase separation of enzymes. Biomolecules 8, 160. https://doi.org/10.3390/BIOM8040160.

20. Gallicano, G.I., McGaughey, R.W., and Capco, D.G. (1992). Cytoskeletal sheets appear as universal components of mammalian eggs. J. Exp. Zool. 263, 194–203. https://doi.org/10.1002/jez.1402630209.

21. Zamboni, L. (1970). Ultrastructure of mammalian oocytes and ova. Biol. Reprod. Suppl. 2, 44–63. https://doi.org/10.1095/biolreprod2.supplement_2.44.

22. Weakley, B.S. (1968). Comparison of cytoplasmic lamellae and membranous elements in the oocytes of five mammalian species. Z. Zellforsch. Mikrosk. Anat. 85, 109–123. https://doi.org/10.1007/BF00330591.

23. Hadek, R. (1966). Cytoplasmic whorls in the golden hamster oocyte. J. Cell Sci. 1, 281–282. https://doi.org/10.1242/jcs.1.3.281.

24. Burkholder, G.D., Comings, D.E., and Okada, T.A. (1971). A storage form of ribosomes in mouse oocytes. Exp. Cell Res. 69, 361–371. https://doi.org/10.1016/0014-4827(71)90236-9.

25. Sternlicht, A.L., and Schultz, R.M. (1981). Biochemical studies of mammalian oogenesis: kinetics of accumulation of total and poly(A)-containing RNA during growth of the mouse oocyte. J. Exp. Zool. 215, 191–200. https://doi.org/10.1002/JEZ.1402150209.

26. Bachvarova, R., de Leon, V., and Spiegelman, I. (1981). Mouse egg ribosomes: evidence for storage in lattices. J. Embryol. Exp. Morphol. 62, 153–164. https://doi.org/10.1242/dev.62.1.153.

27. Yurttas, P., Vitale, A.M., Fitzhenry, R.J., Cohen-Gould, L., Wu, W., Gossen, J.A., and Coonrod, S.A. (2008). Role for PADI6 and the cytoplasmic lattices in ribosomal storage in oocytes and translational control in the early mouse embryo. Development 135, 2627–2636. https://doi.org/10.1242/dev.016329.

28. Capco, D.G., Gallicano, G.I., McGaughey, R.W., Downing, K.H., and Larabell, C.A. (1993). Cytoskeletal sheets of mammalian eggs and embryos: A lattice-like network of intermediate filaments. Cell Motil. Cytoskeleton 24, 85–99. https://doi.org/10.1002/cm.970240202.

29. McGaughey, R.W., and Capco, D.G. (1989). Specialized cytoskeletal elements in mammalian eggs: structural and biochemical evidence for their composition. Cell Motil. Cytoskeleton 13, 104–111. https://doi.org/10.1002/CM.970130205.

30. Li, L., Baibakov, B., and Dean, J. (2008). A subcortical maternal complex essential for preimplantation mouse embryogenesis. Dev. Cell 15, 416–425. https://doi.org/10.1016/j.devcel.2008.07.010.

31. Gao, Z., Zhang, X., Yu, X., Qin, D., Xiao, Y., Yu, Y., Xiang, Y., Nie, X., Lu, X., Liu, W., et al. (2017). Zbed3 participates in the subcortical maternal complex and regulates the distribution of organelles. J. Mol. Cell Biol. 10, 74–88. https://doi.org/10.1093/jmcb/mjx035.

32. Qin, D., Gao, Z., Xiao, Y., Zhang, X., Ma, H., Yu, X., Nie, X., Fan, N., Wang, X., Ouyang, Y., et al. (2019). The subcortical maternal complex protein Nlrp4f is involved in cytoplasmic lattice formation and organelle distribution. Development 146, 183616. https://doi.org/10.1242/dev.183616.

33. Esposito, G., Vitale, A.M., Leijten, F.P.J., Strik, A.M., Koonen-Reemst, A.M.C.B., Yurttas, P., Robben, T.J.A.A., Coonrod, S., and Gossen, J.A. (2007). Peptidylarginine deiminase (PAD) 6 is essential for oocyte cytoskeletal sheet formation and female fertility. Mol. Cell. Endocrinol. 273, 25–31. https://doi.org/10.1016/J.MCE.2007.05.005.

34. Kim, B., Kan, R., Anguish, L., Nelson, L.M., and Coonrod, S.A. (2010). Potential role for MATER in cytoplasmic lattice formation in murine oocytes. PLoS One 5, e12587. https://doi.org/10.1371/journal.pone.0012587.

35. Tashiro, F., Kanai-Azuma, M., Miyazaki, S., Kato, M., Tanaka, T., Toyoda, S., Yamato, E., Kawakami, H., Miyazaki, T., and Miyazaki, J.-I. (2010). Maternal-effect gene Ces5/Ooep/Moep19/Floped is essential for oocyte cytoplasmic lattice formation and embryonic development at the maternal-zygotic stage transition. Genes Cells 15, 813–828. https://doi.org/10.1111/j.1365-2443.2010.01420.x.

36. Ohsugi, M., Zheng, P., Baibakov, B., Li, L., and Dean, J. (2008). Maternally derived FILIA-MATER complex localizes asymmetrically in cleavage-stage mouse embryos. Development 135, 259–269. https://doi.org/10.1242/dev.011445.

37. Schwarz, S.M., Gallicano, G.I., McGaughey, R.W., and Capco, D.G. (1995). A role for intermediate filaments in the establishment of the primitive epithelia during mammalian embryogenesis. Mech. Dev. 53, 305–321. https://doi.org/10.1016/0925-4773(95)00440-8.

38. Morency, E., Anguish, L., and Coonrod, S. (2011). Subcellular localization of cytoplasmic lattice-associated proteins is dependent upon fixation and processing procedures. PLoS One 6, e17226. https://doi.org/10.1371/journal.pone.0017226.

39. Wright, P.W., Bolling, L.C., Calvert, M.E., Sarmento, O.F., Berkeley, E.V., Shea, M.C., Hao, Z., Jayes, F.C., Bush, L.A., Shetty, J., et al. (2003). ePAD, an oocyte and early embryo-abundant peptidylarginine

Cell
Article

CellPress
OPEN ACCESS

deiminase-like protein that localizes to egg cytoplasmic sheets. Dev. Biol. *256*, 73–88. https://doi.org/10.1016/S0012-1606(02)00126-4.

40. Kan, R., Yurttas, P., Kim, B., Jin, M., Wo, L., Lee, B., Gosden, R., and Coonrod, S.A. (2011). Regulation of mouse oocyte microtubule and organelle dynamics by PADI6 and the cytoplasmic lattices. Dev. Biol. *350*, 311–322. https://doi.org/10.1016/j.ydbio.2010.11.033.

41. Lu, X., Gao, Z., Qin, D., and Li, L. (2017). A maternal functional module in the mammalian oocyte-to-embryo transition. Trends Mol. Med. *23*, 1014–1023. https://doi.org/10.1016/J.MOLMED.2017.09.004.

42. Tong, Z.B., Gold, L., Pfeifer, K.E., Dorward, H., Lee, E., Bondy, C.A., Dean, J., and Nelson, L.M. (2000). Mater, a maternal effect gene required for early embryonic development in mice. Nat. Genet. *26*, 267–268. https://doi.org/10.1038/81547.

43. Seckl, M.J., Sebire, N.J., and Berkowitz, R.S. (2010). Gestational trophoblastic disease. Lancet *376*, 717–729. https://doi.org/10.1016/S0140-6736(10)60280-2.

44. Monk, D., Sanchez-Delgado, M., and Fisher, R. (2017). NLRPs, the subcortical maternal complex and genomic imprinting. Reproduction *154*, R161–R170. https://doi.org/10.1530/REP-17-0465.

45. Kalogiannidis, I., Kalinderi, K., Kalinderis, M., Miliaras, D., Tarlatzis, B., and Athanasiadis, A. (2018). Recurrent complete hydatidiform mole: where we are, is there a safe gestational horizon? Opinion and mini-review. J. Assist. Reprod. Genet. *35*, 967–973. https://doi.org/10.1007/s10815-018-1202-9.

46. Sanchez-Delgado, M., Riccio, A., Eggermann, T., Maher, E.R., Lapunzina, P., Mackay, D., and Monk, D. (2016). Causes and consequences of multi-locus imprinting disturbances in humans. Trends Genet. *32*, 444–455. https://doi.org/10.1016/J.TIG.2016.05.001.

47. Herr, J.C., Chertihin, O., Digilio, L., Jha, K.N., Vemuganti, S., and Flickinger, C.J. (2008). Distribution of RNA binding protein MOEP19 in the oocyte cortex and early embryo indicates pre-patterning related to blastomere polarity and trophectoderm specification. Dev. Biol. *314*, 300–316. https://doi.org/10.1016/j.ydbio.2007.11.027.

48. Pfender, S., Kuznetsov, V., Pasternak, M., Tischer, T., Santhanam, B., and Schuh, M. (2015). Live imaging RNAi screen reveals genes essential for meiosis in mammalian oocytes. Nature *524*, 239–242. https://doi.org/10.1038/nature14568.

49. Tillberg, P.W., Chen, F., Piatkevich, K.D., Zhao, Y., Yu, C.C., English, B.P., Gao, L., Martorell, A., Suk, H.J., Yoshida, F., et al. (2016). Protein-retention expansion microscopy of cells and tissues labeled using standard fluorescent proteins and antibodies. Nat. Biotechnol. *34*, 987–992. https://doi.org/10.1038/NBT.3625.

50. Asano, S.M., Gao, R., Wassie, A.T., Tillberg, P.W., Chen, F., and Boyden, E.S. (2018). Expansion microscopy: protocols for imaging proteins and RNA in cells and tissues. Curr. Protoc. Cell Biol. *80*, e56. https://doi.org/10.1002/CPCB.56.

51. Gambarotto, D., Zwettler, F.U., Le Guennec, M., Schmidt-Cernohorska, M., Fortun, D., Borgers, S., Heine, J., Schloetel, J.G., Reuss, M., Unser, M., et al. (2019). Imaging cellular ultrastructures using expansion microscopy (U-ExM). Nat. Methods *16*, 71–74. https://doi.org/10.1038/s41592-018-0238-1.

52. Gao, M., Maraspini, R., Beutel, O., Zehtabian, A., Eickholt, B., Honigmann, A., and Ewers, H. (2018). Expansion stimulated emission depletion microscopy (ExSTED). ACS Nano *12*, 4178–4185. https://doi.org/10.1021/acsnano.8b00776.

53. Ian Gallicano, G., Larabell, C.A., McGaughey, R.W., and Capco, D.G. (1994). Novel cytoskeletal elements in mammalian eggs are composed of a unique arrangement of intermediate filaments. Mech. Dev. *45*, 211–226. https://doi.org/10.1016/0925-4773(94)90009-4.

54. Chen, F., Tillberg, P.W., and Boyden, E.S. (2015). Optical imaging. Expansion microscopy. Science *347*, 543–548. https://doi.org/10.1126/science.1260088.

55. M'Saad, O., and Bewersdorf, J. (2020). Light microscopy of proteins in their ultrastructural context. Nat. Commun. *11*, 3850. https://doi.org/10.1038/s41467-020-17523-8.

56. Bäuerlein, F.J.B., Renner, M., El Chami, D., Lehnart, S.E., Pastor-Pareja, J.C., and Fernández-Busnadiego, R. (2023). Cryo-electron tomography of large biological specimens vitrified by plunge freezing. Preprint at bioRxiv. https://doi.org/10.1101/2021.04.14.437159.

57. Bhattacharya, S. (2018). Cryoprotectants and their usage in cryopreservation process. In Cryopreservation Biotechnology in Biomedical and Biological Sciences, Y. Bozkurt, ed. (IntechOpen). https://doi.org/10.5772/intechopen.80477.

58. Kasapi, E., Asimakopoulos, B., Chatzimeletiou, K., Petousis, S., Panagiotidis, Y., Prapas, N., and Nikolettos, N. (2017). Vitrification of human germinal vesicle oocytes: before or after in vitro maturation? Int. J. Fertil. Steril. *11*, 85–92. https://doi.org/10.22074/IJFS.2017.4717.

59. Palmerini, M.G., Antinori, M., Maione, M., Cerusico, F., Versaci, C., Nottola, S.A., Macchiarelli, G., Khalili, M.A., and Antinori, S. (2014). Ultrastructure of immature and mature human oocytes after cryotop vitrification. J. Reprod. Dev. *60*, 411–420. https://doi.org/10.1262/JRD.2014-027.

60. Selman, H., Angelini, A., Barnocchi, N., Brusco, G.F., Pacchiarotti, A., and Aragona, C. (2006). Ongoing pregnancies after vitrification of human oocytes using a combined solution of ethylene glycol and dimethyl sulfoxide. Fertil. Steril. *86*, 997–1000. https://doi.org/10.1016/J.FERTNSTERT.2006.02.117.

61. Molina, I., Gómez, J., Balasch, S., Pellicer, N., and Novella-Maestre, E. (2016). Osmotic-shock produced by vitrification solutions improves immature human oocytes in vitro maturation. Reprod. Biol. Endocrinol. *14*, 27. https://doi.org/10.1186/S12958-016-0161-1.

62. Trinkaus, V.A., Riera-Tur, I., Martínez-Sánchez, A., Bäuerlein, F.J.B., Guo, Q., Arzberger, T., Baumeister, W., Dudanova, I., Hipp, M.S., Hartl, F.U., et al. (2021). In situ architecture of neuronal α-Synuclein inclusions. Nat. Commun. *12*, 2110. https://doi.org/10.1038/s41467-021-22108-0.

63. Bäuerlein, F.J.B., Saha, I., Mishra, A., Kalemanov, M., Martínez-Sánchez, A., Klein, R., Dudanova, I., Hipp, M.S., Hartl, F.U., Baumeister, W., et al. (2017). In situ architecture and cellular interactions of PolyQ inclusions. Cell *171*, 179–187.e10. https://doi.org/10.1016/j.cell.2017.08.009.

64. Chakraborty, S., Mahamid, J., and Baumeister, W. (2020). Cryoelectron tomography reveals nanoscale organization of the cytoskeleton and its relation to microtubule curvature inside cells. Structure *28*, 991–1003.e4. https://doi.org/10.1016/J.STR.2020.05.013.

65. Yurttas, P., Morency, E., and Coonrod, S.A. (2010). Use of proteomics to identify highly abundant maternal factors that drive the egg-to-embryo transition. Reproduction *139*, 809–823. https://doi.org/10.1530/REP-09-0538.

66. Park, S.J., Shirahige, K., Ohsugi, M., and Nakai, K. (2015). DBTMEE: a database of transcriptome in mouse early embryos. Nucleic Acids Res. *43*, D771–D776. https://doi.org/10.1093/nar/gku1001.

67. Yu, X.J., Yi, Z., Gao, Z., Qin, D., Zhai, Y., Chen, X., Ou-Yang, Y., Wang, Z.B., Zheng, P., Zhu, M.S., et al. (2014). The subcortical maternal complex controls symmetric division of mouse zygotes by regulating F-actin dynamics. Nat. Commun. *5*, 4887.

68. Szklarczyk, D., Gable, A.L., Nastou, K.C., Lyon, D., Kirsch, R., Pyysalo, S., Doncheva, N.T., Legeay, M., Fang, T., Bork, P., et al. (2021). The STRING database in 2021: customizable protein-protein networks, and functional characterization of user-uploaded gene/measurement sets. Nucleic Acids Res. *49*, D605–D612. https://doi.org/10.1093/NAR/GKAA1074.

69. Johnson, C., Crowther, S., Stafford, M.J., Campbell, D.G., Toth, R., and MacKintosh, C. (2010). Bioinformatic and experimental survey of 14–3-3-binding sites. Biochem. J. *427*, 69–78. https://doi.org/10.1042/BJ20091834.

70. Pennington, K.L., Chan, T.Y., Torres, M.P., and Andersen, J.L. (2018). The dynamic and stress-adaptive signaling hub of 14-3-3: emerging mechanisms of regulation and context-dependent protein–protein interactions. Oncogene *37*, 5587–5604. https://doi.org/10.1038/s41388-018-0348-3.

71. Maenohara, S., Unoki, M., Toh, H., Ohishi, H., Sharif, J., Koseki, H., and Sasaki, H. (2017). Role of UHRF1 in de novo DNA methylation in oocytes and maintenance methylation in preimplantation embryos. PLoS Genet. *13*, e1007042. https://doi.org/10.1371/JOURNAL.PGEN.1007042.

72. Kinterova, V., Kanka, J., Petruskova, V., and Toralova, T. (2019). Inhibition of Skp1-Cullin-F-box complexes during bovine oocyte maturation and preimplantation development leads to delayed development of embryos†. Biol. Reprod. *100*, 896–906. https://doi.org/10.1093/biolre/ioy254.

73. Posfai, E., Kunzmann, R., Brochard, V., Salvaing, J., Cabuy, E., Roloff, T.C., Liu, Z., Tardat, M., van Lohuizen, M., Vidal, M., et al. (2012). Polycomb function during oogenesis is required for mouse embryonic development. Genes Dev. *26*, 920–932. https://doi.org/10.1101/gad.188094.112.

74. Boulard, M., Edwards, J.R., and Bestor, T.H. (2015). FBXL10 protects Polycomb-bound genes from hypermethylation. Nat. Genet. *47*, 479–485. https://doi.org/10.1038/ng.3272.

75. Li, Y., Zhang, Z., Chen, J., Liu, W., Lai, W., Liu, B., Li, X., Liu, L., Xu, S., Dong, Q., et al. (2018). Stella safeguards the oocyte methylome by preventing de novo methylation mediated by DNMT1. Nature *564*, 136–140. https://doi.org/10.1038/s41586-018-0751-5.

76. Wu, Y., Dong, J., Feng, S., Zhao, Q., Duan, P., Xiong, M., Wen, Y., Lv, C., Wang, X., and Yuan, S. (2021). Maternal UHRF1 is essential for transcription landscapes and repression of repetitive elements during the maternal-to-zygotic transition. Front. Cell Dev. Biol. *8*, 610773. https://doi.org/10.3389/fcell.2020.610773.

77. Elbracht, M., Mackay, D., Begemann, M., Kagan, K.O., and Eggermann, T. (2020). Disturbed genomic imprinting and its relevance for human reproduction: causes and clinical consequences. Hum. Reprod. Update *26*, 197–213. https://doi.org/10.1093/HUMUPD/DMZ045.

78. Begemann, M., Rezwan, F.I., Beygo, J., Docherty, L.E., Kolarova, J., Schroeder, C., Buiting, K., Chokkalingam, K., Degenhardt, F., Wakeling, E.L., et al. (2018). Maternal variants in NLRP and other maternal effect proteins are associated with multilocus imprinting disturbance in offspring. J. Med. Genet. *55*, 497–504. https://doi.org/10.1136/JMEDG-ENET-2017-105190.

79. Eckersley-Maslin, M.A., Alda-Catalinas, C., and Reik, W. (2018). Dynamics of the epigenetic landscape during the maternal-to-zygotic transition. Nat. Rev. Mol. Cell Biol. *19*, 436–450. https://doi.org/10.1038/s41580-018-0008-z.

80. Israel, S., Ernst, M., Psathaki, O.E., Drexler, H.C.A., Casser, E., Suzuki, Y., Makalowski, W., Boiani, M., Fuellen, G., and Taher, L. (2019). An integrated genome-wide multi-omics analysis of gene expression dynamics in the preimplantation mouse embryo. Sci. Rep. *9*, 13356. https://doi.org/10.1038/s41598-019-49817-3.

81. Gasic, I., Boswell, S.A., and Mitchison, T.J. (2019). Tubulin mRNA stability is sensitive to change in microtubule dynamics caused by multiple physiological and toxic cues. PLoS Biol. *17*, e3000225. https://doi.org/10.1371/JOURNAL.PBIO.3000225.

82. Jonasson, E.M., Mauro, A.J., Li, C., Labuz, E.C., Mahserejian, S.M., Scripture, J.P., Gregoretti, I.V., Alber, M., and Goodson, H.V. (2020). Behaviors of individual microtubules and microtubule populations relative to critical concentrations: dynamic instability occurs when critical concentrations are driven apart by nucleotide hydrolysis. Mol. Biol. Cell *31*, 589–618. https://doi.org/10.1091/mbc.E19-02-0101.

83. Lin, Z., Gasic, I., Chandrasekaran, V., Peters, N., Shao, S., Mitchison, T.J., and Hegde, R.S. (2020). TTC5 mediates autoregulation of tubulin via mRNA degradation. Science *367*, 100–104. https://doi.org/10.1126/science.aaz4352.

84. So, C., Menelaou, K., Uraji, J., Harasimov, K., Steyer, A.M., Seres, K.B., Bucevičius, J., Lukinavičius, G., Möbius, W., Sibold, C., et al. (2022). Mechanism of spindle pole organization and instability in human oocytes. Science *375* (1979), eabj3944. https://doi.org/10.1126/science.abj3944.

85. Schiøtz, O.H., Kaiser, C.J.O., Klumpe, S., Morado, D.R., Poege, M., Schneider, J., Beck, F., Thompson, C., and Plitzko, M.J. (2023). Serial lift-out – sampling the molecular anatomy of whole organisms. Preprint at bioRxiv. https://doi.org/10.1101/2023.04.28.538734.

86. Schaffer, M., Pfeffer, S., Mahamid, J., Kleindiek, S., Laugks, T., Albert, S., Engel, B.D., Rummel, A., Smith, A.J., Baumeister, W., et al. (2019). A cryo-FIB lift-out technique enables molecular-resolution cryo-ET within native Caenorhabditis elegans tissue. Nat. Methods *16*, 757–762. https://doi.org/10.1038/s41592-019-0497-5.

87. Kelley, K., Raczkowski, A.M., Klykov, O., Jaroenlak, P., Bobe, D., Kopylov, M., Eng, E.T., Bhabha, G., Potter, C.S., Carragher, B., et al. (2022). Waffle method: a general and flexible approach for improving throughput in FIB-milling. Nat. Commun. *13*, 1857. https://doi.org/10.1038/s41467-022-29501-3.

88. Kobe, B., and v Kajava, A.V. (2001). The leucine-rich repeat as a protein recognition motif. Curr. Opin. Struct. Biol. *11*, 725–732. https://doi.org/10.1016/S0959-440X(01)00266-4.

89. Xu, C., and Min, J. (2011). Structure and function of WD40 domain proteins. Protein Cell *2*, 202–214. https://doi.org/10.1007/S13238-011-1018-1.

90. Raijmakers, R., Zendman, A.J.W., Egberts, W.V., Vossenaar, E.R., Raats, J., Soede-Huijbregts, C., Rutjes, F.P.J.T., van Veelen, P.A., Drijfhout, J.W., and Pruijn, G.J.M. (2007). Methylation of arginine residues interferes with citrullination by peptidylarginine deiminases in vitro. J. Mol. Biol. *367*, 1118–1129. https://doi.org/10.1016/J.JMB.2007.01.054.

91. Taki, H., Gomi, T., Knuckley, B., Thompson, P.R., Vugrek, O., Hirata, K., Miyahara, T., Shinoda, K., Hounoki, H., Sugiyama, E., et al. (2011). Purification of enzymatically inactive peptidylarginine deiminase type 6 from mouse ovary that reveals hexameric structure different from other dimeric isoforms. Adv. Biosci. Biotechnol. *02*, 304–310. https://doi.org/10.4236/ABB.2011.24044.

92. Witalison, E.E., Thompson, P.R., and Hofseth, L.J. (2015). Protein arginine deiminases and associated citrullination: physiological functions and diseases associated with dysregulation. Curr. Drug Targets *16*, 700–710. https://doi.org/10.2174/1389450116666150202160954.

93. Guo, Q., Bedford, M.T., and Fast, W. (2011). Discovery of peptidylarginine deiminase-4 substrates by protein array: antagonistic citrullination and methylation of human ribosomal protein S2. Mol. Biosyst. *7*, 2286–2295. https://doi.org/10.1039/C1MB05089C.

94. Antonets, K.S., Belousov, M.V., Sulatskaya, A.I., Belousova, M.E., Kosolapova, A.O., Sulatsky, M.I., Andreeva, E.A., Zykin, P.A., Malovichko, Y.V., Shtark, O.Y., et al. (2020). Accumulation of storage proteins in plant seeds is mediated by amyloid formation. PLoS Biol. *18*, e3000564. https://doi.org/10.1371/JOURNAL.PBIO.3000564.

95. Bibring, T., and Baxandall, J. (1977). Tubulin synthesis in sea urchin embryos: almost all tubulin of the first cleavage mitotic apparatus derives from the unfertilized egg. Dev. Biol. *55*, 191–195. https://doi.org/10.1016/0012-1606(77)90330-X.

96. Raff, R.A., and Kaumeyer, J.F. (1973). Soluble microtubule proteins of the sea urchin embryo: partial characterization of the proteins and behavior of the pool in early development. Dev. Biol. *32*, 309–320. https://doi.org/10.1016/0012-1606(73)90243-1.

97. Pestell, R.Q.W. (1975). Microtubule protein synthesis during oogenesis and early embryogenesis in Xenopus laevis. Biochem. J. *145*, 527–534. https://doi.org/10.1042/BJ1450527.

98. Wang, T., and Lessman, C.A. (1997). The major soluble tubulins are found in mega dalton (MDa) fractions in fully-grown oocytes and eggs but not in brain of the frog, Rana pipiens. Comp. Biochem. Physiol. B Biochem. Mol. Biol. *118*, 421–430. https://doi.org/10.1016/S0305-0491(97)00108-9.

Cell
Article

CellPress
OPEN ACCESS

99. Lessman, C.A., and Kim, H. (2001). Soluble tubulin complexes in oocytes of the common leopard frog, Rana pipiens, contain gamma-tubulin. Mol. Reprod. Dev. 60, 128–136. https://doi.org/10.1002/MRD.1069.

100. Liu, J., and Lessman, C.A. (2007). Soluble tubulin complexes, γ-tubulin, and their changing distribution in the zebrafish (Danio rerio) ovary, oocyte and embryo. Comp. Biochem. Physiol. B Biochem. Mol. Biol. 147, 56–73. https://doi.org/10.1016/J.CBPB.2006.12.014.

101. Qian, J., Nguyen, N.M.P., Rezaei, M., Huang, B., Tao, Y., Zhang, X., Cheng, Q., Yang, H., Asangla, A., Majewski, J., et al. (2018). Biallelic PADI6 variants linking infertility, miscarriages, and hydatidiform moles. Eur. J. Hum. Genet. 26, 1007–1013. https://doi.org/10.1038/s41431-018-0141-3.

102. Murdoch, S., Djuric, U., Mazhar, B., Seoud, M., Khan, R., Kuick, R., Bagga, R., Kircheisen, R., Ao, A., Ratti, B., et al. (2006). Mutations in NALP7 cause recurrent hydatidiform moles and reproductive wastage in humans. Nat. Genet. 38, 300–302. https://doi.org/10.1038/ng1740.

103. Demond, H., Anvar, Z., Jahromi, B.N., Sparago, A., Verma, A., Davari, M., Calzari, L., Russo, S., Jahromi, M.A., Monk, D., et al. (2019). A KHDC3L mutation resulting in recurrent hydatidiform mole causes genome-wide DNA methylation loss in oocytes and persistent imprinting defects post-fertilisation. Genome Med. 11, 84. https://doi.org/10.1186/s13073-019-0694-y.

104. Zhang, W., Chen, Z., Zhang, D., Zhao, B., Liu, L., Xie, Z., Yao, Y., and Zheng, P. (2019). KHDC3L mutation causes recurrent pregnancy loss by inducing genomic instability of human early embryonic cells. PLoS Biol. 17, e3000468. https://doi.org/10.1371/journal.pbio.3000468.

105. Docherty, L.E., Rezwan, F.I., Poole, R.L., Turner, C.L.S., Kivuva, E., Maher, E.R., Smithson, S.F., Hamilton-Shield, J.P., Patalan, M., Gizewska, M., et al. (2015). Mutations in NLRP5 are associated with reproductive wastage and multilocus imprinting disorders in humans. Nat. Commun. 6, 8086. https://doi.org/10.1038/ncomms9086.

106. Cubellis, M.V., Pignata, L., Verma, A., Sparago, A., del Prete, R., Monticelli, M., Calzari, L., Antona, V., Melis, D., Tenconi, R., et al. (2020). Loss-of-function maternal-effect mutations of PADI6 are associated with familial and sporadic Beckwith-Wiedemann syndrome with multi-locus imprinting disturbance. Clin. Epigenetics 12, 139. https://doi.org/10.1186/s13148-020-00925-2.

107. Tannorella, P., Calzari, L., Daolio, C., Mainini, E., Vimercati, A., Gentilini, D., Soli, F., Pedrolli, A., Bonati, M.T., Larizza, L., et al. (2022). Germline variants in genes of the subcortical maternal complex and multilocus imprinting disturbance are associated with miscarriage/infertility or Beckwith–Wiedemann progeny. Clin. Epigenetics 14, 43. https://doi.org/10.1186/S13148-022-01262-2.

108. Zheng, W., Hu, H., Dai, J., Zhang, S., Gu, Y., Dai, C., Guo, J., Xu, X., Li, Y., Zhang, S., et al. (2021). Expanding the genetic and phenotypic spectrum of the subcortical maternal complex genes in recurrent preimplantation embryonic arrest. Clin. Genet. 99, 286–291. https://doi.org/10.1111/CGE.13858.

109. Schindelin, J., Arganda-Carreras, I., Frise, E., Kaynig, V., Longair, M., Pietzsch, T., Preibisch, S., Rueden, C., Saalfeld, S., Schmid, B., et al. (2012). Fiji: an open-source platform for biological-image analysis. Nat. Methods 9, 676–682. https://doi.org/10.1038/nmeth.2019.

110. Berg, S., Kutra, D., Kroeger, T., Straehle, C.N., Kausler, B.X., Haubold, C., Schiegg, M., Ales, J., Beier, T., Rudy, M., et al. (2019). ilastik: interactive machine learning for (bio)image analysis. Nat. Methods 16, 1226–1232. https://doi.org/10.1038/s41592-019-0582-9.

111. Klein, S., Staring, M., Murphy, K., Viergever, M.A., and Pluim, J.P.W. (2010). Elastix: a toolbox for intensity-based medical image registration. IEEE Trans. Med. Imaging 29, 196–205. https://doi.org/10.1109/TMI.2009.2035616.

112. McCormick, M., van der Valk, V., Zukić, D., Dekker, N., and Wu, H.-Y. (2021). InsightSoftwareConsortium/ITKElastix: ITKElastix 0.11.0. Zenodo.. https://doi.org/10.5281/ZENODO.4556389.

113. R Core Team (2021). R: A Language and Environment for Statistical Computing (R Foundation for Statistical Computing). https://www.R-project.org/.

114. Mastronarde, D.N. (2005). Automated electron microscope tomography using robust prediction of specimen movements. J. Struct. Biol. 152, 36–51. https://doi.org/10.1016/J.JSB.2005.07.007.

115. Kremer, J.R., Mastronarde, D.N., and McIntosh, J.R. (1996). Computer visualization of three-dimensional image data using IMOD. J. Struct. Biol. 116, 71–76. https://doi.org/10.1006/JSBI.1996.0013.

116. Bruderer, R., Bernhardt, O.M., Gandhi, T., Miladinović, S.M., Cheng, L.Y., Messner, S., Ehrenberger, T., Zanotelli, V., Butscheid, Y., Escher, C., et al. (2015). Extending the limits of quantitative proteome profiling with data-independent acquisition and application to acetaminophen-treated three-dimensional liver microtissues. Mol. Cell. Proteomics 14, 1400–1410. https://doi.org/10.1074/mcp.M114.044305.

117. Perez-Riverol, Y., Bai, J., Bandla, C., García-Seisdedos, D., Hewapathirana, S., Kamatchinathan, S., Kundu, D.J., Prakash, A., Frericks-Zipper, A., Eisenacher, M., et al. (2022). The PRIDE database resources in 2022: a hub for mass spectrometry-based proteomics evidences. Nucleic Acids Res. 50, D543–D552. https://doi.org/10.1093/NAR/GKAB1038.

118. Edgar, R., Domrachev, M., and Lash, A.E. (2002). Gene Expression Omnibus: NCBI gene expression and hybridization array data repository. Nucleic Acids Res. 30, 207–210. https://doi.org/10.1093/NAR/30.1.207.

119. Shen, B., Zhang, J., Wu, H., Wang, J., Ma, K., Li, Z., Zhang, X., Zhang, P., and Huang, X. (2013). Generation of gene-modified mice via Cas9/RNA-mediated gene targeting. Cell Res. 23, 720–723. https://doi.org/10.1038/cr.2013.46.

120. Scheffler, K., Uraji, J., Jentoft, I., Cavazza, T., Mönnich, E., Mogessie, B., and Schuh, M. (2021). Two mechanisms drive pronuclear migration in mouse zygotes. Nat. Commun. 12, 841. https://doi.org/10.1038/s41467-021-21020-x.

121. Schuh, M., and Ellenberg, J. (2007). Self-organization of MTOCs replaces centrosome function during acentrosomal spindle assembly in live mouse oocytes. Cell 130, 484–498. https://doi.org/10.1016/j.cell.2007.06.025.

122. Jaffe, L.A., and Terasaki, M. (2004). Quantitative microinjection of oocytes, eggs, and embryos. Methods Cell Biol. 74, 219–242. https://doi.org/10.1016/S0091-679X(04)74010-8.

123. Los, G.V., Encell, L.P., McDougall, M.G., Hartzell, D.D., Karassina, N., Zimprich, C., Wood, M.G., Learish, R., Ohana, R.F., Urh, M., et al. (2008). HaloTag: A novel protein labeling technology for cell imaging and protein analysis. ACS Chem. Biol. 3, 373–382. https://doi.org/10.1021/cb800025k.

124. Shamonin, D.P., Bron, E.E., Lelieveldt, B.P.F., Smits, M., Klein, S., and Staring, M.; Alzheimer's Disease Neuroimaging Initiative (2014). Fast parallel image registration on CPU and GPU for diagnostic classification of Alzheimer's disease. Front. Neuroinform. 7, 50. https://doi.org/10.3389/fninf.2013.00050.

125. Rigort, A., Günther, D., Hegerl, R., Baum, D., Weber, B., Prohaska, S., Medalia, O., Baumeister, W., and Hege, H.C. (2012). Automated segmentation of electron tomograms for a quantitative description of actin filament networks. J. Struct. Biol. 177, 135–144. https://doi.org/10.1016/J.JSB.2011.08.012.

126. Jasnin, M., Asano, S., Gouin, E., Hegerl, R., Plitzko, J.M., Villa, E., Cossart, P., and Baumeister, W. (2013). Three-dimensional architecture of actin filaments in Listeria monocytogenes comet tails. Proc. Natl. Acad. Sci. USA 110, 20521–20526. https://doi.org/10.1073/pnas.1320155110.

127. Lowe, D.G. (2004). Distinctive image features from scale-invariant keypoints. Int. J. Comput. Vis. 60, 91–110. https://doi.org/10.1023/B:VISI.0000029664.99615.94.

128. Fernandez, J.J., Laugks, U., Schaffer, M., Bäuerlein, F.J.B., Khoshouei, M., Baumeister, W., and Lucic, V. (2016). Removing contamination-

induced reconstruction artifacts from cryo-electron tomograms. Biophys. J. *110*, 850–859. https://doi.org/10.1016/J.BPJ.2015.10.043.

129. Liu, Y.T., Zhang, H., Wang, H., Tao, C.L., Bi, G.Q., and Zhou, Z.H. (2022). Isotropic reconstruction for electron tomography with deep learning. Nat. Commun. *13*, 6482. https://doi.org/10.1038/s41467-022-33957-8.

130. Rohou, A., and Grigorieff, N. (2015). CTFFIND4: fast and accurate defocus estimation from electron micrographs. J. Struct. Biol. *192*, 216–221. https://doi.org/10.1016/J.JSB.2015.08.008.

131. Castaño-Díez, D., Kudryashev, M., Arheit, M., and Stahlberg, H. (2012). Dynamo: a flexible, user-friendly development tool for subtomogram averaging of cryo-EM data in high-performance computing environments. J. Struct. Biol. *178*, 139–151. https://doi.org/10.1016/J.JSB.2011.12.017.

132. Scheres, S.H.W. (2012). RELION: implementation of a Bayesian approach to cryo-EM structure determination. J. Struct. Biol. *180*, 519–530. https://doi.org/10.1016/J.JSB.2012.09.006.

133. Pettersen, E.F., Goddard, T.D., Huang, C.C., Couch, G.S., Greenblatt, D.M., Meng, E.C., and Ferrin, T.E. (2004). UCSF Chimera–a visualization system for exploratory research and analysis. J. Comput. Chem. *25*, 1605–1612. https://doi.org/10.1002/JCC.20084.

134. Hughes, C.S., Moggridge, S., Müller, T., Sorensen, P.H., Morin, G.B., and Krijgsveld, J. (2018). Single-pot, solid-phase-enhanced sample preparation for proteomics experiments. Nat. Protoc. *14*, 68–85. https://doi.org/10.1038/s41596-018-0082-x.

135. Cheng, S., Altmeppen, G., So, C., Welp, L.M., Penir, S., Ruhwedel, T., Menelaou, K., Harasimov, K., Stützer, A., Blayney, M., et al. (2022). Mammalian oocytes store mRNAs in a mitochondria-associated membraneless compartment. Science *378*, eabq4835. https://doi.org/10.1126/science.abq4835.

136. Storey, J.D. (2002). A direct approach to false discovery rates. J. R. Stat. Soc. B *64*, 479–498. https://doi.org/10.1111/1467-9868.00346.

137. Martin, M. (2011). Cutadapt removes adapter sequences from high-throughput sequencing reads. EMBnet J. *17*, 10–12. https://doi.org/10.14806/EJ.17.1.200.

138. Dobin, A., Davis, C.A., Schlesinger, F., Drenkow, J., Zaleski, C., Jha, S., Batut, P., Chaisson, M., and Gingeras, T.R. (2013). STAR: ultrafast universal RNA-seq aligner. Bioinformatics *29*, 15–21. https://doi.org/10.1093/BIOINFORMATICS/BTS635.

139. Anders, S., Pyl, P.T., and Huber, W. (2015). HTSeq—a Python framework to work with high-throughput sequencing data. Bioinformatics *31*, 166–169. https://doi.org/10.1093/BIOINFORMATICS/BTU638.

140. Love, M.I., Huber, W., and Anders, S. (2014). Moderated estimation of fold change and dispersion for RNA-seq data with DESeq2. Genome Biol. *15*, 550. https://doi.org/10.1186/S13059-014-0550-8/FIGURES/9.

141. Korotkevich, G., Sukhov, V., Budin, N., Shpak, B., Artyomov, M.N., and Sergushichev, A. (2021). Fast gene set enrichment analysis. bioRxiv.. https://doi.org/10.1101/060012.

142. Subramanian, A., Tamayo, P., Mootha, V.K., Mukherjee, S., Ebert, B.L., Gillette, M.A., Paulovich, A., Pomeroy, S.L., Golub, T.R., Lander, E.S., et al. (2005). Gene set enrichment analysis: a knowledge-based approach for interpreting genome-wide expression profiles. Proc. Natl. Acad. Sci. USA *102*, 15545–15550. https://doi.org/10.1073/pnas.0506580102.

143. Liberzon, A., Subramanian, A., Pinchback, R., Thorvaldsdóttir, H., Tamayo, P., and Mesirov, J.P. (2011). Molecular signatures database (MSigDB) 3.0. Bioinformatics *27*, 1739–1740. https://doi.org/10.1093/BIOINFORMATICS/BTR260.

144. Myasnikov, A.G., Afonina, Z.A., Ménétret, J.F., Shirokov, V.A., Spirin, A.S., and Klaholz, B.P. (2014). The molecular structure of the left-handed supra-molecular helix of eukaryotic polyribosomes. Nat. Commun. *5*, 5294. https://doi.org/10.1038/ncomms6294.

STAR★METHODS

KEY RESOURCES TABLE

REAGENT or RESOURCE	SOURCE	IDENTIFIER
Antibodies		
Guinea pig anti-PADI6	This paper/Cambridge Research Biochemicals	N/A
Rabbit anti-OOEP	This paper/Cambridge Research Biochemicals	Cat# crb2005295
Rat anti-KHD3C	This paper/ Davids Biotechnologie GmbH	N/A
Rabbit anti-PADI6	LS Bio	Cat#LS-C373394
Rabbit anti-TLE6	Thermo Fisher Scientific	Cat#PA5-109241; RRID: AB_2854652
Mouse anti-TLE6	Sigma-Aldrich	Cat#WH0079816M1; RRID: AB_1843962
Rabbit anti-NALP5/NRP5	Abcam	Cat#ab105324; RRID: AB_10714702
Mouse anti-UHRF1	Santa Cruz Biotechnology	Cat#sc-373750; RRID: AB_10947236
Mouse anti-SKP1	Thermo Fisher Scientific	Cat#MA5-15928; RRID: AB_11153724
Mouse anti-alpha-Tubulin [DM1A]	Sigma-Aldrich	Cat#T6199; RRID: AB_477583
Rabbit anti-SPIN1	Thermo Fisher Scientific	Cat#PA5-96448; RRID: AB_2808250
Mouse anti-FBXL10/KDM2B	Thermo Fisher Scientific	Cat#H00084678-M09; RRID: AB_538764
Rabbit anti-NALP4/NLRP4	Bioss	Cat#BS-6855R
Rabbit anti-NLRP14	Abnova	Cat#PAB19311; RRID: AB_10905283
Rabbit anti-UBE2D3	Novus	Cat#NBP1-55276; RRID: AB_11014373
Mouse anti-pan-14-3-3/YWHA	Santa Cruz Biotechnology	Cat#sc-1657; RRID: AB_626618
Rabbit anti-DPPA5	Sigma-Aldrich	Cat#D2569; RRID: AB_2277471
Mouse anti-CDK1	Thermo Fisher Scientific	Cat#MA5-11472; RRID: AB_10979734
Rabbit anti-GFP	Thermo Fisher Scientific	Cat#A-11122; RRID: AB_221569
Rabbit anti-UQCRB	Abcam	Cat#ab190360; RRID: AB_2890185
Rat anti-α-tubulin	Biorad	Cat#MCA78G; RRID: AB_325005
Rabbit anti-GAPDH	Abcam	Cat# ab181602; RRID: AB_2630358
Goat Anti-Rabbit IgG H&L (HRP) antibody	Abcam	Cat# ab205718; RRID: AB_2819160
Donkey anti-Mouse IgG (H+L) Highly Cross-Adsorbed Secondary Antibody, Alexa Fluor 568	Thermo Fisher Scientific	Cat# A10037; RRID: AB_2534013
Donkey anti-Rabbit IgG (H+L) Highly Cross-Adsorbed Secondary Antibody, Alexa Fluor 488	Thermo Fisher Scientific	Cat# A-21206; RRID: AB_2535792
Donkey anti-Rabbit IgG (H+L) Highly Cross-Adsorbed Secondary Antibody, Alexa Fluor 568	Thermo Fisher Scientific	Cat# A-10042; RRID: AB_2534017
Donkey anti-Rat IgG (H+L) Highly Cross-Adsorbed Secondary Antibody, Alexa Fluor 488	Thermo Fisher Scientific	Cat# A-21208; RRID: AB_2535794
Chicken anti-Rat IgG (H+L) Cross-Adsorbed Secondary Antibody, Alexa Fluor™ 647	Thermo Fisher Scientific	Cat# A-21472; RRID: AB_2535875
Goat anti-Guinea Pig IgG (H+L) Highly Cross-Adsorbed Secondary Antibody, Alexa Fluor™ 488	Thermo Fisher Scientific	Cat# A-11073; RRID: AB_2534117
Goat anti-Guinea Pig IgG (H+L) Highly Cross-Adsorbed Secondary Antibody, Alexa Fluor™ 647	Thermo Fisher Scientific	Cat# A-21450; RRID: AB_2735091
Donkey anti-rabbit STAR 635	Abberior GmbH	Cat# ST635-1002-500UG

(Continued on next page)

Continued

REAGENT or RESOURCE	SOURCE	IDENTIFIER
Bacterial and virus strains		
One Shot™ TOP10 Chemically Competent E. coli	Thermo Fisher Scientific	Cat# C404010
Chemicals, peptides, and recombinant proteins		
HaloTag-JaneliaFluor549 ligand	Promega	Cat# GA1110
SiR-NHS ester	Spirochrome	Cat# SC003
HaloTag substrate	Promega	Cat# P6711
Hoechst 33342	Thermo Fisher Scientific	Cat# H3570
Ovine follicle stimulating hormone, oFSH	National Hormone and Peptide Programme	Cat# NDDK-oFSH-20
Collagenase IV	Thermo Fisher Scientific	Cat# 17104019
Human chorionic gonadotropin (hCG), Ovogest® 1000 I.E./ml	MSD Tiergesundheit	N/A
Pregnant mare serum gonadotropin (PMSG)	THP Medical Products	Cat# hor-272-a
Acryloyl-X	Invitrogen	Cat# A20770
Sodium acrylate	Sigma-Aldrich	Cat# 408220
Acrylamide	Sigma-Aldrich	Cat# A4058
N,N′-methylenebisacrylamide	Sigma-Aldrich	Cat# M1533
Ammonium persulfate	Thermo Fisher Scientific	Cat# 17874
Tetramethylethylenediamine	Thermo Fisher Scientific	Cat# 17919
Atto 488-NHS-ester	Sigma-Aldrich	Cat# 41698
Ethylene glycol	Sigma-Aldrich	Cat# 324558
Dimethylsulfoxid	Sigma-Aldrich	Cat# D2650
Critical commercial assays		
HiScribe T7 ARCA mRNA Kit	New England Biolabs	Cat# E2065S
Qubit RNA HS Assay Kit	Thermo Fisher Scientific	Cat# Q32852
Invitrogen™pENTR™/TEV/D-TOPO™ Cloning Kit	Thermo Fisher Scientific	Cat# K252520
Gateway™ LR Clonase™ II Enzyme-Mix	Thermo Fisher Scientific	Cat# 11791020
SensiFAST cDNA synthesis kit	Bioline	Cat# BIO-65053
Alexa Fluor® 488 fluorophore using the Alexa Fluor® 488 Conjugation Kit (Fast) - Lightning-Link®	Abcam	Cat# ab236553
QIAseq FX Single Cell RNA Library Kit	Qiagen	Cat# 180733
NextSeq 500/550 High Output Kit v2.5 (150 Cycles)	Illumina	Cat# 20024907
Deposited data		
RNA sequencing *Padi6*$^{+/-}$ vs *Padi6*$^{-/-}$ and *Tle6*$^{+/-}$ vs *Tle6*$^{-/-}$	National Center for Biotechnology Information (NCBI) GEO database	GSE222809
MASS Spectrometry *Padi6*$^{+/-}$ vs *Padi6*$^{-/-}$ and *Tle6*$^{+/-}$ vs *Tle6*$^{-/-}$	ProteomeXchange Consortium	PXD038575
Cryo-ET subtomogram averages	Electron Microscopy Data Bank (EMDB)	EMD-16458
Mouse oocyte cryo-ET tomogram	Electron Microscopy Data Bank (EMDB)	EMD-16472
Experimental models: Organisms/strains		
FVB/NRj	Janvier labs	N/A
C57BL/6JCRL	Charles River laboratories	N/A
CBA/CaOlaHsd	Inotiv	N/A
B6CBAF1	In house	N/A
B6N.B6N-PRX-Padi6(E1-HaloTag-E1') tm MS	This paper (Polygene AG)	N/A

(Continued on next page)

Continued

REAGENT or RESOURCE	SOURCE	IDENTIFIER
FVB/N-Padi6 (e3-em89)em MS	This paper (Polygene AG)	N/A
B6J.129J TLE6(PGKNeo-exon3)tm LeiLi	Prof. Lei Li (Yu et al.[67])	N/A
Human oocytes	Kinderwunschzentrum Göttingen	N/A
Oligonucleotides		
See Table S1	This paper	N/A
Recombinant DNA		
pGEMHE-Halo-Padi6	This paper	N/A
pGEMHE-Halo-Tle6	This paper	N/A
pGEMHE-Halo-Ooep	This paper	N/A
pGEMHE-Halo-Khdc3	This paper	N/A
Software and algorithms		
Prism 9	GraphPad Software	https://www.graphpad.com/
Imaris version 9.3.0	Oxford Instruments	https://imaris.oxinst.com/
Fiji (Fiji Is Just ImageJ)	Schindelin et al.[109]	N/A
Zen 2.3/3.1 (Blue edition)	Zeiss Group	www.zeiss.com/microscopy/en/products/software.html
Ilasik	Berg et al.[110]	N/A
Elastix	Klein et al.[111]	N/A
Itk-elastix	McCormick et al.[112]	https://doi.org/10.5281/zenodo.7378570
R	R Core Team[113]	N/A
SerialEM	Mastronarde[114]	http://bio3d.colorado.edu/SerialEM/
IMOD 4.11	Kremer et al.[115]	N/A
AMIRA	Thermo Fisher Scientific	https://www.thermofisher.com/de/de/home/electron-microscopy/products/software-em-3d-vis/amira-software.html
Persistence length analyses	Bäuerlein et al.[63]	N/A
Lamella in-silico clearing filter	This paper	https://doi.org/10.5281/zenodo.8370296
Spectronaut (v. 16.2.220903.53000)	Bruderer et al.[116]	N/A
ExM length error calculation	This paper	https://doi.org/10.5281/zenodo.8359490
Biorender	N/A	https://www.biorender.com/
Other		
Zeiss LSM800/900/980 confocal laser scanning microscopes	Zeiss	N/A
STED Expert line	Abberior	N/A
Leica EM TRIM 2	Leica	N/A
Leica UC7	Leica	N/A
Talos F200 G2	Thermo Fisher Scientific	N/A
Titan Krios G4	Thermo Fisher Scientific	N/A
Aquilos 2 Cryo-FIB	Thermo Fiisher Scientific	N/A
Orbitrap Exploris 480 Mass Spectrometer	Thermo Fisher Scientific	N/A
NextSeq 500/550	Illumina	N/A

RESOURCE AVAILABILITY

Lead contact
Further information and requests for resources and reagents should be directed to and will be fulfilled by the lead contact, Melina Schuh (melina.schuh@mpinat.mpg.de).

Materials availability
Plasmids are available from M.S. under a material transfer agreement with the Max Planck Society.

CellPress
OPEN ACCESS

Cell
Article

Data and code availability

- The mass spectrometry proteomics data have been deposited to the ProteomeXchange Consortium via the PRIDE[117] partner repository. Identifier in ProteomeXchange PRIDE database: PXD038575. The RNA sequencing datasets have been deposited in the National Center for Biotechnology Information (NCBI) GEO database[118] under accession number GSE222809. Cryo-ET subtomogram averages and an example of a mouse oocyte cellular tomogram are deposited under the listed identifiers in the Electron Microscopy Data Bank (EMDB) database: EMD-16458 (subtomogram averages of cytoplasmic lattice filaments) and EMD-16472 (cellular tomogram shown in Figure 3E).
- Scripts are available under https://doi.org/10.5281/zenodo.8370296 and https://doi.org/10.5281/zenodo.8359490.
- Any additional information required to reanalyze the data reported in this paper is available from the lead contact upon request.

EXPERIMENTAL MODEL AND STUDY PARTICIPANT DETAILS

Husbandry and housing conditions of experimental animals

Maintenance and handling of all mice were carried out in the MPI-NAT animal facility according to international animal welfare rules (Federation for Laboratory Animal Science Associations guidelines and recommendations). Requirements of formal control of the German national authorities and funding organizations were satisfied, and the study received approval by the Niedersächsisches Landesamt für Verbraucherschutz und Lebensmittelsicherheit (LAVES). All mice were maintained in a specific pathogen-free environment according to The Federation of European Laboratory Animal Science Associations guidelines and recommendations. Mice are housed in individually ventilated cages at 21°C and 55% relative humidity with open cage changing. Animals are provided with commercial soy-free breeding chow and water ad libitum. The following mouse lines/strains were used: HaloTag-Padi6 (C57BL/6N), Padi6-KO (FVB/N), Tle6-KO (C57BL/6J),[67] B6CBAF1 (offspring of cross between C57BL/6JCRL female and CBA/CaOlaHsd male), C57BL/6JCRL, and FVB/NRj.

Generation of mutant mouse lines

Padi6-knockout mice were generated through CRISPR/Cas9-mediated genome engineering[119] in an FVB/N background by Polygene AG. The gRNA for mouse *Padi6* (GTGCTGTTTCTCACCGGCAT(CGG)), and *Cas9* mRNA were co-injected into pronuclei of mouse zygotes to generate targeted knockout offspring. F0 founder animals were identified by PCR followed by sequence analysis, and subsequently bred with wild-type mice to test for germline transmission and to generate F1 animals. An 89 bp deletion in exon 3 of the *Padi6* gene was achieved. For genotyping, primers P1 and P2 (Table S1) were used. The wild-type and knock-out allele PCR products have a band size of 426 bp and 337 bp, respectively.

To generate the HaloTag-*Padi6* knock-in mouse line, a HaloTag sequence was inserted upstream of the endogenous *Padi6* locus on mouse chromosome 4. A previously cloned construct for HaloTag-PADI6 expression in oocytes (see below) was used as a template for the targeting vector, using a 54 bp spacer between the HaloTag sequence and the *Padi6* start codon: 5'-CTC GAG ACA AGT TTG TAC AAA AAA GCA GGC TCC GCG GCC GCC CCC TTC ACC GCC-3'. The targeting vector contained homology regions of 4.96 kb for the long arm (upstream) and 2.11 kb for the short arm (downstream) of homology and a neomycin cassette, flanked by FRT sites, inserted between exon 1 and 2 (Figure S1A). The targeting vector was transfected into C57Bl/6N-derived ES cells. Positive clones were identified with PCR and injected into grey C57Bl/6N mice-derived blastocysts. Chimeras were mated with grey C57Bl/6N Flp deleter mice and pups were analyzed by PCR for germline transmission. Mice with presence of HaloTag-Padi6 and successful deletion of the neomycin cassette were chosen for breeding. The presence of the HaloTag-*Padi6* (535 bp) or wild-type (351 bp) allele was assessed by PCR genotyping using primers P3-P5 (Table S1).

Tle6-knockout mice were a kind gift from Dr. Lei Li (Chinese Academy of Sciences, Institute of Zoology). Mice were backcrossed into the C57BL/6J background. Genotyping was performed as described in Yu et al.[67] with primers P6-P8 (Table S1).

Human oocytes

The use of unfertilized human oocytes in this study was approved by the Ärztekammer Niedersachsen (Ethics Commit-tee of Lower Saxony) under the reference 15/2016. All human oocytes used in this study were collected at the Kinderwunschzentrum Göttingen. Only immature (GV) oocytes which were unsuitable for ICSI treatment were used in this study. All patients gave informed consent for the donation of their surplus oocyte(s) to be used in this study. After collection, oocytes were incubated in G-MOPS plus (Vitrolife) medium and kept at 37°C under paraffin oil (NidaCon #NO-400K). Oocytes were fixed for immunofluorescence and expansion microscopy as described below with the following modification: Triton-X-100 was used at a final concentration of 0.5% in the fixation solution.

Bacterial strains

Molecular cloning was performed in One Shot™ TOP10 Chemically Competent E. coli (Thermo Fisher Scientific). Cells were grown in LB supplemented with appropriate antibiotics at 37°C.

METHOD DETAILS

Preparation and culture of mouse oocytes and follicles

Oocytes were isolated from 8-12-week-old female mice. Fully grown GV oocytes ($\sim$75 μm in diameter) with a central nucleus were selected for experiments and cultured in homemade M2 medium supplemented with 250 μM dibytryl cyclic AMP (dpcAMP) (Sigma Aldrich) covered with paraffin oil (NidaCon #NO-400K). For meiotic maturation experiments, oocytes were washed out of dpcAMP and fixed at different timepoints after dpcAMP release.

Follicles were isolated from 10-12-day-old (C57Bl/6j x CBA/Ca) F1 females as described previously[48] with some modifications. Briefly, ovaries were collected in MEM-alpha HEPES GlutaMAX (ThermoFisher, #42360024) supplemented with 5% fetal bovine serum (FBS) (Gibco, #16000044), 1x Insulin-Transferrin-Selenium (ITS) (ThermoFisher Scientific, #41400045), 0.01 μg/ml ovine follicle stimulating hormone, oFSH (National Hormone and Peptide Programme, NDDK-oFSH-20), and 0.1x Penicillin-G/Streptomycin (Gibco) and dissociated enzymatically with addition of 2 mg/ml collagenase IV (Thermo Fisher Scientific #17104019) for a total of 10 minutes. Follicles with a diameter of $\sim$100 μm with uniformly surrounding granulosa cells were collected for microinjection. A maximum volume of 5 pl were injected into the follicles. Following microinjection, the follicles were transferred to collagen-coated inserts (Corning, #3491/3493) and incubated in MEMα medium (Gibco, #32571028) supplemented with 5% FBS, 1x ITS, 0.01 μg/ml oFSH, and 0.1x Penicillin-G/Streptomycin at 37°C/5% CO$_2$. Medium surrounding the insert was exchanged every 3 days. Mature GV oocytes were harvested in modified M2 medium with 10% FBS instead of 4 mg/ml bovine serum albumin (BSA) after 9 days of culture.

In vitro fertilization of mouse eggs

8-12-week-old females (HaloTag-*Padi6* or CBAB6-F1) were super ovulated by injection of 5 IU pregnant mare serum gonadotropin (THP Medical Products, #hor-272-a) followed 48 h later by injection of 5 IU human chorionic gonadotropin (hCG, Intervet, Ovogest® 1000). 13 hours after hCG injection, meiosis II arrested eggs were harvested from the oviducts and cultured as described previously.[120] Sperm was collected from >12-week-old C57BL/6J × CBA/CaOlaHsd (CBAB6-F1) males and capacitated for 2 h in HTF medium (Millipore, #MR-070-D) supplemented with 2 mM Hypotaurine (Sigma, #H1384). Subsequently, IVF was performed in a 40 μl droplet of HTF medium under paraffin oil (NidaCon #NO-400K) by adding 2–5 μl of capacitated sperm. After 4-6 hours, zygotes were transferred to Advanced KSOM medium (Merck, #MR-101-D) and incubated at 37°C/5% CO$_2$ for *in vitro* preimplantation embryo development.

Microinjection of mouse oocytes and immature follicles

Microinjection of both oocytes and follicles was carried out as previously described.[48,121,122] In brief, oocytes and follicles were loaded onto an injection shelf assembled by overlaying two coverslips separated by one (for GV oocytes) or two (for follicles) layers of 100 μm thick double-sided tape. For GV oocytes 8 pl of mRNA at the following concentrations was injected: HaloTag-*Padi6* at 1.5 μg/μl, HaloTag-*Tle6* at 1.5 μg/μl, HaloTag-*Ooep* at 1.5 μg/μl, HaloTag-*Khdc3* at 1.5 μg/μl, H2B-mClover3 at 8 ng/μl. For immature follicles 5 pl of mRNA at the following concentrations was injected: HaloTag-*Padi6* at 1.5 μg/μl, HaloTag-*Tle6* at 1.5 μg/μl, HaloTag-*Ooep* at 1.5 μg/μl, HaloTag-*Khdc3* at 1.5 μg/μl, mClover3-*Padi6* at 1 μg/μl. For GV oocytes, an mRNA expression period of 3 hours in presence of dpcAMP was given before continuing the experiment.

Expression constructs and in vitro mRNA synthesis

To generate expression constructs of the *Padi6* and *SCMC* genes, *Padi6*, *Tle6*, *Ooep*, and *Khdc3* were amplified from oocyte cDNA libraries generated using a SensiFAST cDNA synthesis kit (Bioline #BIO-65053). Primers used for plasmid construction are shown in Table S1 (P9-P18). First, pENTR/dTOPO-*Padi6*, pENTR/dTOPO-*Tle6*, pENTR/dTOPO-*Ooep*, pENTR/dTOPO-*Khdc3* were generated for subcloning into pGEMHE-Halo-gateway destination vectors using primers P9-P16 and the Invitrogen™pENTR™/TEV/D-TOPO™ Cloning Kit (Thermo Fisher Scientific, #K252520). To generate pGEMHE-Halo-gateway destination vectors the published HaloTag sequence[123] was amplified using primers (P17 and P18). The amplified sequence was subcloned into pGEMHE-gateway destination vectors using NheI/XhoI restriction enzymes. For generation of Halo-PADI6/SCMC expression vectors, pENTR/dTOPO entry vectors were incubated with pGEMHE-Halo-gateway destination vectors for the LR reaction using the Gateway™ LR Clonase™ II Enzyme-Mix (Thermo Fisher Scientific, #11791020) generating pGEMHE-Halo-*Padi6*, pGEMHE-Halo-*Tle6*, pGEMHE-Halo-*Ooep*, and pGEMHE-Halo-*Khdc3* expression vectors. From these constructs, mRNAs were *in vitro* synthesized using the HiScribe T7 ARCA mRNA Kit (NEB # E2065S) following the manufacturer's instructions. mRNA concentration was quantified using a Qubit RNA HS Assay Kit (Thermo Fisher Scientific #Q32852).

Immunofluorescence

Oocytes were fixed in 100 mM HEPES (pH 7.0, titrated with KOH), 50 mM EGTA (pH 7.0, titrated with KOH), 10 mM MgSO4, 2% methanol-free formaldehyde, and 0.2% triton X-100 at 37°C for 30 min. Fixed oocytes were extracted in phosphate-buffered saline (PBS) with 0.5% triton X-100 (PBT) overnight at 4°C and blocked in PBT with 3 % BSA (PBT-BSA) for 5 hours at room temperature. All primary antibodies were incubated overnight at 4°C followed by 3 x 15-minute washes in 3% PBT-BSA. Secondary antibodies were used at 5 μg/ml and incubated for 1.5 hours at room temperature. DNA was stained with Hoechst 33342 (Molecular Probes) at

100 μM. For immunofluorescence of oocytes expressing HaloTag-fusion proteins, cells were incubated in 1 μM HaloTag-JaneliaFluor549 ligand (Promega, GA1110) or Halo-5'-SiR (in-house conjugation of HaloTag substrate (Promega, # P6711) and a SiR-NHS ester (Spirochrome, # SC003)) for 20 minutes prior to fixation. For embryos, MII eggs were incubated with the fluorescent HaloTag-ligand prior to IVF.

A guinea pig anti-PADI6 antibody was raised against a synthetic peptide corresponding to amino acids 123-140 (YRDGQLDMPSDKQAKKKW) of mouse PADI6 where the methionine residue at position 130 was changed to norleucine to stop the formation of metoxide. The antibody was affinity purified by affinity purification (Cambridge Research Biochemicals). A rabbit anti-OOEP antibody was raised against a synthetic peptide corresponding to amino acids 2-19 of mouse OOEP (ASHTADADAKPDSDSQKL-amide), and was further purified with affinity purification (Cambridge Research Biochemicals). A rat anti-KHDC3 was raised against a synthetic peptide corresponding to amino acids 1-20 of mouse KHDC3 (MASLKRFQTL VPLDHKQGTL) (Davids Biotechnologie GmbH). Further antibodies used were: rabbit anti-PADI6 (LS Bio, #LSC373394), rabbit anti-TLE6 (Thermo Fisher Scientific, #PA5-109241), mouse anti-TLE6 (Sigma-Aldrich, #WH0079816M1), rabbit anti-NALP5/NLRP5 (Abcam, #ab105324), mouse anti-UHRF1 (Santa Cruz Biotechnology, #sc-373750), mouse anti-SKP1 (Thermo Fisher Scientific, #MA5-15928), mouse anti-α-tubulin[DM1A] (Sigma-Aldrich, #T6199), rabbit anti-SPIN1 (Thermo Fisher Scientific, #PA596448), mouse anti-FBXL10/KDM2B (Thermo Fisher Scientific, #H00084678-M09), rabbit anti-NALP4/NLRP4 (Bioss, #BS-6855R), rabbit anti-NLRP14 (Abnova, #PAB19311), rabbit anti-UBE2D3 (NovisBio, #NBP1-55276), mouse anti-pan-14-3-3/YWHA (Santa Cruz Biotechnology, #sc-1657), rabbit anti-DPPA5 (Sigma-Aldrich, #D2569), mouse anti-CKD1 (Thermo Fisher Scientific, #MA5-11472), rabbit anti-GFP (Thermo Fisher Scientific, #A111-22), rabbit anti-UQCRB (Abcam, #ab190360), and rat anti-α-tubulin (Biorad, #MCA78G). AlexaFluor488-, 546-, 568-, or 647-conjugated rabbit IgG, mouse IgG, rat IgG, or guinea pig IgG highly cross-adsorbed secondary antibodies were used (Thermo Fisher Scientific). All secondary antibodies were raised in donkey or goat.

Direct coupling of anti-PADI6 primary antibody

Guinea pig anti-PADI6 antibodies (Cambridge Research Biochemicals) were purified and buffer-exchanged into PBS by ultrafiltration (Merck Millipore #UFC510024). Primary anti-PADI6 antibodies were conjugated to an Alexa Fluor® 488 fluorophore using the Alexa Fluor® 488 Conjugation Kit (Fast) - Lightning-Link® (Abcam, ab236553) following kit instructions. The directly labelled antibody was used at 0.07 mg/ml concentration.

Expansion microscopy

The expansion microscopy (ExM) protocol was based on the pro-ExM in published literature[49–51] and adapted for use with mammalian oocytes. Chemically fixed oocytes were incubated in 0.1 mg/ml Acryloyl-X (AcX; Invitrogen, A20770) in PBS for 2 hours[50] at room temperature and subsequently washed 2x 15 minutes in 1X PBS. Cells were transferred to a glass slide mounted with a silicon well separator with a diameter of 3 mm (Grace bio-labs, #103350). Excess PBS was aspirated and the gelation solution was carefully added to the well (8.625% sodium acrylate (Sigma-Aldrich, 408220), 20% acrylamide (Sigma-Aldrich, A4058), 0.075% N,N'-methylenebisacrylamide (Sigma-Aldrich, M1533), 2M NaCl, 0.2% Ammonium persulfate (APS; Thermo Fisher Scientific, 17874), 0.2% Tetramethylethylenediamine (TEMED; Thermo Fisher Scientific, 17919). The gelation solution was based on a published ExM protocol[51] and was found to work well in mammalian oocytes. Gels were incubated at 37°C in a humidifying camber for 1 hour for gelation. Gel denaturation was performed in an alkaline denaturation solution (100 mM Tris (Sigma-Aldrich, T1503), 5% (w/v) Triton-X-100 (Sigma-Aldrich, 93443), 1 % SDS (Sigma-Aldrich, L3771) at 121°C for 1 hour in an autoclave at liquid sterilization mode as recommended for post-expansion labelling.[50] Following denaturation, gels were washed in PBS and subsequently incubated with primary antibodies in 3% PBT-BSA for 12-24 hours. All antibodies were used at a 1:100 dilution, apart from anti-KHDC3 (David Biotechnologies) which was used at a 1:10 dilution. All antibodies used are listed under section immunofluorescence above. Following a 4x30-minute wash in 3% PBT-BSA, gels were incubated with secondary antibodies at 5 μg/ml for 12-24 hours followed by another 4x30-minute wash step in 3% PBT-BSA. The gels were incubated with an Atto 488-NHS-ester (Sigma-Aldrich, 41698) at 20 μg/ml in PBS for 1 hour at room temperature after secondary antibody incubation. Finally, gels were expanded in H_2O overnight at room temperature.

The degree of expansion was calculated by measuring the size of easily distinguishable landmarks in the oocyte such as the nucleus, the spindle, and the whole cell size, before and after processing for ExM. Before fixation at either the GV stage or MI stage (6.5 hours after release from dpcAMP), the zona pellucida was removed with a short incubation in Tyrode's solution to improve fixture to the coverslip. Oocytes were immunostained with an anti-α-tubulin antibody (Biorad, #MCA78G) and glued to a coverslip using CellTak (Corning, #354240) for the pre-ExM image acquisition. Oocytes were subsequently processed for ExM as described above, taking care to minimize cell distortion. The oocytes were re-imaged after ExM and the same microtubule structures were identified in both pre- and post-ExM images.

The measurement length (ML) error quantifies the putative distortion induced by a non-isotropic expansion of the gel. We used the same approach as in M'Saad and Bewersdorf[55] where the ML error is denoted root mean squared (RMS) error. We defined matching region of interests (ROIs) in pre-ExM and post-ExM images. We used elastix[111,124] and itk-elastix[112] to register the post-ExM to the pre-ExM image and computed a similarity transform (translation, rotation, and scaling), an affine transform (translation, rotation, scaling, and shear), and a non-rigid transform using B-splines. To allow for reliable minimization, transformations are applied sequentially in order of complexity starting from the rigid transform, followed by the similarity and affine transform up to the non-rigid transform. The non-rigid transform represents the best possible registration of the two images accounting for potential non-isotropic

CellPress
OPEN ACCESS

expansion of the gel. For the B-splines we used a final grid spacing in the pre-ExM of 1 μm and a regularization weight of 1 and 3. Mathematically we compute the forward transform. Applying the backward transform yields a deformed post-ExM image that is registered to the pre-ExM. To compute the ML error, we used ilastik[110] to segment interphase microtubules in GV oocytes or the whole spindle in metaphase I oocytes in the pre-ExM images. The binary mask was further processed to yield the binary skeleton (microtubules) or object boundary (spindle). We finally extracted a point set with x and y coordinates for the different regions. Using the previously computed transforms we forward transformed the pre-ExM point set to obtain a point set registered to the post-ExM image. For each point pairs separated by a distance L_{sim} (L_{aff}) in the similarity (affine) transformed point set, we can compute the ML error as $|L_{sim} - L_{bspline}|$ ($|L_{aff} - L_{bspline}|$) where $L_{bspline}$ is the distance of the same point pairs in the non-rigid transformed point set. The expansion factor was calculated by the ratio of the L_{sim}/L_{preExM}, L_{preExM} is the distance of the same points in the pre-ExM image. We used a length cut-off of 5 and 10 μm for the GV and MI oocytes, respectively. The script for the measurement length error calculations can be found under doi.org/10.5281/zenodo.8359490.

Confocal microscopy

For confocal microscopy, oocytes were imaged in M2 medium (for live cells) and PBS (for fixed cells) covered with paraffin oil (NidaCon #NO-400K) in a 35 mm glass bottom dish with coverslips #1 (MatTek) or #1.5H (Ibidi). For expansion microscopy, gels were embedded in 1% agarose in H_2O and imaged on 35 mm dishes with #1.5H coverslips (Ibidi). Images were acquired with LSM800/880/900/980 laser scanning confocal microscopes (Zeiss) equipped with an incubator chamber and a 40x C-apochromat 1.2 NA water-immersion objective (Zeiss). Airyscan images were acquired using the LSM800/880/900/980 confocal laser scanning microscopes equipped with an Airyscan module (Zeiss) and processed in ZEN (Zeiss) after acquisition. Care was taken that the laser power, pixel-dwell time, and detector gain did not cause phototoxicity, photobleaching, or saturation.

STED microscopy

3D STED microscopy of expanded oocytes was performed with a STED Expert line microscope (Abberior Instruments GmbH, Göttingen) equipped with a pulsed 775 nm STED laser module (up to 1200 mW at 40 mHz). A UPLSAPO 60x 1.2 NA water-immersion objective (Olympus) was used for all image acquisition of expanded gels. The diffraction limit in 3D mode was measured to ~200 nm in all dimensions (x,y,z). This was done by extracting the PSF full width at half maximum in x, y, and z from line profiles over 40 nm beads, fitting a gaussian curve of the line profile intensities. An isotropic voxel size of 50 nm was used for 3D STED image acquisition. For STED microscopy, a donkey anti-rabbit STAR 635 (ST635-1002-500UG, Abberior GmbH) secondary antibody was used and excited with a 640 nm excitation laser.

Fluorescence recovery after photobleaching (FRAP)

For analysis of cytoplasmic lattice dynamics, oocytes expressing an mClover3-PADI6 reporter protein were bleached using the bleaching module of a Zeiss LSM800 confocal microscope. Squares of 10 μm x 10 μm were drawn in 3 regions of interest (ROI); two within the oocyte cytoplasm of which only one was bleached, and one outside the cell for background calculations. A 488 nm excitation laser line at maximum power was used for bleaching at the 4th time point.

Scanning transmission electron tomography
Sample preparation and microscopy

For electron microscopy, GV mouse oocytes were fixed in 100 mM HEPES (pH 7.0, titrated with KOH), 50 mM EGTA (pH 7.0, titrated with KOH), 10 mM MgSO4, 3 % EM-grade glutaraldehyde, 0.5% methanol-free formaldehyde at 37°C for 1 hour.

Fixed oocytes were embedded in 2% low-melt agarose (Sigma-Aldrich, #A0701-25G) in H_2O. Agarose embedded oocytes were post-fixed and heavy metal-contrasted first with 1% osmium tetroxide (Electron microscopy sciences, #19132) in 0.1 M cacodylate buffer (Sigma-Aldrich, #C0250-100G) and then with 2% aqueous uranyl acetate (SPI Supplies, #2624), each for 60 min at RT as described previously.[27] Stained samples were subsequently dehydrated via sequential 10 min immersions through an increasing gradient of ethanol concentrations and embedded in epoxy resin. Plastic-embedded oocytes were prepared for sectioning with a high-speed milling device (Leica EM TRIM 2) and an ultramicrotome (Leica UC7) equipped with a 35° diamond knife (Diatome) which was used to collect 500 nm-thick sections through oocytes onto formvar-coated, 100-mesh parallel line copper grids (Gilder). Both surfaces of collected sections were labelled with 15 nm gold fiducial markers by floating grids on droplets of diluted Protein A-gold (UMC Utrecht) and then coated with 5 nm of evaporated carbon using a CCU-010 HV vacuum coating device (Safematic).

Oocytes were visualized in a Talos F200 G2 (Thermo Fisher Scientific) scanning/transmission electron microscope operated at 200 kV and equipped with a Model 2040 dual-axis high-angle tomography holder (Fischione). STEM imaging was performed in microprobe mode with a beam semi-convergence angle of 3.6 mrad and images were acquired (2048 x 2048; pixel size 1.2 nm; dwell time 15 μs) using an on-axis brightfield detector with a collection angle of 10 mrad. Continuous tilt series were acquired (tilt range +/- 60°; 2° increments) from orthogonal axes in dynamic focus mode using SerialEM software (http://bio3d.colorado.edu/SerialEM/) and reconstructed using weighted back-projection implemented by eTomo (IMOD software package[115]) to obtain 3D tomographic oocyte subvolumes containing cytoplasmic lattices.

Filament tracing and analysis

For filament tracing, the tomograms were gaussian filtered with a kernel of 6 nm and resampled to 5 nm pixel size. The CPL filaments were then automatically detected using the XTracing Module in Amira (Thermo Fisher Scientific).[125] 3D visualizations were created using Amira. Persistence length was calculated by an in-house MATLAB (MathWorks) script.[63] Filament neighbour analyses were conducted as described in Jasnin et al.[126] We estimated the cellular volume occupied by CPL bundles as the volume occupied by filaments plus the space between filaments within a bundle. To that end, individual filaments were dilated to a diameter of 75 nm, thereby fusing with all neighbouring filaments, followed by an erosion to 40 nm filament diameter at the bundle surface.

Cryoelectron tomography

Vitrification

Holey carbon-coated 200 mesh molybdenum electron microscopy (EM) grids were use as support for the oocytes. The EM grids were first plasma cleaned for 30s in a plasma cleaner (Harrick Plasma PDC-32G-2) to decrease hydrophobicity. The zona pellucida was removed from GV oocytes by a short incubation in Tyrode's solution. Subsequently, GV oocytes were incubated in a series of increasing concentrations of DMSO/EG in M2 medium to enable vitrification: 1.75%/1.75% DMSO/EG for 3 min, 2.33%/2.33% DMSO/EG for 3 min, 3.5%/3.5% DMSO/EG for 6 min, and finally, in the final concentration of 7.5%/7.5% DMSO/EG for 3 min. The EM grid was clamped in a inverse tweezer (Dumont). 15 μL of the final cryoprotectant solution were pipetted on the grid and then placed under the stereo microscope. Oocytes were selected under a stereo microscope (Stemi 508, Zeiss) and transferred with a fine glass pipette to place 4-6 oocytes precisely around the center of the EM grid. To maintain the positioning of the oocytes on the grid, the excess cryoprotectant solution was removed by pipetting just before plunge freezing. The grids were then mounted on a manual plunger, blotted from the back side using Whatman paper #1 (Sigma-Aldrich) and plunged into a 2:1 ethane:propane mixture cooled down to liquid nitrogen temperature.

Cryo-FIB milling

To prepare thin electron transparent lamellae into the oocytes, plunge-frozen grids were first mounted into Autogrid frames (Thermo Fisher Scientific). Autogrids were loaded into a dual-beam Aquilos II focused ion beam (FIB) / scanning electron microscope (SEM) (Thermo Fisher Scientific). The samples were kept at -190 °C throughout FIB milling by the microscope cryo-stage. Overview maps of the EM grid were acquired by SEM at 10 kV at 100-250x magnification (object pixel size 1.1 or 0.4 μm, respectively) and panorama views by secondary electrons were produced using the FIB at 30 kV and 338x magnification (object pixel size 0.7 μm; Figures S4B and S4C). Gaseous organic platinum was deposited on top of the sample using the gas injection system for 60 s at the standard stage position. To efficiently produce lamellae from these large cells, we developed a "deep-FIBing" approach. First, an oocyte was centred and the stage was rotated by 180° compucentric rotation to enable milling under 90° (Figure S4D). With an ion beam current of 5 nA, a 40 μm wide surface was milled in the oocyte in a few minutes (Figure S4E). With an ion beam current of 1 nA, uneven surface structures were removed to create a smooth, clean surface perpendicular to the EM grid. Biological structures in this cross section through the oocyte were imaged by SEM at 3.0 kV, 13 pA, 300 ns dwell time, 3072x2048 in integration mode (128-256x magnification; Figure S4F). To improve the interpretability of the cellular content of the SEM micrograph of the newly created surface, the micrograph was computationally filtered by a combination of a high-pass FFT filter (to remove charging artefacts) and contrast limited adaptive histogram equalization in Fiji[109] to further enhance contrast (Figure S4G). This allowed to screen for an interesting region in the oocyte by removing more material and consecutively imaging the exposed surface until the final positioning of the lamella was determined. To protect the milling front of the lamellae, gaseous organic platinum was frozen a second time on the sample from an angle similar to the milling direction. As the deposition of the organic platinum creates an electrically insulating layer, charge drainage spots were created by removing material down to the grid bars around the oocyte with an ion beam current of 5 nA. To further improve the electrical conductivity of the sample surface, a thin layer of pure metallic Pt was sputtered onto the grid within the FIB/SEM using the following parameters: 30 mA sputtering current, 1000 V between stage and sputtering target and 33 s of exposure at 0.1 mbar resulting in ∼1000 mC of sputtered Pt. To prevent bending of the lamella during the preparation and fracturing of the lamella due to thermal expansion/shrinking during later transfers, the lamella was disconnected at one side with a notch.[87] Approximately 1000 μm^2 large lamellae (∼20 μm wide, ∼50 μm long) were prepared into the oocytes using the FIB at 30 kV at shallow angles (8-14°) in four consecutive steps: first, about a third of the oocyte volume was removed above and below the intended lamella site using an ion beam current of 5 nA with 10 μm spacing in 5-10 min. Further rectangular patterns were defined above and below the intended lamella with 3 μm spacing for the rough milling step (ion beam current of 1000 pA), followed by fine milling with 1000 nm spacing (300 pA) and the final two polishing steps down to first 300 nm spacing, and then the final lamella thickness of 100-200 nm (50-100 pA; Figures S4H and S4I). To reach a uniform thickness, the lamella was tilted by 0.5° and milled only on the top with 50-100 pA (Figures S4J and S4K). The thickness of the lamella during the polishing step was assessed by SEM at 3-5 kV, 4.1 pA: the loss of charging effects in the lamella (i.e. vanishing of bright areas) indicates a thickness <300 nm at 5 kV or <200 nm at 3 kV. Cellular structures inside the lamella at the surface were imaged at each step by SEM at 2.5 kV, 4.1 pA in integration mode (64x; Figure S4I).

Cryo-ET imaging

Cryo-FIB lamellas were imaged using a Titan Krios G4 cryo-transmission electron microscope (Thermo Fisher Scientific) equipped with a field emission gun operated at 300 kV, a Selectris post-column energy filter (Thermo Fisher Scientific) operated at zero-loss and a Falcon IV direct electron detector (Thermo Fisher Scientific). Low magnification projections of lamellas were recorded (4.800 x,

object pixel size 2.593 nm) using the montage option in SerialEM[114] and stitched using ICE (Microsoft Research) to produce complete lamella overviews. Lamella imperfections dominating the contrast, like curtains and large-scale thickness variations, were cleared by the "Lamella *in-silico* clearing" filter[56] (https://doi.org/10.5281/zenodo.8370296/github.com/FBauerlein/LisC_Algorithm). High magnification (33,000x or 53,000x, object pixel size 0.365 or 0.232 nm, respectively) tilt series were recorded at locations of interest using the SerialEM low dose acquisition scheme with 1.9-3.5 e⁻/Å² per projection, a tilt increment of $3°$, typically spanning an angular range from $-60°$ to $+60°$ depending on the pre-tilt of the lamella. Target defocus was set between -3 to -5 μm. The camera was operated in dose fractionation mode recording in EER format, which enables post-acquisition fractionation. The total dose was limited to 70-150 e⁻/Å².

Tomogram reconstruction and analysis

Raw EER files were aligned using version 4.11 of the IMOD package.[127] The resulting tilt series were dose filtered and partially obstructed projections excluded. The resulting tilt series were aligned using patch tracking in IMOD and reconstructed by weighted back projection. The sputtered Pt layer was computationally removed using the masktomrec package.[128] Tomograms were denoised and the missing wedge complemented by IsoNet.[129] Filament tracing was performed as described above, but contrast was enhanced for the cryo-ET tomograms by filtering with tom deconv (https://github.com/dtegunov/tom_deconv) within MATLAB 2021b.

Subtomogram averaging

The defocus value of each motion-corrected tilt image (not dose-filtered) was estimated using CTFFIND 4.1.14.[130] Afterwards, the dose-filtered images were CTF corrected by the CTFphaseflip routine using the IMOD 4.11. The tomographic volume was subsequently reconstructed using weighted back-projection in IMOD.[115] The subtomogram averaging procedure was performed using the Dynamo software package[131] on five tomograms obtained from FIB-milled lamellae. Fourier transform analysis indicated a periodicity of 38 nm (Figure 3D, inset). Therefore, the coordinates of the traced filaments were imported into Dynamo and sampled every 26 pixels (38 nm) employing the "filamentWithTorsion" geometric model. Subvolumes with a box size of 96 pixels were extracted along the spline connecting these points. In total, 1246 subvolumes from 433 filaments were extracted from bin 4 tomograms (14.61 Å/px). The initial reference was generated de novo by randomizing the in-plane azimuthal angle and averaging the subvolumes. The subvolumes were aligned against the reference low-pass filtered to 42Å using a cylindrical alignment mask with a diameter of 32 pixels. The alignment was performed using a cone search range of $360°$ with a $30°$ step (4 iterations), and an in-plane angular search range of $360°$ with a $30°$ step size (4 iterations). Subtomograms were re-extracted from bin 2 tomograms (7.305 Å/px) using a box size of 192 pixels, separated into two random half-data sets, and aligned and averaged independently. Successive rounds of local alignment and averaging were applied with a cone search ranging from $45°$ to $6°$ in $5°$ to $1°$ steps, and an in-plane angular search ranging from $30°$ to $6°$ with steps of $5°$ to $1°$. The FSC curve calculation and resolution estimation was carried out using Relion 3.1[132] by masking the central filament, which resulted in the final average reconstruction with a global resolution of 30 Å using the 0.143 criterion. To focus the alignment on the surrounding filaments, the globally aligned subvolumes extracted from bin 4 tomograms were locally aligned using a mask with a diameter of 80 pixels, excluding the central filament. Figures were prepared using the Chimera 1.16 package[133] and the 3dmod interface in IMOD 4.11.

Immunoblotting

For immunoblots of PADI6 and HaloTag-PADI6, 10 GV mouse oocytes were probed per lane. Collected cells were washed through BSA-free M2 medium and snap-frozen in liquid nitrogen. 5 μl 4X NuPAGE sample buffer (Thermo Fisher Scientific, #NP0007) with 100 mM DTT was added to 15 μl of cell lysate and immediately snap-frozen. The cells were snap-frozen and thawed for a total of 3 times before boiling at $95°$C for 5 minutes. Samples were resolved on a 10 well NuPAGE 4-12% bis-tris protein gel of 1.0 mm thickness (Thermo Fisher Scientific #NP0301BOX) with 1 X NuPAGE MOPS running buffer (Thermo Fisher Scientific #NP0001). Proteins were transferred to a 0.45 μm PVDP membrane (Thermo Fisher Scientific #LC2005) with 1X NuPAGE transfer buffer (Thermo Fisher Scientific #NP0006) with 20% methanol and run at 110 V for 1 hour and 10 minutes on ice. Blocking and antibody incubations were done in PBS with 5% skimmed milk and 0.05% Tween-20. Primary antibodies used were rabbit anti-PADI6 (LS Bio, LSC373394) (1 μg/ml), rabbit anti-GAPDH (Abcam, ab181602) (2 μg/ml). Primary antibodies were incubated overnight at $4°$C. A Goat Anti-Rabbit IgG H&L (HRP) antibody (Abcam, #ab205718) secondary antibody used was and incubated for 1 hour at room temperature. Immunoblots were developed with Pierce ECL Western blotting-substrate (ThermoFisher Scientific, #32106) or SuperSignal West Femto Maximum Sensitivity Substrate Femto (ThermoFisher Scientific, #34094) and imaged with an Amersham Imager 600 (GE Healthcare).

DIA mass spectrometry

Sample preparation

For data-independent acquisition (DIA) proteomic analysis, mouse GV oocytes were collected in M2 media without BSA. For data-independent acquisition (DIA) analysis, 120 GV mouse oocytes from *Padi6*⁺/⁻, *Padi6*⁻/⁻, *Tle6*⁺/⁻, and *Tle6*⁻/⁻ were collected per replicate for a total of three biological replicates per sample. Collected oocytes were snap-frozen in liquid nitrogen and stored at -80°C awaiting further processing.

Cell lysis was performed using SDS lysis buffer (4% [w/v] SDS, 150 mM NaCl, 50 mM Hepes-NaOH pH 7.5, 2 mM DTT, 0.5% [v/v] NP40, 1X Roche complete protease inhibitors-EDTA), which was added to frozen cells, followed by incubation at 99 °C for 10 min and

Cell
Article

sonication for 10 min with 30 sec on/off cycles at 20°C using a Bioruptor (Diagenode) at the highest output level. Samples were diluted to a final concentration of 0.1% SDS and 1 mM MgCl2 was added. DNA was digested using 500U of Pierce™ Universal Nuclease (ThermoFisher Scientific; 88700) for 30 min at 37°C, 300 rpm. Proteins were reduced by incubation with 5 mM dithiothreitol (DTT) for 30 min at 37°C, 300 rpm, and alkylated by incubation with 20 mM iodoacetamide (IAA) for 30 min at 25°C, 300 rpm, in the dark. The reaction was quenched by addition of another 5 mM of DTT and subsequent incubation for 5 min at 25°C, 300 rpm. Sample cleanup was performed by applying the single-pot, solid-phase-enhanced sample preparation (SP3) protocol by.[134] Briefly, carboxylate modified magnetic beads (Cytiva; 65152105050350, 45152105050250, mixed 1:1) were added at a 1:10 protein-to-bead mass ratio and an equal volume of 100% acetonitrile (ACN) was added to induce protein binding to the magnetic beads. Washing was performed twice with 80% EtOH and once with 100% ACN. Proteins were digested on beads in 100 mM NH4HCO3 containing trypsin (Promega, V5111) at a 1:20 enzyme-to-protein ratio (assuming 25 ng total protein amount per cell) ON at 37 °C, 1000 rpm. Peptides were removed from the magnetic beads and dried in a vacuum concentrator before DIA LC-MS/MS analysis.

DIA LC-MS/MS analysis of GV oocytes
Peptides from *Padi6* or *Tle6* +/- or -/- GV oocytes were dissolved in 2% ACN, 0.05% trifluoroacetic acid (TFA) and subjected to DIA LC-MS/MS analysis using an Orbitrap Exploris 480 Mass Spectrometer (Thermo Fisher Scientific) coupled to a Dionex Ultimate 3000 RSLCnano system. Peptides were loaded on a Pepmap 300 C18 trap column (Thermo Fisher Scientific) (flow rate, 10 μl/min) in buffer A (0.1% [v/v] FA) and the column was washed subsequently for 3 min with buffer A. Peptide separation was performed on an in-house packed C18 column (30 cm; ReproSil-Pur 120Å, 1.9 μm, C18-AQ; inner diameter, 75 μm; flow rate: 300 nl/min) by applying a two-step linear gradient of buffer B (80% [v/v] ACN, 0.08% [v/v] FA). The main column was equilibrated with 5% buffer B for 3 min, before samples were applied. Two subsequent linear gradients from 5-14% buffer B over 27 min and from 14-48% over 77 min were applied to elute peptides, followed by 4.8 min washing at 90% buffer B and 6 min at 5% buffer B. Eluting peptides were analyzed in positive mode for 118 min using a data-independent acquisition (DIA) method. Resolution was set to 120,000 (MS1) and 30,000 (MS2) FWHM, AGC targets to 3x106 (MS1) and 106 (MS2), maximum injection time to 20 ms (MS1) and 55 ms (MS2) and MS1 scan range to m/z 350-1650. MS2 scans were acquired after every MS1 scan, using tMS2 option in Thermo Xcalibur Instrument Setup software, in 70 m/z windows (Table S2). Precursors were fragmented using 30% normalized, higher-energy collision-induced dissociation (HCD) fragmentation.

For all measurements, the lock mass option (m/z 445.120025) was used for internal calibration.

DIA MS database search
DIA data was processed using Spectronaut (v. 16.2.220903.53000).[116] For library generation, DDA LC-MS/MS data from fractionated mouse oocyte samples[135] were searched using the Pulsar search engine platform and a protein sequence database including canonical and isoform sequences downloaded from UniProt Knowledgebase (date of download: 10.09.2021; 17077 protein sequences). The database search was performed using the default BGS Factory settings including: enzyme, trypsin/P; fixed modification, carbamidomethyl (C); variable modifications oxidation (M), acetylation (protein N-term). The resulting spectral library was used for library-based DIA data analysis. Default BGS Factory settings were applied. Global imputation and local normalization were enabled for all analyses. Differential abundance testing was performed using Spectronaut post analysis option. An unpaired t test was performed based on the log$_2$ ratios of protein intensities and p-values were corrected for multiple testing.[136]

For downstream analyses, only proteins with >2 unique peptides detected were considered.

STRING enrichment analysis
For pathway enrichment analysis, the Search Tool for the Retrieval of Interacting Genes/Proteins (STRING) was used https://string-db.org/[68]. Depleted proteins in either *Padi6*$^{-/-}$ or *Tle6*$^{-/-}$ oocytes were listed in the search tool indicating *mus musculus* as the input organism, and all enriched terms were exported.

RNA sequencing and data analysis
GV oocytes were collected from three *Padi6*$^{+/-}$ and three *Padi6*$^{-/-}$ mice, or two *Tle6*$^{+/-}$ and four *Tle6*$^{-/-}$ mice. Cells were washed through PBS and transferred in 2 μl PBS to a 1.5 ml Eppendorf tube. An ERCC RNA Spike-In Mix (4456740, ThermoFisher scientific) was added before lysis in a 1:50000 final dilution. The QIAseq FX Single Cell RNA Library Kit (Qiagen #180733) was used for library preparation following kit instructions. Each library was sequenced at an average sequencing depth of 50 million reads using a NextSeq 500/550 (Illumina). The resulting FASTQ files were trimmed for quality and the presence of adapter sequences using cutadapt 2.8[137] using the "-q 20 -m 35 -j 15" parameters. Read mapping and counting against Gencode GRCm39 reference genome and the VM26 annotation file were performed with the splice-aware aligner STAR 2.7.8a[138] and HTSeq 2.0.2,[139] respectively. Differential gene expression analysis was accomplished with DESeq2 v1.32.0[140] package in R.[113] Gene set enrichment analysis (GSEA) was performed using fgsea v1.18.0[141] package in R and the MSigDB[142,143] C5 (ontology) gene set.

QUANTIFICATION AND STATISTICAL ANALYSIS

Statistical analysis
The standard deviation was used for error bars for box charts. Statistical significance based on unpaired, two-tailed Student's t test (for comparison of two groups) was calculated in GraphPad Prism 9. For comparison of three groups, a one-way ANOVA test was performed in GraphPad Prism 9. All data are from at least two independent experiments. P-values are indicated with exact values.

Cell
Article

Image analysis and quantification

Images were analyzed in Fiji,[109] Imaris (Oxford Instruments), Ilastik,[110] or ZEN (Zeiss). Exported data were further processed in Microsoft Excel, Origin, and GraphPad Prism 9.

For PADI6 protein distribution analyses, line profile analysis was performed in Fiji, drawing a line with width 5 across the full diameter of the oocyte (Figures S1F and S1H). Pixel intensity along the drawn line was exported and plotted in GraphPad Prism.

For cytoplasmic lattice width calculation in 3D STED images (Figure 2H), a line with width 5 was drawn perpendicular across a filament. The measured pixel intensities were plotted and fitted to a gaussian curve using the Levenberg Marquardt equation in Origin from which the full-width at half maximum was extracted.

3D STED cytoplasmic lattice segmentation was performed in Fiji, Ilastik, and Imaris (Oxford Instruments). First, image sections were imported in Fiji and drift-corrected using the linear stack alignment with SIFT.[127] Drift-corrected images were imported into Ilastik for pixel classification. Three categories were created for cytoplasmic lattices "CPL", "border" for the area between the cytoplasmic lattice structures and the background, and "background". The categories were manually annotated on imported z-stacks. A training dataset for pixel classification was used and separate datasets were processed subsequently. Segmentation probabilities were exported into Fiji and a threshold of 0.7 was applied for the CPL segmented file. A binary mask was created after thresholding and multiplied with the original drift-corrected image sections. The segmented image was imported into Imaris for 3D visualization of cytoplasmic lattice fluorescent signal and measurement points were manually added to mark individual filaments. Care was taken that measured filaments were not cropped by the image boundaries. Distance between measurement points were exported to Microsoft Excel and plotted in GraphPad Prism 9.

To calculate the enrichment of mass spectrometry identified candidates on cytoplasmic lattices, the ratio of candidate protein signal on the lattices versus the cytoplasm was calculated. To this end, an Ilastik pixel classification model was trained on images stained for PADI6 alone. PADI6 was stained with an AlexaFluor-647 secondary antibody for all enrichment experiments. The candidates were labelled with an AlexaFluor-568 secondary antibody, except for the GFP-control in Figure S7E, where the GFP signal was enhanced with an anti-GFP antibody labelled with an AlexaFluor-488 secondary antibody. Segmentation probabilities were exported into Fiji and a threshold of 0.5 was applied for the PADI6-segmentation image. Several thresholds (0.5, 0.6, and 0.7) were tested and did not give significantly different results (Figure S6Q). An image selection ROI around the PADI6 mask was applied to the candidate protein channel, and the mean fluorescence intensity was measured within the mask and the inverted mask. All fold enrichment values for all probed candidate proteins are derived from at least two independent experiments. The values were exported to Microsoft Excel and the ratio between the two values were calculated and plotted in GraphPad Prism 9.

The 90-degree rotation control analysis was performed by drawing a line profile with width 13 in Fiji along a cytoplasmic lattice fiber. The fluorescence intensity of the PADI6 and candidate protein channels (original and rotated) were exported and plotted in GraphPad Prism.

Quantification FRAP experiments

Mean intensities of ROIs over time were exported from Zen to Excel (Microsoft). The intensity of the ROI outside the cell was used for background subtraction of the bleached (FRAP) and non-bleached (reference) ROIs inside the cytoplasm. Intensities of all time points from a background-corrected ROI were normalized to the average intensity of the 3 pre-bleach time points and the bleached ROI further normalized to the reference intensities:

$$Norm\ (t) = \frac{FRAP_{(t)}}{Average\ FRAP_{pre-bleach}} \times \frac{Average\ ref_{non-bleached}}{Ref_{(t)}}$$

Plots of intensity against time were plotted in GraphPad Prism 9. Half-time of maximum recovery ($t_{1/2}$) and immobile mobile fractions (F_i) were determined by $\tau \times \ln(2)$ and $1-(F_\infty/(F_0-F'))$ (where F' is the minimum intensity measured immediately after photobleaching), respectively.

Supplemental figures

A Chromosome 4

B

C

D

E Halo-PADI6 oocyte

Merge DNA

■ Halo-SiR-PADI6   ■ anti-PADI6
+fluorescent secondary antibody

F Halo-PADI6 oocyte

■ Halo-SiR-PADI6
■ anti-PADI6
+fluorescent secondary antibody

G

H Wild type oocyte

■ anti-PADI6-Alexa488
(directly labelled)

I Direct labelling
of primary antibody

Primary antibody labelled
by fluorescent secondary
antibodies

■ Antigen
⊢ Primary antibody
⊣ Secondary antibody
★ Fluorophore

J Expression of Halo-tagged PADI6/SCMC proteins in fully-grown oocytes

■ Halo-PADI6   ■ Halo-TLE6   ■ Halo-OOEP   ■ Halo-KHDC3

Inset

K Post-bleach

Pre-bleach   0 s   40 s   80 s   120 s

■ mClover3-PADI6

L mClover3-PADI6

$t_{1/2}$=3.29±0.3 s
F_i=66.0±7.6%

(legend on next page)

Figure S1. PADI6 and SCMC proteins form stable fibers throughout the oocyte cytoplasm, related to Figure 1

(A) Schematic representation of the HaloTag-*Padi6* knockin mouse line generation. A detailed description can be found in STAR Methods.

(B) Immunoblot showing expression of wild-type (WT) PADI6 and Halo-PADI6 protein in oocytes from WT, p/+, and p/p female mice. The protein Glyceraldehyde 3-phosphate dehydrogenase (GAPDH) was used as a loading control.

(C) Number of oocytes collected from females of WT, Halo-*Padi6* p/+, and p/p genotypes. Number of mice indicated in italics. Mean value indicated as vertical line.

(D) Number of pups per litter from females of Halo-Padi*6* WT, p/+, and p/p genotypes. Number of litters analyzed indicated in italics. Mean value indicated as vertical line. In (C) and (D), p values were calculated using an unpaired two-tailed Student's t test and reported as exact values.

(E) Representative micrograph of Halo-SiR-PADI6 (magenta) oocytes co-stained with an anti-PADI6 antibody with a fluorescent secondary antibody (green) and DNA (gray). Scale bar, 10 μm.

(F and G) Magnified micrograph of oocyte in (E). Signal intensity profiles for Halo-PADI6 and anti-PADI6 along yellow line are shown in (G). Magenta and green lines represent Halo-PADI6 and anti-PADI6 signal profiles, respectively. Scale bar, 10 μm.

(H) Representative micrograph of a mouse GV oocyte stained with a directly coupled anti-PADI6-Alexa 488 antibody. Signal intensity profile (yellow line) is shown on the right. Nuclear area is indicated by gray shading. Scale bar, 10 μm.

(I) Scheme of direct and indirect antibody labeling strategies. Fluorescent secondary antibodies generate a coat around the primary antibody.

(J) Representative micrographs of fully grown GV mouse oocytes expressing Halo-PADI6, Halo-TLE6, Halo-OOEP, or Halo-KHDC3 (all gray). Oocytes were labeled with Halo-JF549 following a 3 h mRNA expression period and subsequently fixed. Halo-PADI6 was incorporated slightly better than the other SCMC proteins. Scale bars, 10 μm.

(K) FRAP of mClover3-PADI6 in GV-arrested oocytes. mClover3-PADI6 shown in gray. Bleached area is indicated by yellow boxes. Scale bar, 10 μm.

(L) Quantification of fluorescence recovery. Yellow line indicates bleaching event. Data curve shows the mean±standard deviation. Number of analyzed cells specified in italics. Fi, immobile fraction.

All insets are magnifications of outlined regions.

A Manual landmark measurements

B Similarity scaling

C Interphase microtubules (GV oocyte) — Pre-ExM | Post-ExM (similarity-registered) | Post-ExM (non-rigid-registered) | Merged

D

E Post-ExM (affine-registered) | Post-ExM (non-rigid-registered) | Merged

F

G Metaphase I spindle — Pre-ExM | Post-ExM (similarity-registered) | Post-ExM (non-rigid-registered) | Merged

H

I Post-ExM (affine-registered) | Post-ExM (non-rigid-registered) | Merged

J

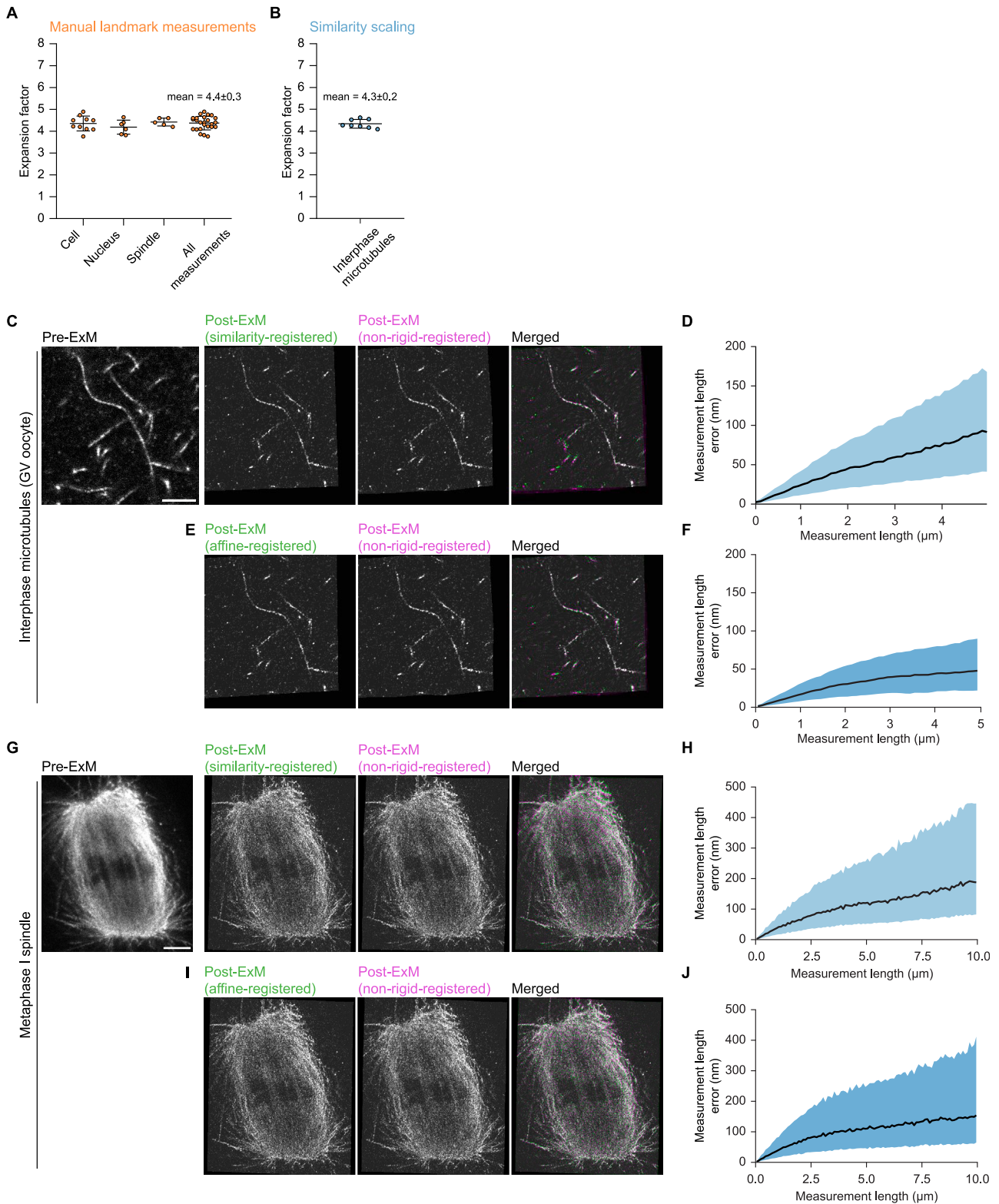**Figure S2. Quantification of ExM anisotropy error, related to Figure 2**

(A) Quantification of the gel expansion factor by measurement of cellular landmarks such as the whole-cell size, the nucleus size, and spindle length. The expansion factor is calculated by dividing the post-ExM to the pre-ExM length. All individual measurements pre- and post-ExM were carried out in the same cell

(legend continued on next page)

and the same imaging plane was identified in pre- and post-ExM micrographs. Data are represented as mean ± standard deviation (SD). For "all measurements," the mean ± SD is noted above the data points.

(B) Expansion factor calculated from the scaling factor obtained by a similarity transform registering the post-ExM to the pre-ExM image. Input data are from labeled interphase microtubules in GV oocytes. Data are represented as mean ± standard deviation, which is also noted above the data points.

(C) Interphase microtubules in GV oocytes. Representative region of interest (ROI) before and after expansion. The post-ExM image was registered to the pre-ExM image using a similarity or non-rigid transformation (B-splines). The last panel shows the overlay of similarity transformed (green) and non-rigid transformed (magenta) post-ExM images. Scale bar, 5 μm.

(D) Measurement length error as function of measurement length comparing the similarity and non-rigid transformed images. Data shows the median lower and upper quantile from in total 4 gels, 6 oocytes, and 20 ROIs. Spatial scale corresponds to the pre-ExM image.

(E) The post-ExM image was registered to the pre-ExM image in (C) using an affine and a non-rigid transformation. The last panel shows the overlay of affine transformed (green) and non-rigid transformed (magenta) post-ExM images.

(F) Measurement length error as function of measurement length comparing the affine and non-rigid transformed images. Data shows the median lower and upper quantile from in total 4 gels, 6 oocytes, and 20 ROIs. Spatial scale corresponds to the pre-ExM image.

(G) Microtubules in an oocyte metaphase I spindle. Representative ROI before and after expansion. The post-ExM image was registered to the pre-ExM image using a similarity or non-rigid transformation. The last panel shows the overlay of similarity transformed (green) and non-rigid transformed (magenta) post-ExM image. Scale bar, 5 μm.

(H) Measurement length error as function of measurement length comparing the similarity and non-rigid transformed images. Data shows the median lower and upper quantile from in total 4 gels, 5 oocytes, and 10 ROIs. Spatial scale corresponds to the pre-ExM image.

(I) The post-ExM image was registered to the pre-ExM image in (G) using an affine and a non-rigid transformation. The last panel shows the overlay of affine transformed (green) and non-rigid transformed (magenta) post-ExM images.
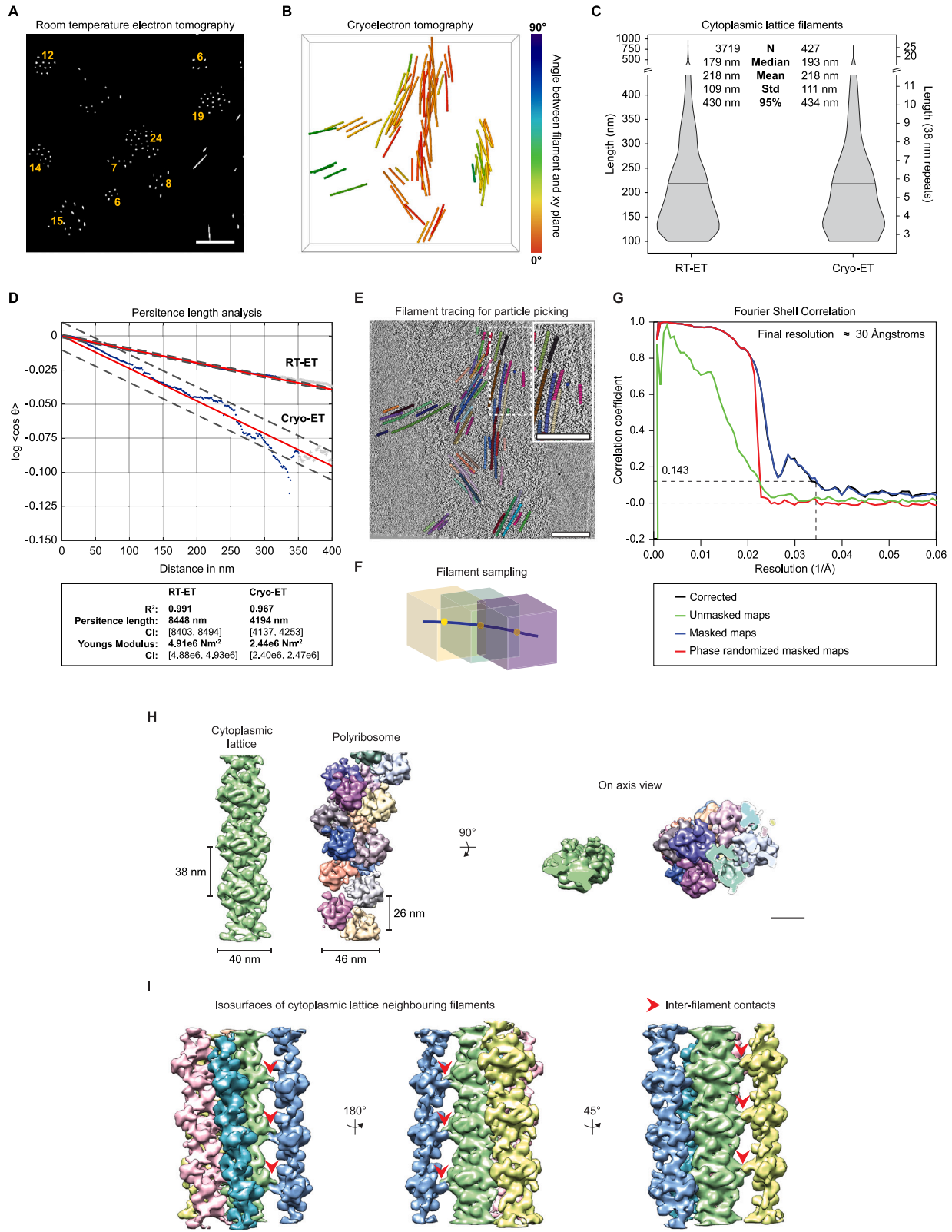
(J) Measurement length error as a function of measurement length comparing the affine and non-rigid transformed images. Data shows the median lower and upper quantile from in total 4 gels, 5 oocytes, and 10 ROIs. Spatial scale corresponds to the pre-ExM image.

A Room temperature electron tomography

B Cryoelectron tomography

Angle between filament and xy plane

C Cytoplasmic lattice filaments

3719	**N**	427	
179 nm	**Median**	193 nm	
218 nm	**Mean**	218 nm	
109 nm	**Std**	111 nm	
430 nm	**95%**	434 nm	

D Persitence length analysis

RT-ET
Cryo-ET

	RT-ET	Cryo-ET
R²:	**0.991**	**0.967**
Persitence length:	**8448 nm**	**4194 nm**
CI:	[8403, 8494]	[4137, 4253]
Youngs Modulus:	**4.91e6 Nm⁻²**	**2.44e6 Nm⁻²**
CI:	[4.88e6, 4.93e6]	[2.40e6, 2.47e6]

E Filament tracing for particle picking

F Filament sampling

G Fourier Shell Correlation

Final resolution ≈ 30 Ångstroms

0.143

— Corrected
— Unmasked maps
— Masked maps
— Phase randomized masked maps

H Cytoplasmic lattice   Polyribosome

On axis view

90°

38 nm

26 nm

40 nm   46 nm

I Isosurfaces of cytoplasmic lattice neighbouring filaments

Inter-filament contacts

180°   45°

(legend on next page)

Figure S3. Analysis of cytoplasmic lattice filament organization by RT- and cryo-ET, related to Figure 3

(A) Binary tomographic slice through a 3D representation of the filament segmentation from a RT-EM tomogram. The traces of individual filaments arranged in bundles are shown in white. Numbers indicate the number of filament neighbors per bundle.

(B) 3D rendering of filaments shown in the cryoelectron tomogram in Figure 3E. Color scale depicts the angle between the xy plane and the filament: 0° (warm colors) represents filaments in the xy plane, 90° (cold colors) represents filaments perpendicular to the image plane.

(C) Statistical analysis of cytoplasmic filament length in RT-ET and cryo-ET data. The left y axis measures the length in nm and the right y axis measures the length in numbers of 38-nm repeats. Violin plots visualize the distribution, and horizontal lines mark the mean. Number of filaments (n); ET-ET = 3,719, cryo-ET = 427. Data extracted from a total of 7 (RT-ET) and 5 (cryo-ET) tomograms.

(D) Linear fits for the apparent persistence length for RT-ET and cryo-ET tomograms' analyzed filaments (red lines). Blue dots represent the original data. 95% confidence interval (broken lines) and the values of the persistence length; Young's modulus and coefficients of determination (R^2) are indicated in the text box. Note that the apparent persistence length is larger in RT-ET compared with cryo-ET tomograms, possibly due to the chemical fixation in RT-ET, which crosslinks proteins and thus increases the stiffness of the filaments in this environment. Number of fibrils and tomograms as indicated in (C).

(E) Traced filaments superimposed on the corresponding tomogram used for particle picking in Dynamo. Filaments are depicted in different colors. Inset: high magnification of the dashed region in the tomogram.

(F) Schematic outline of the filament sampling and particle picking procedure. The filament is depicted as a blue line and the sampling points as yellow dots. The colored cubes centered on these points represent subvolumes extracted for the subtomogram averaging procedure.

(G) Fourier shell correlation (FSC) of the central filament with a final global resolution of 30 Å at 0.143 cut-off. The FSC curves for the unmasked (green), masked (blue), corrected (black), and phase randomized maps (red) are reported.

(H) Size comparison between the cytoplasmic lattice filament (left) and the eukaryotic polyribosomes (EMDB database: EMDB-2790,[144] right). Each ribosome is depicted in a different color.

(I) Isosurface representation of the subtomogram average of the filament fiber in different orientations. The red arrowheads indicate the inter-filament contacts. Scale bars, 250 nm in (A), (E), and inset in (E), 25 nm in (H) and (I). Field of view. 1,500 nm in (B).
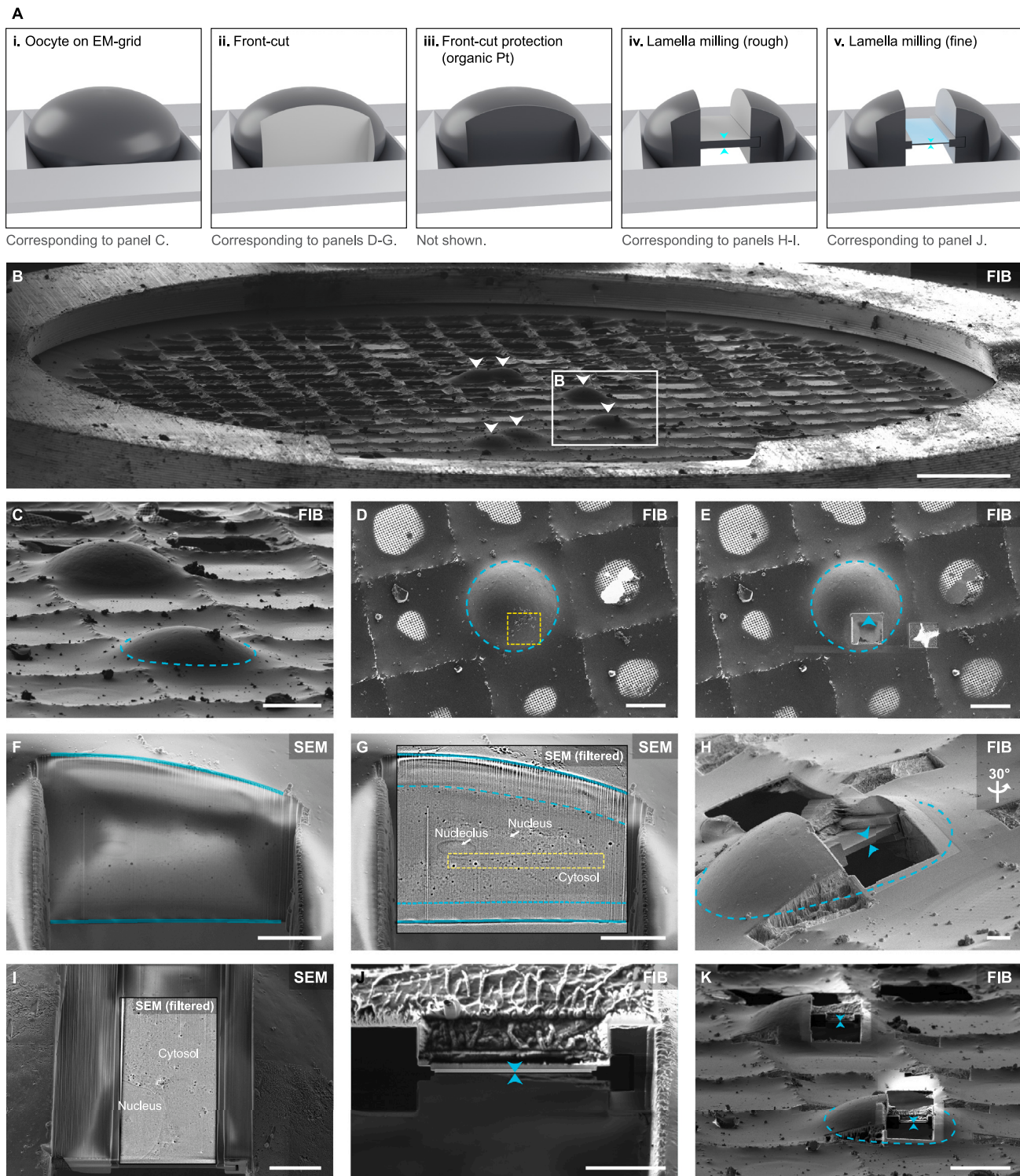
A

i. Oocyte on EM-grid	**ii.** Front-cut	**iii.** Front-cut protection (organic Pt)	**iv.** Lamella milling (rough)	**v.** Lamella milling (fine)
Corresponding to panel C.	Corresponding to panels D-G.	Not shown.	Corresponding to panels H-I.	Corresponding to panel J.

Figure S4. Cryo-FIB lamella preparation of oocytes with deep-FIBing, related to Figure 3 and STAR Methods

(A) Schematic representation of the deep-FIBing approach. (Ai) Oocyte deposited within a 100-μm mesh of an EM grid (see C). The dark surface represents gaseous organic platinum, which was deposited on the sample using gas injection. (Aii) The front of the oocyte was milled from the top (under 90° to the grid plane), after rotating the stage by 180° (see D and E). This assures a smooth, contamination-free surface for an optimal lamella preparation at any depth inside the cell (see F). Biological structures in this cross-section can be imaged, allowing screening for interesting cellular regions by serial block-face imaging to determine the final positioning of the lamella (see G). (Aiii) To protect the newly created surface, gaseous organic platinum (dark surface) was deposited a second time on the

(legend continued on next page)

sample from an angle similar to the milling direction. (Aiv) Large volumes of the cell were removed above and below the lamella (see H). To prevent bending of the lamella during the preparation, and fracturing of the lamella due to thermal expansion/shrinking during later transfers, the lamella is disconnected from the rest of the cell with a lateral notch (see H and I). Cellular structures can be imaged during milling, as in (Aii, G), to guide the final lamella preparation (see I). (Av) Classical FIB lamella preparation is applied to thin down the lamella to <200 nm (see J).

In the following panels, the mode of imaging is indicated as scanning electron microscopy (SEM) or secondary electrons induced by the ion beam (FIB).

(B) FIB panorama side-view of the entire EM grid containing six oocytes (white arrowheads).

(C) Magnification of the area boxed in (B) containing two oocytes. The dotted line indicates the oocyte shown in the following panels.

(D) FIB top-view of the oocyte marked in (C). The yellow dotted box marks the planning of $\sim$40 $\times$ 45 μm^2 area, which will be removed by FIB milling in (E).

(E) FIB top-view after FIB-milling of the boxed area in (D). The blue arrowhead shows the angle of view on the cross-section shown in (F).

(F) SEM view of the cross-section through the oocyte created in (E). The surface is flat and free of any ice-crystal contamination, facilitating subsequent lamella preparation. Blue lines indicate top and bottom surfaces of the sample.

(G) Overlay of a filtered version of the surface shown in (F). The image is filtered by a combination of an FFT high-pass filter and contrast-limited adaptive histogram equalization. The filtered micrograph significantly facilitates the interpretation of the cellular context in comparison to (F): the nucleus, nucleolus, and cytosolic elements are clearly distinguishable. The filtering also allows the precise planning of the following cryo-FIB lamella preparation (yellow dotted box). The blue broken lines mark the oocyte plasma membrane.

(H) 30° rotated FIB view of the 5-μm-thick lamella (blue arrowheads) through the oocyte after rough milling at the location indicated in (G).

(I) SEM view of the lamella surface at 2 kV after further thinning. Overlay of a SEM image filtered as described in (G).

(J) FIB-view of the final lamella with $\sim$150 nm thickness (blue arrowheads).

(K) Final result after deep-FIBing cryo-FIB lamella preparation of the two oocytes shown in (C). The dotted line indicates the oocyte shown in (D)–(J).

Scale bars, 250 μm in (B), 50 μm in (C)–(E) and (K), 10 μm in (F)–(J).
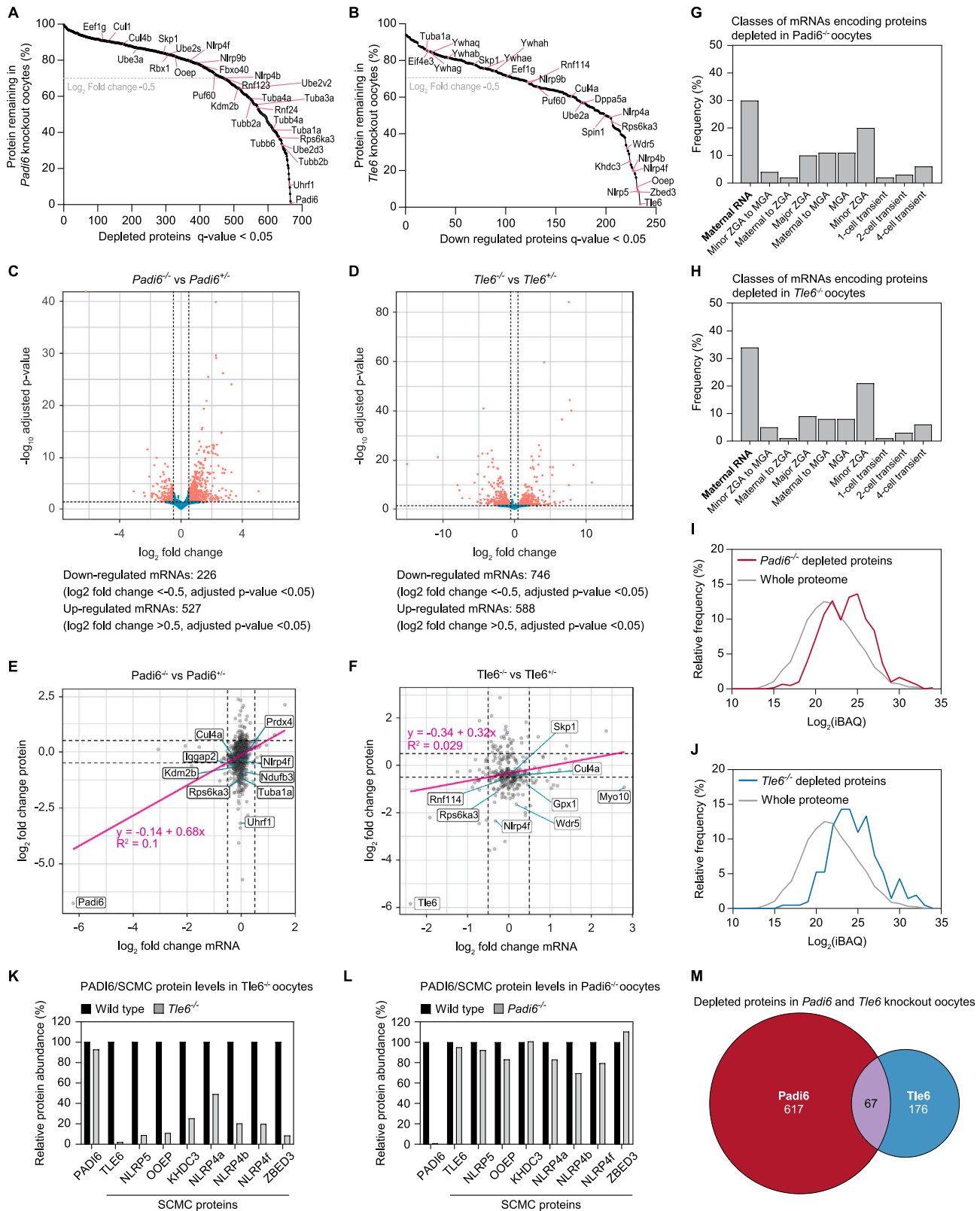
Figure S5. Proteomic and transcriptomic analysis of *Padi6*$^{-/-}$ and *Tle6*$^{-/-}$ oocytes, related to Figure 4

(A and B) Distribution of depleted proteins in *Padi6*$^{-/-}$ (A) or *Tle6*$^{-/-}$ (B) oocytes. Percentage of protein levels remaining in knockout oocytes is plotted for each significantly less abundant protein (q value < 0.05). Gray line indicates a log$_2$ fold change of −0.5.

(C and D) Differential gene expression analysis after RNA sequencing of *Padi6*$^{-/-}$ and *Padi6*$^{+/-}$ (C) or of *Tle6*$^{-/-}$ and *Tle6*$^{+/-}$ (D) oocytes. Differentially expressed genes are indicated in red. Vertical dashed lines represent a log$_2$ fold change of −0.5 or 0.5. Horizontal dashed line represents the adjusted p value = 0.05.
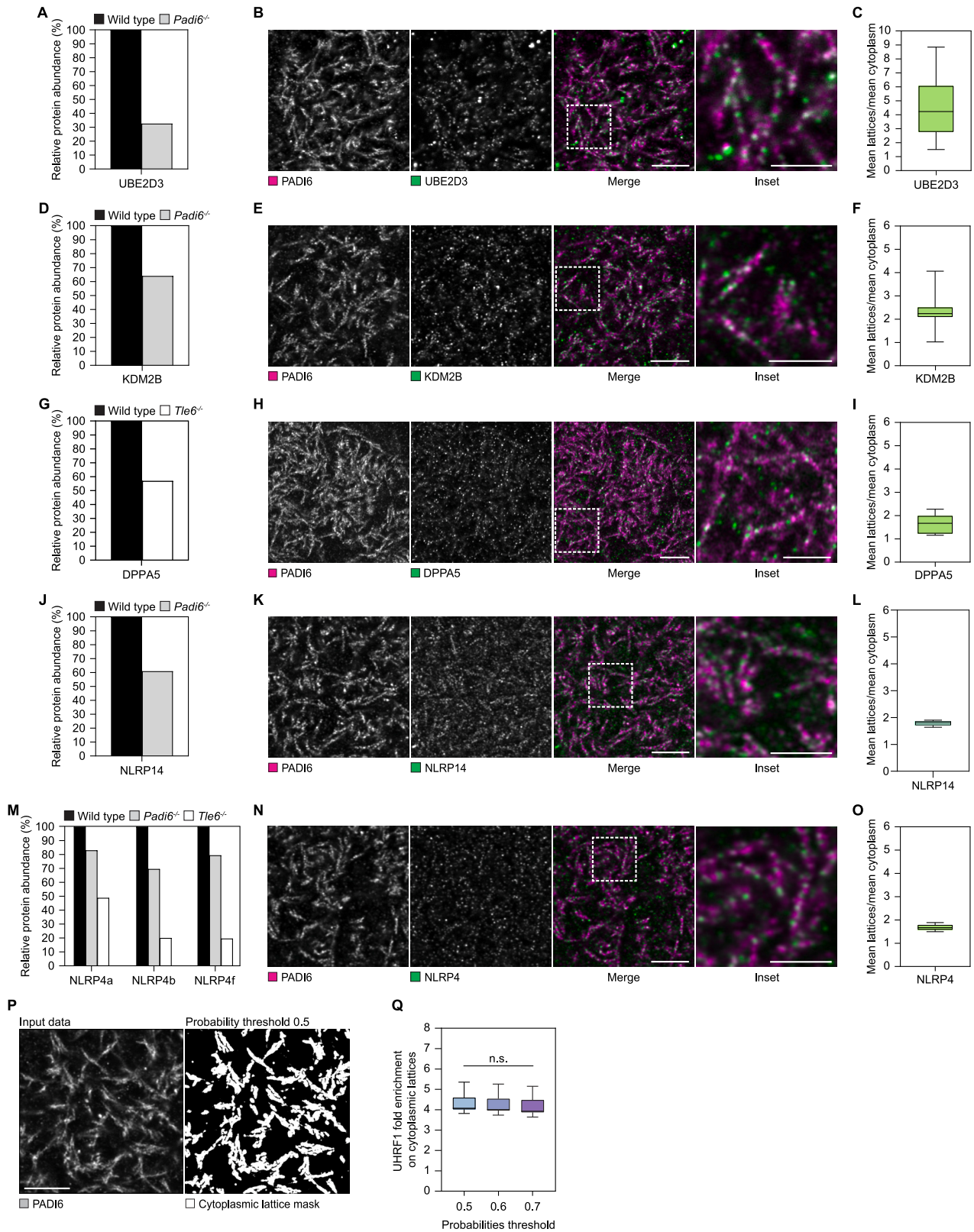
(E and F) Comparison of log$_2$ fold change for all significantly changed proteins (q value < 0.05) and log$_2$ fold change of their respective transcripts in *Padi6*$^{-/-}$ versus *Padi6*$^{+/-}$ (E) and *Tle6*$^{-/-}$ versus *Tle6*$^{+/-}$ (F) oocytes. A linear regression line (magenta) was fitted to the data. The regression line equation with R^2 value is indicated in magenta. Dashed lines indicate log$_2$ fold change of 0.5 or of −0.5.

(G and H) Classification of mRNAs encoding depleted proteins in *Padi6*$^{-/-}$ (G) and *Tle6*$^{-/-}$ (H) oocytes. The DMBTEE[66] database was used to classify the expression cluster of depleted proteins' mRNAs.

(I and J) Frequency distribution of intensity-based absolute quantification (iBAQ) values for the whole proteome (gray) and depleted proteins in *Padi6*$^{-/-}$ (I, red) and *Tle6*$^{-/-}$ (J, blue) oocytes. The difference of the mean value between the two populations is statistically significant, p < 0.0001. p value calculated using an unpaired, two-tailed Student's t test. iBAQ values were generated from a data-dependent acquisition oocyte proteome dataset analyzed by MaxQuant described in Cheng et al.[135]

(K and L) Quantification of relative protein abundances of PADI6 and SCMC proteins in *Tle6*$^{-/-}$ (K) and *Padi6*$^{-/-}$ (L) oocytes compared with the wild type.

(M) Venn diagram showing the overlap of significantly depleted proteins between *Padi6*$^{-/-}$ and *Tle6*$^{-/-}$ oocytes.

A Relative protein abundance (%) — Wild type / *Padi6⁻/⁻* — UBE2D3

B PADI6 / UBE2D3 / Merge / Inset

C Mean lattices/mean cytoplasm — UBE2D3

D Relative protein abundance (%) — Wild type / *Padi6⁻/⁻* — KDM2B

E PADI6 / KDM2B / Merge / Inset

F Mean lattices/mean cytoplasm — KDM2B

G Relative protein abundance (%) — Wild type / *Tle6⁻/⁻* — DPPA5

H PADI6 / DPPA5 / Merge / Inset

I Mean lattices/mean cytoplasm — DPPA5

J Relative protein abundance (%) — Wild type / *Padi6⁻/⁻* — NLRP14

K PADI6 / NLRP14 / Merge / Inset

L Mean lattices/mean cytoplasm — NLRP14

M Relative protein abundance (%) — Wild type / *Padi6⁻/⁻* / *Tle6⁻/⁻* — NLRP4a, NLRP4b, NLRP4f

N PADI6 / NLRP4 / Merge / Inset

O Mean lattices/mean cytoplasm — NLRP4

P Input data — PADI6 / Probability threshold 0.5 — Cytoplasmic lattice mask

Q UHRF1 fold enrichment on cytoplasmic lattices — n.s. — Probabilities threshold 0.5, 0.6, 0.7

(legend on next page)

Figure S6. PADI6- and TLE6-dependent proteins localize to cytoplasmic lattices, related to Figure 5

(A, D, G, J, and M) Quantification of relative protein abundance of proteins shown in (B), (E), (H), (K), and (N), respectively; (M) includes all significantly changed NLRP4 proteins.
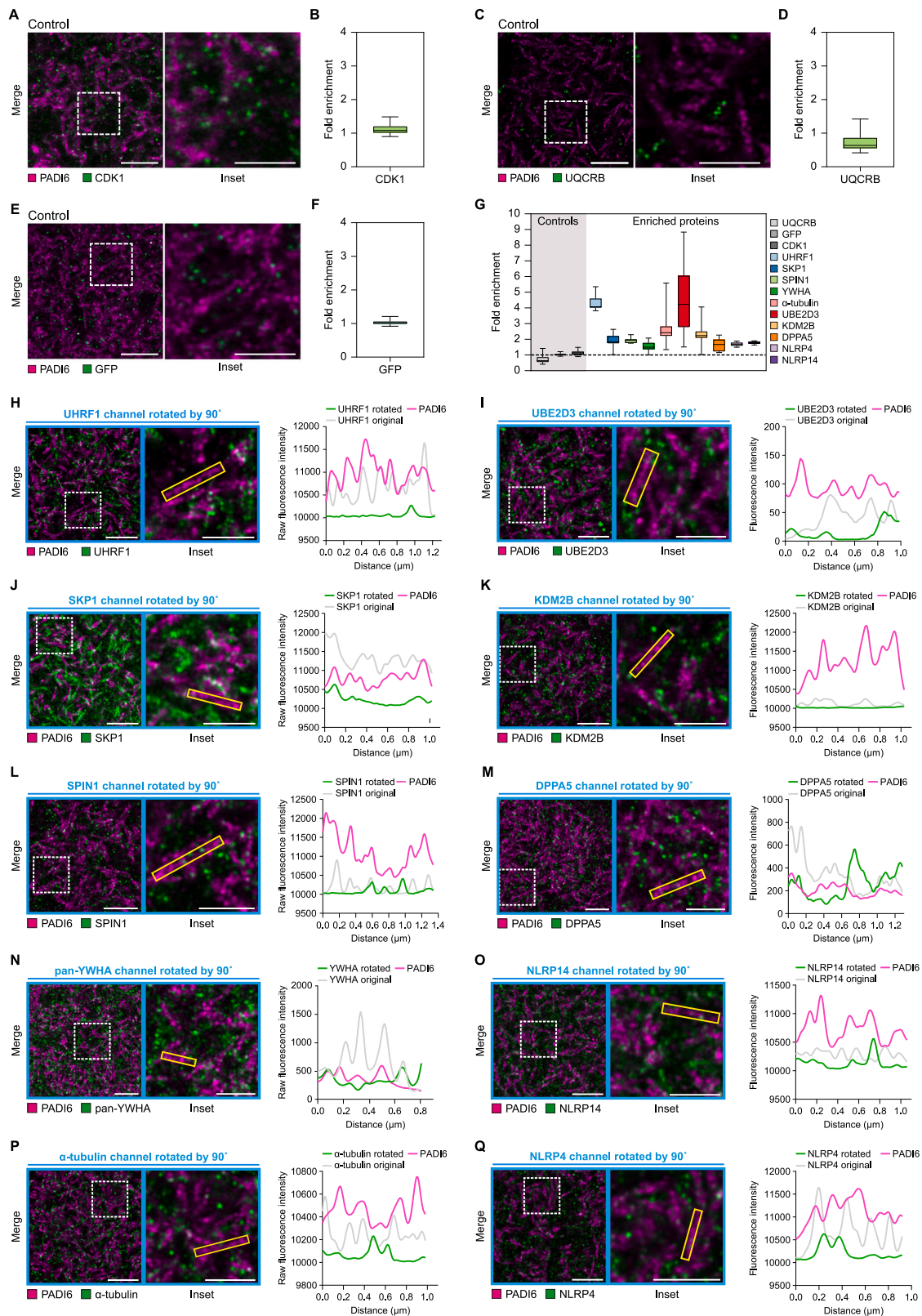
(B, E, H, K, and N) Representative ExM images of wild-type oocytes labeled for PADI6 (magenta) and UBE2D3, KDM2B, DPPA5, NLRP14, or NLRP4 (green), respectively. Insets are magnifications of outlined regions. Scale bars, 2 μm. Scale bars of insets, 1 μm. All images were acquired using a laser scanning confocal microscope. All scale bars are corrected for the expansion factor.

(C, F, I, L, and O) Quantification of candidate protein enrichment on cytoplasmic lattices. Fold enrichment was quantified as described in Figure 5 and STAR Methods. Vertical lines indicate the mean. Whiskers represent minumum and maximum values.

(P) Example ExM image of a GV oocyte labeled for PADI6 and the resulting binary mask when a 0.5 threshold is applied to the probability segmentation image from Ilastik. Scale bars, 2 μm.

(Q) Quantification of UHRF1 cytoplasmic lattice enrichment using different thresholds to create the segmented image. Thresholds between 0.5 and 0.7 did not yield significantly different results after a statistical test using a one-way ANOVA test.

See also Figure S7.

(legend on next page)

Figure S7. Channel rotation analyses confirm specific enrichment of candidate proteins on cytoplasmic lattices, related to Figure 5

(A, C, and E) Representative ExM micrographs of wild-type oocytes labeled for PADI6 (magenta) and CDK1, UQCRB, or GFP (green), respectively. Insets are magnifications of outlined regions. Scale bars, 2 μm. Scale bars of insets, 1 μm.

(B, D, and F) Quantification of CDK1, UQCRB, and GFP signal enrichment on cytoplasmic lattices. Fold enrichment was quantified as described in Figure 5 and STAR Methods.

(G) Comparison of fold enrichment between candidate proteins and controls as presented in Figures 5, S5, and S7. For (B), (D), (F), and (G), vertical lines indicate the mean and whiskers represent minumum and maximum values.

(H–Q) ExM micrographs of wild-type oocytes labeled for PADI6 (magenta) and candidate proteins (green), as presented in Figures 5 and S5, where the candidate channel (green) has been rotated by 90°, indicated by blue boxes. Insets are magnifications of outlined regions. Scale bars, 2 μm. Scale bars of insets, 1 μm. Line profiles within yellow boxes are plotted for each image. The line profile of the non-rotated image (as in Figures 5 and S5) is indicated with a gray line (original). Line profile fluorescence intensity values were exported from raw image files. Images were display adjusted for visualization.

All images were acquired using a laser scanning confocal microscope in Airyscan mode. All scale bars are corrected for the expansion factor.